

TRANSPORT OF POLYMERS AND PARTICLES IN MICROFABRICATED
ARRAY DEVICES

by

BRIAN R. LONG

A DISSERTATION

Presented to the Department of Physics
and the Graduate School of the University of Oregon
in partial fulfillment of the requirements
for the degree of
Doctor of Philosophy

June 2008

University of Oregon Graduate School

Confirmation of Approval and Acceptance of Dissertation prepared by:

Brian Long

Title:

"Transport of polymers and particles microfabricated array devices"

This dissertation has been accepted and approved in partial fulfillment of the requirements for the Doctor of Philosophy degree in the Department of Physics by:

Miriam Deutsch, Chairperson, Physics
Heiner Linke, Advisor, Physics
Dietrich Belitz, Member, Physics
Paul Csonka, Member, Physics
Andrew Marcus, Outside Member, Chemistry

and Richard Linton, Vice President for Research and Graduate Studies/Dean of the Graduate School for the University of Oregon.

June 14, 2008

Original approval signatures are on file with the Graduate School and the University of Oregon Libraries.

show no conformational changes indicative of the polymer ratchet mechanism, despite the polymer motion. This result and detailed analysis of the DNA trajectories, suggest that the observed motion was driven by bulk flow generated through electroosmosis, in agreement with results from experiments using particles in similar devices.

Deterministic Lateral Displacement (DLD) uses an array of obstacles in a microfluidic channel to sort micron-scale objects with $\sim 10\text{nm}$ precision. However, very little work has been done to quantitatively address the role of diffusion in DLD sorting. Here, modeling of transport in DLD arrays has shown that using arrays of obstacles that are small compared to their separation can create sorting that is robust against changes in flow velocity. Also, novel sorting modes were revealed when the model was applied to unconventional array geometries that have not been discussed in the literature.

CURRICULUM VITAE

NAME OF AUTHOR: Brian Russell Long

GRADUATE AND UNDERGRADUATE SCHOOLS ATTENDED:

University of Oregon, Eugene, Oregon

University of Washington, Seattle, Washington

DEGREES AWARDED:

Doctor of Philosophy, Physics, June 2008, University of Oregon

Bachelor's of Science in Physics, 2002, University of Washington

AREAS OF SPECIAL INTEREST:

Condensed Matter

Biophysics

PROFESSIONAL EXPERIENCE:

Graduate Research Assistant under UO Prof. Heiner Linke, 2003-2008

Graduate Teaching Assistant under UO Prof. Dean Livelybrooks, 2002-2003

GRANTS, AWARDS AND HONORS:

IGERT International Travel Grant to Lund University, UO MSI, 2006

IGERT International Travel Grant to Lund University, UO MSI, 2005

GAANN Fellowship, Particles in microfabricated arrays, UO MSI, 2004

Mary Gates Research Training Grant, University of Washington,
2002 and 2000

Exchange Scholarship to Giessen, Germany, University of Washington
Physics Department, 2000-2001

PUBLICATIONS:

Craig, E.M, B.R. Long, J.M.R. Parrondo and H. Linke, "Effect of time delay on feedback control of a flashing ratchet." *Europhys. Lett.* **81**(1), (2008)

J.M.K. Donev, Q. Yu, B.R. Long, R.K. Bollinger, S.C. Fain, "Noncontact atomic force microscopy studies of ultrathin films of amorphous solid water deposited on Au(111)", *J. Chem. Phys.* **123**(4), (2005)

ACKNOWLEDGMENTS

I am grateful to Prof. Heiner Linke for his support during my studies at the University of Oregon and especially for his very helpful work in reviewing this manuscript. Linke lab group members Erin Craig, Ben Lopez, Nate Kuwada and Ruth Saunders all provided invaluable help over the past six years in discussions both scientific and otherwise. Matthew Downton also provided insightful conversations, Unix advice and useful simulation data. Deterministic Lateral Displacement work was inspired by and developed in conversations with Prof. Jonas Tegenfeldt at Lund University, who was an excellent mentor during my stay there. My progress to this point is due in no small part to the advice, examples and encouragement provided by my family and friends, for which I am very thankful.

TABLE OF CONTENTS

Chapter	Page
I. INTRODUCTION	1
Diffusion	2
Brownian Ratchets	2
Brownian Ratchet Case Study: The Flashing Ratchet	3
Flashing Ratchet: Experimental Precedents	4
The Polymer Ratchet	6
Transporting and Sorting Micron-scale Objects in Aqueous Solution	7
II. THERMAL MOTION, BROWNIAN RATCHETS AND TRAJECTORY ANALYSIS	9
Brownian Motion	9
The Flashing Ratchet	11
Trajectory Analysis	13
III. POLYMERS IN A FLASHING RATCHET	21
Polymer Ratchet Model	21
Experimental Relevance	23
IV. BACKGROUND: RELEVANT PHYSICAL CHEMISTRY OF AQUEOUS SOLUTIONS	24
Introduction	24
pH and Ions in Solution	24
DNA in Solution	25
Electrostatic Screening	27
V. PARTICLE EXPERIMENTS AND RESULTS	31

Chapter	Page
Introduction	31
Experiment Protocol	32
Observations in Particle Experiments	33
Particle Motion in Response to Applied Potential	33
Particle Displacement and Velocities	35
Position Histograms	38
Ionic Strength	40
Discussion	42
Screening and Electrostatic Potentials in Interdigitated Electrode Array Devices	45
Electroosmosis	47
Transient Reversals	52
Additional Observations	53
Summary of Results from Particle Experiments	54
 VI. POLYMER EXPERIMENTS AND RESULTS	 56
Introduction	56
Background	57
Experiment Design and Description	59
Analysis	62
Observations in Polymer Experiments	62
Principal Components Analysis	70
DNA Conformational Changes in Response to an Applied Potential	82
Summary of Results of Polymer Experiments	84
 VII. DIFFUSION AND NOVEL GEOMETRIES IN DETERMINISTIC LATERAL DISPLACEMENT DEVICES	 88
Introduction	88
Model and Implementation	91
Results	96
Discussion	99
Conclusions	104
 VIII. CONCLUSIONS AND OUTLOOK	 106

Chapter	Page
Conclusions	106
Outlook	107
 APPENDICES	
A. IMAGE ANALYSIS AND OBJECT TRACKING	109
Introduction	109
Locating Objects in Images	110
Creating Trajectories from Positions	111
B. DNA SOLUTION	112
Introduction	112
Making the DNA Solution	112
C. FABRICATION OF INTERDIGITATED ELECTRODE DEVICES . .	114
Device Fabrication: Polymer Experiments	114
Experimental Procedure	116
Device Fabrication: Particle Experiments	116
D. FLUORESCENCE MICROSCOPY METHODS	120
Particle Experiments	120
Polymer Experiments	120
BIBLIOGRAPHY	122

LIST OF FIGURES

Figure	Page
1.1 a) Particles in an asymmetric potential with period L , asymmetry α and amplitude $U \gtrsim k_B T$. b) When the potential is switched off, the particles diffuse isotropically. c) When the potential is switched on again, the asymmetry of the potential generates net motion of the particles in one direction as the new equilibrium distribution is reached. By repeating this cycle many times, macroscopic displacements can be achieved without the use of a macroscopic potential gradient.	4
1.2 a. Interdigitated electrodes. For particle ratchet experiments described in Chapter V $L = 10 - 40 \mu m$ and $CD = 1 - 4 \mu m$. For the polymer ratchet discussed in Chap. VI, $L = 500 nm$ and Electrode Width $\approx 50 nm$. b. The electrode array dimensions are $W = 2 mm$ for particle experiments and $W = 80 \mu m$ for polymer experiments. c. Sketch of microchamber construction (for details see Appendix C)	5
2.1 Squared displacements of 12 $0.2 \mu m$ -diameter particles in a $1.5 \mu m$ -deep microchannel. The range of squared displacements increases linearly with time. These 12 particles were all present in the field of view for 1000 frames collected at about 3 frames/sec.	15
2.2 Sketch of a trajectory divided into adjacent segments of Δt for square displacement analysis.	16
2.3 A. Mean squared displacement $\langle \Delta x^2 \rangle$ for 12 particles plotted versus Δt . The line plotted is $2D\Delta t$ using D calculated as described in the Sec. 2.3.2. B. The same data near the origin.	18
2.4 Calculated values of D with error bars for the data shown in Figures 2.3 and 2.1.	19
4.1 The chemical structure of DNA showing the paired nucleic bases (guanine-cytosine and adenine-thymine) connecting the two phosphate-sugar backbones. Image from [1]	26

Figure	Page
5.1 a. Interdigitated electrodes. For particle ratchet experiments, $L = 10 - 40\mu m$ and $d_c = 1 - 4\mu m$. b. The electrode array dimension $W = 2\text{ mm}$ for particle experiments. c. Sketch of microchamber construction.	33
5.2 Particle locations from 1000 images of $0.2\mu m$ -diameter particles overlaid on an image of the interdigitated electrode array.	34
5.3 Applied voltage, $\langle \Delta x \rangle_t$ (top) and time-averaged mean velocity over each experiment (bottom) for two experiments showing response to applied voltage. The direction of transport is x (perpendicular to the electrodes) while y is parallel to the electrodes and transverse to the microchannel. Data is for about 10 $0.2\mu m$ -diameter, carboxylate-modified, fluorescent microspheres in 10^{-3} M NaCl solution.	37
5.4 Applied voltage, mean x displacement and time-averaged mean velocity, $\langle \Delta x \rangle_t$. Peak mean velocities are circled.	38
5.5 Peak $\langle v \rangle_t$ versus applied voltage. Variability in the peak $\langle v \rangle_t$ immediately after switching on and switching off increases for greater applied voltage. The magnitude and direction of peak velocities is variable at all voltages despite electrode arrays being in the same orientation for all experiments. These data were collected under the range of ionic strengths plotted in Fig. 5.7.	39
5.6 A. Particle position histograms during experiment shown in Fig. 5.3A. Error bars are for each data point. B. Effective potential calculated from the distribution in A.	40
5.7 Peak mean velocities after switching on and off are plotted here versus ionic strength. Applied voltages cover the range shown in Fig. 5.5.	41
5.8 Electroosmotic flow at a charged surface driven by a uniform electric field E	48

Figure	Page	
5.9	Sketches of electroosmotically driven flows. Electroosmosis drives fluid flow within a Debye length of the surface, represented as a slip velocity here. The velocity falls off away from the surface with the size of the region driving the flow as a characteristic length scale. A. If screening of substrate charge is ignored, the slip boundary conditions at the surface and the resulting flows are symmetric. B. The presence of a positive screening layer across the surface induces an asymmetric slip velocity, thus preserving the asymmetry of the underlying applied potential.	55
6.1	False color images of λ DNA molecules in a microchannel above an interdigitated electrode array. Each image is about $5 \mu m$ across and was collected over an exposure time of 50 ms.	58
6.2	Left: Sketch of interdigitated electrode array used for polymer experiments. Right: Top view of device showing 'H' shaped microchannel design and electrical contact pads. Side view of device with chuck for microfluidic connections and vacuum seal.	60
6.3	Measured diffusion coefficient D for λDNA plotted <i>vs.</i> Δt in seconds. The error bars are the statistical error associated with calculating D from finite trajectories, as discussed in Sec. 2.3.1.	63
6.4	Mean DNA y -displacement <i>vs.</i> time before and during application of a flashing potential. DNA molecules move in the negative y -direction when the potential is on and reverse direction when the potential is turned off.	64
6.5	Mean DNA y displacement <i>vs.</i> time during the same time period shown in Fig. 6.5.	65
6.6	Mean DNA y velocity <i>vs.</i> time modulo two temporal periods of the flashing potential. For reference, the applied voltage is also plotted.	66
6.7	Mean DNA y displacement <i>vs.</i> time modulo two temporal periods of the flashing potential. This graph is derived only from time when the flashing potential was applied. The initial position at $t = 0$ is arbitrary, since this is averaged over many cycles of the applied voltage.	67

Figure	Page
6.8 Mean DNA intensity with no voltage applied. $\phi(x)$ and the Gaussian fits are described in the text. Mean DNA intensity falls off more slowly than the Gaussian, but also slightly more slowly than $\phi(x)$	71
6.9 False color images of the first 16 principal components (ordered left to right and top to bottom) from 5224 images of λ DNA in a microchannel above an interdigitated electrode array. Each image is about 5 microns across	76
6.10 A. Top view sketch of the thin slit described in the text. The slit ($10nm < h < 100nm$) was formed between the coverslip and the photoresist due to incomplete sealing. λ DNA was nonspecifically bound to the edge of the slit and stretched out by fluid flow in the main microchannel. After being pulled into the slit, the DNA then returned to a less extended configuration as it moved through the slit towards the narrow microchannel. The DNA's speed through the slit was approximately $14 \mu m/s$. B. Fluorescence microscopy images of DNA in the slit, taken from the region outlined in yellow in A. Scale bar on the right is $10 \mu m$. The full contour length of λ DNA when intercalated with ToTo-1 dye molecules is $22 \mu m$	78
6.11 The first 16 principal components calculated from images of DNA in the slit described in Sec. 6.6.3. The principal components are ordered by decreasing eigenvalue left to right and top to bottom. Not all of these principal components exhibit the same clear symmetries seen in those calculated from DNA in the microchannel. The DNA in the slit is exploring a wide range of non-equilibrium configurations that are rare in the dynamics of the equilibrium configurations. Images are $5 \mu m$ across.	79
6.12 A-C. Mean square of principal component amplitudes 2-4 <i>vs.</i> position in the slit sketched in Fig. 6.10. The decrease in magnitude seen in these graphs shows the conformational change associated with relaxation of the extended DNA to more compact coil configurations. D. Number of data points associated with each mean plotted in A-C.	81
6.13 False color images of the first 16 principal components from images of λ DNA subjected to a flashing voltage. These images are almost identical to those calculated from images of DNA before any potential was applied (see Fig. 6.9). Each image is about $5 \mu m$ across.	83

Figure	Page
6.14 Spectra of the stiffness of the first 16 principal components as a function of principal component number. Both plotted data sets are derived from expressing images in the same basis: principal components calculated from images collected before any voltage was applied. The first 11 principal components are shown to illustrate that modes with the same symmetries are largely interchangeable in these spectra.	85
6.15 Square of principal component amplitudes 1-4 of λ DNA <i>vs.</i> time modulo two cycles of the flashing potential. The amplitudes are averaged over about 17 temporal cycles of the potential and each plotted point corresponds to ≈ 120 data points. There is no clear signal in response to the applied potential, especially compared to the y -velocity from the same data, which is plotted in the same format in Fig. 6.6.	86
7.1 The basic DLD sorting mechanism in an array where the obstacle separation is $3\times$ the shift between rows ($N=3$). Particles smaller than r_c (see Eq. 7.1) follow streamlines through the array of obstacles giving the path labeled ‘U’. Particles larger than r_c are deflected at each row of posts, leading to the path marked ‘D’.	90
7.2 This sketch depicts the geometry used in the DLD model described in detail in Sec. 7.2. The array of point-sized posts is defined by p , the separation between posts, d , the distance between rows, and s , the lateral shift from one row to the next. Here $s = 0.3d = 0.3p$, corresponding to the results in Section 7.3. The point-like posts exclude the finite-sized particles with radius r from a circular region of the same radius around the post. The particle’s motion through the array in the absence of diffusion includes movement along the straight flowlines (parallel to \mathbf{v}) and hard interactions with the obstacles. The paths are indicated schematically by arrows showing the three modes of transport through the array. These modes are defined by two critical radii, r_{c1} and r_{c2} described in the text. In mode A, ($r \leq r_{c1}$), there is no systematic net displacement in the x -direction. In mode B, ($r_{c1} < r \leq r_{c2}$) the particle moves in a zigzag pattern but is systematically displaced (to the left for this array). In mode C, ($r > r_{c2}$), at each row of posts, particles are displaced by the row shift s	92

Figure	Page
7.3 a. Composite image of spatial distributions without diffusion for particles with radii $r < r_{c1}$ (Mode A), $r_{c1} < r \leq r_{c2}$ (Mode B) and $r > r_{c2}$ (Mode C). Spatial distributions are characterized by a sorting angle θ , which is defined from the flow direction \vec{v} to the center of mass of each distribution. b. The same particle radii moving through the array with flow speed of $100 \mu\text{m/s}$ and including the effect of diffusion. Broadening of all distributions due to diffusion can be seen and particles in Mode C are sorted less efficiently. Initial spatial distributions are the same for all particle radii.	93
7.4 Sorting angles versus particle radius without diffusion (filled circles) and with diffusion at a flow velocity of $10\mu\text{m/s}$. The negative sorting angles for $r_{c1} < r < r_{c2}$ indicate the presence of mode B for the array used here; as in the text and other figures, $r_{c1} = 1\mu\text{m}$ and $r_{c2} = 3\mu\text{m}$. Inset shows the same quantity around $r = r_{c2} = 3\mu\text{m}$ for a range of flow velocities (same y-axis range). The sharp transition between sorting modes is blurred by diffusion.	98
7.5 Spatial distributions of particles and mode detectability. Particle densities after ten rows of the array for three radii, $0.9 \mu\text{m}$, $2 \mu\text{m}$ and $3.08 \mu\text{m}$. a. No diffusion. b. $v = 1000 \mu\text{m/s}$ c. $v = 100 \mu\text{m/s}$ d. $v = 10 \mu\text{m/s}$. b. shows a case where mode B could be detected experimentally. For lower speeds (Fig. c) modes A and B are not resolvable but the combined distribution is broader than mode A alone. For even lower speeds (d) the distributions of particles in modes A and B are each wider than the separation between them and the two modes are completely unresolvable. The total number of particles is the same in each case and the initial distribution is a square distribution with width equal to the post separation $p = 10\mu\text{m}$	103
D.1 A. Sketch of epifluorescence layout. The broad excitation light source is filtered to the spectrum indicated by the excitation filter transmission curve in B. This same band is reflected by the dichroic mirror and then excites the fluorescent sample. Emission light is transmitted by the dichroic mirror and then is filtered before being detected at the camera. B. Transmission characteristics of the epifluorescence filter used in particle experiments.	121

CHAPTER I

INTRODUCTION

The persistent random motion of molecules in a fluid causes small objects in solution to move constantly on irregular paths, manifesting the thermal energy present in any system at finite temperature. At submicron length scales in aqueous solutions, the constant buffeting of the thermal bath leads to mean squared displacements of micron scale particles on the order of a micron per second (see Sec. 2.1). The randomness of this motion makes it a challenging proposition to control small objects in solution. The presence of thermal noise in solution also makes the function of biological molecular motors an impressive feat- biological motors generate directed motion in the noisy and complex environment of the cell [2, 3]. Such molecular motors are an inspiration for studying transport in thermal systems with microfabricated devices. To investigate transport in systems where diffusion is important, Brownian motion must be understood and quantified, and so background information about Brownian motion is discussed below in Sec. 1.1. Details of experimental measurements of diffusion and Brownian motion are discussed in Chapters II, V and VI. Systems that utilize thermal motion as an essential step in a cyclical process generating *directed* motion are called Brownian ratchets or Brownian motors [4, 5, 6, 3, 7, 8]. The flashing ratchet is the specific Brownian ratchet that is the focus of this work and it is introduced in Sec. 1.2, followed by a discussion of experimental precedents in the literature in Sec. 1.4. Chapter V includes detailed discussion of the Brownian ratchet experiments performed here using micron-scale particles in microfabricated array devices. Existing simulation work indicates that applying the flashing ratchet to a polymer (in place of a particle) will yield qualitatively different ratchet behavior [9]. After some opening remarks about

the predicted polymer ratchet mechanism in Sec. 1.5, the subject is covered more thoroughly in Chapter III. The experiments with λ DNA in electrode array devices to investigate the polymer ratchet are a main focus of this work. The culmination of microfabrication, imaging of individual DNA molecules and detailed analysis are presented in Chapter VI. An additional related project is introduced in Sec. 1.6 that shares the themes of transport and diffusion at the micron scale: modeling diffusion in deterministic lateral displacement arrays. The complete discussion of this work is found in Chapter VII.

Diffusion

The invention of the microscope allowed a window into the range of length scales where the effects of thermal motion on objects in solution become directly observable. Soon, researchers published descriptions of the skittering motion of small particles in aqueous solution at room temperature, including Ingen-Housz in 1784 [10] and Brown in 1828 [11]. The source of this motion was speculated upon, but no conclusive theory was presented at the time. In 1905, Einstein's description of diffusion linked the microscopic thermal motion of solvent molecules to the observable phenomenon of Brownian motion [12], leading towards our current understanding of diffusion as a stochastic process originating in thermal fluctuations of solvent molecules. The theoretical framework for understanding and measuring diffusion will be discussed in Chapter II.

Brownian Ratchets

One question often asked is if the microscopic thermal fluctuations can be somehow harnessed to generate work. At equilibrium, the answer is no. This is clear for the macroscopic case due to the second law of thermodynamics, but it's also

true for the less intuitive case of microscopic fluctuations, as was shown in a very accessible way by Feynman [13]. However, Curie showed (in the context of electron transport) that if spatial asymmetry is introduced into a thermal system that is *out of equilibrium*, in general, a current will be generated ([14] via [7]). Brownian ratchets generate transport by progressing cyclically through a series of states characterized by asymmetry and nonequilibrium [5, 6, 15, 3, 7, 8]. One example of such a system is the flashing ratchet discussed in 2.2, although there are several others, including ‘rocking ratchets’ whereby a sinusoidally varying, uniform force is added to an asymmetric ratchet potential [8, 16], and the ‘burned bridges’ ratchet where kinetic events prevent backwards stepping on a lattice [17]. The essential ingredients for transport in a Brownian ratchet are some kind of asymmetry (directional asymmetry for a flashing ratchet) and a mechanism to keep the system out of equilibrium. Brownian ratchets combine these ingredients to create directed motion in a thermal bath and do work.

Brownian Ratchet Case Study: The Flashing Ratchet

The flashing ratchet is one example of a Brownian ratchet system. The system consists of an ensemble of non-interacting particles in a thermal bath subjected alternately to an asymmetric, periodic potential and a flat potential. This sequence of events characterizing the flashing ratchet in one dimension is shown in Fig. 1.1. The potential is applied for the time period t_{ON} and the particles move to their equilibrium distribution, centered in each spatial period near the minima of potential. When the potential is off (t_{OFF}), particles are free to diffuse and do so isotropically. If the particles are allowed to diffuse sufficiently (see Chapter II), there is a net flux of particles when the potential is again turned on. The asymmetry in the potential allows appropriately timed switching (‘flashing’) of the potential to give systematic transport, in the positive x direction here. Repeated switching allows the flashing ratchet to achieve transport over distances much larger than the range of the forces

involved. Because both underlying potentials are spatially periodic, they necessarily have zero average force, and thus the flashing ratchet accomplishes macroscopic transport without the use of macroscopic potential gradients.

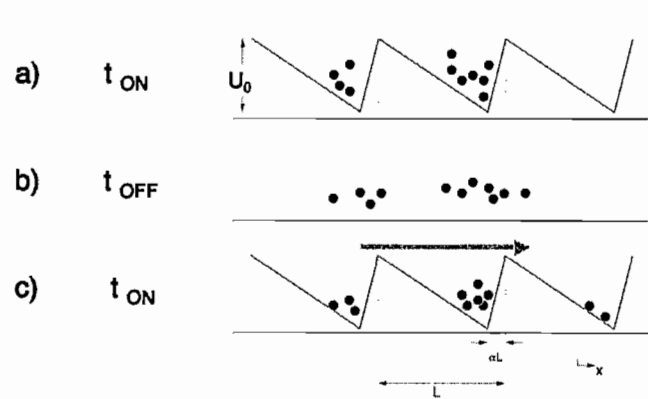


FIGURE 1.1: a) Particles in an asymmetric potential with period L , asymmetry α and amplitude $U \gtrsim k_B T$. b) When the potential is switched off, the particles diffuse isotropically. c) When the potential is switched on again, the asymmetry of the potential generates net motion of the particles in one direction as the new equilibrium distribution is reached. By repeating this cycle many times, macroscopic displacements can be achieved without the use of a macroscopic potential gradient.

Flashing Ratchet: Experimental Precedents

The flashing ratchet was first experimentally implemented in 1994 by Rousselet *et al.* [18] using an effective potential from dielectrophoretic forces on particles generated by AC voltages applied across a pair of periodic, asymmetrically shaped electrodes. Subsequent work showed similar transport by creating periodic, asymmetric optical trapping potentials for dielectric particles in solution [19, 16, 20, 21]. Also, Brownian ratchet transport has been observed in supported lipid bilayers above patterned surfaces [22].

In 1999, Bader and coworkers observed transport in an experimental system involving DC voltages applied across an array of interdigitated electrodes (such as

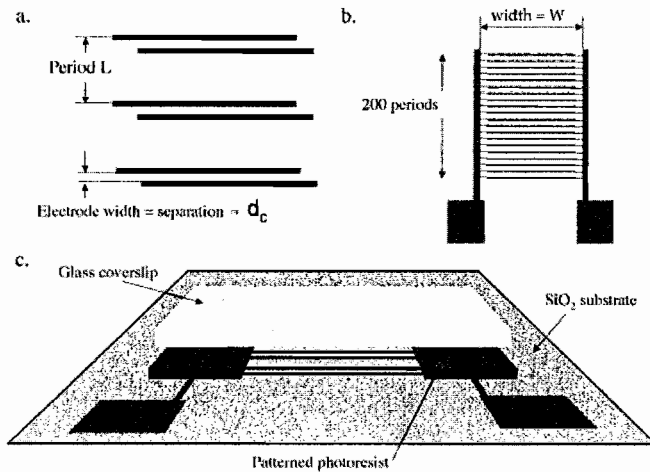


FIGURE 1.2: a. Interdigitated electrodes. For particle ratchet experiments described in Chapter V $L = 10 - 40\mu\text{m}$ and $CD = 1 - 4\mu\text{m}$. For the polymer ratchet discussed in Chap. VI, $L = 500\text{nm}$ and Electrode Width $\approx 50\text{nm}$. b. The electrode array dimensions are $W = 2\text{mm}$ for particle experiments and $W = 80\mu\text{m}$ for polymer experiments. c. Sketch of microchamber construction (for details see AppendixC)

those shown in Fig. 5.1) [23]. They used short (contour length $\approx 50\text{nm}$) pieces of fluorescently-labelled, single-stranded DNA as charged particles and obtained reasonable agreement between theory and their experimental results [24, 25]. The simplicity of this setup suggested an attractive platform for ratchet experiments and appeared to offer tantalizing possibilities as a lab-on-a-chip transport mechanism. One limitation of the early experiments studying Brownian ratchets, including the Bader experiments, is that only the spatial distribution of particles was observed, usually using the overall fluorescence intensity as an indicator of particle density. More recent work by Grier *et al.* is one exception to this in thermal ratchet work [20], but in the majority of experiments, individual particle trajectories were lost to ensemble measurement techniques. Here, by using fluorescent particles large enough to be resolved and individually tracked, the details of the ratchet mechanism underlying transport in an interdigitated electrode array system have been explored (see Chapter V).

Additionally, as discussed in Chapter III (and Sec. 1.5 below), more complex objects such as polymers are predicted to be transported in flashing ratchets [9], inspiring the polymer ratchet experiments described in Chapter VI. Although the random motion of diffusion would seem to be at odds with directed transport without macroscopic potential gradients, Brownian ratchet systems such as the flashing ratchet utilize thermal motion as an essential step in their transport processes. Brownian ratchets can output work (which is often the transport of an object through a viscous medium) only through the input of energy: the system must be kept out of equilibrium. In the case of the flashing ratchet, this is provided by an applied potential. The interdigitated electrode array devices have been chosen as the experimental system with which to investigate the flashing ratchet transport of particles and polymers.

The Polymer Ratchet

A natural extension of the flashing ratchet for particles is to investigate more complex structures subjected to the the same type of periodic, asymmetric potential. Theoretical and simulation work in this direction has included pairs of particles coupled by a harmonic potential [26], large ensembles of coupled particles [8], rigid rods [27] and polymers [9]. The last of these is of particular interest because the polymer contains many degrees of freedom within a single object, analogous to the internal degrees of freedom of processive biological molecular motors [3]. The simulation study of a polymer in a flashing ratchet potential in [9] revealed a novel ratchet transport mechanism and proposed an experimental system that could be feasible for testing the model's predictions. Chapter III discusses this model and its potential for experimental realization.

Transporting and Sorting Micron-scale Objects in Aqueous Solution

Diffusion and thermal motion make transport of small objects in solution a challenge: for micron-scale polystyrene particles used in ratchet experiments (see Chapter V), the characteristic diffusion length is about the size of the particle over 1 second. So diffusion must be taken into account in any process designed to transport such particles. With an eye to miniaturization of processes in bio-medical, sensing, or chemical research, much experimental focus has been placed on transporting objects in microfluidic channels, which can be loosely defined as any channels with at least one dimension in the 1-100 micron range. Microfluidics are also used in research for practical reasons. For example, monitoring small objects in solution is often accomplished with fluorescence microscopy- it's much easier to focus on an object confined to a microchannel than in bulk solution and also the fluorescence background and local environment can be better regulated in a microfluidic channel. Transporting objects through the use of macroscopic pressure gradients is often not ideal in microfluidic systems because the high hydrodynamic resistance of channels with micron-scale cross sections require large pressure gradients to transport liquid [28], and high hydrostatic pressures can easily rupture delicate microfluidic devices. Electrostatic potential gradients are similarly limited: the electrolysis of water can create bubbles in solution at voltages above 1.2 V, causing undesired fluid motion and introducing compressible gas into the system. In this context, methods to move small objects without macroscopic gradients are especially promising. The Brownian ratchet system discussed in Chapter II is an example of such a system: the flashing ratchet uses a potential with micron-scale periodicity in combination with diffusion to transport objects in solution.

Sorting micron-scale objects in aqueous solution at around room temperature has application in separating cells, viruses and macromolecules such as DNA without the addition of chemical labels. For example, separating white blood cells and red

blood cells from each other and from blood plasma based on hydrodynamic radius [29] or separating long, coiled DNA molecules of different sizes[30]. The separations described in [29] and [30] use a recently-developed technique called deterministic lateral displacement (DLD), described in detail in Chapter VII. In essence, DLD uses the bifurcating flows of fluid around obstacles in a microchannel to sort particles based on size (see Fig. 7.1). DLD has a few clear benefits over traditional separation techniques such as centrifugation or filtering: First, the sorted objects can be collected after separation while remaining in their original aqueous solution. Second, size range where DLD sorts effectively is many times smaller than the smallest gap in the device, so clogging is unlikely. Despite its benefits, DLD sorting is not immune to the effects of diffusion and work presented here addressing this issue discussed in Chapter VII.

CHAPTER II
THERMAL MOTION, BROWNIAN RATCHETS AND TRAJECTORY
ANALYSIS

Brownian Motion

Brownian motion is a mesoscopic manifestation of the microscopic thermal forces acting on a particle in solution. These forces are generated by random collisions of solvent molecules with the particle, and mathematically, the effect of these collisions on the particle's motion can be characterized by adding a random force $\xi(t)$ to the equation of motion for a particle in a viscous fluid:

$$F = m\ddot{x} = F_{external} - \gamma\dot{x} + \xi(t)$$

the thermal noise force is uncorrelated in time and taken from a Gaussian distribution [31].

$$\langle \xi(t)\xi(t') \rangle = k_B T \delta(t - t') \quad (2.1)$$

Experiments discussed later in Chapter V will involve polystyrene beads with a radius of $0.1\mu m$. By reorganizing Eq. 2.1, the momentum term can be isolated to estimate its importance. For such a particle at room temperature in water,

$$\dot{x} - \frac{F_{Applied}}{\gamma} = -\frac{m\ddot{x}}{\gamma} \approx (-10^{-9} s^{-1})\ddot{x}$$

which allows us to neglect the inertial term for timescales longer than $\approx (10^{-9} s^{-1})$ and work in the overdamped limit:

$$\dot{x} = \frac{F_{Applied}}{\gamma} \quad (2.2)$$

All of the analysis described below is in the overdamped limit because fluorescence microscopy of micron-scale particles does not allow resolution of any inertial dynamics. In the absence of an applied force, the motion of a particle in solution is random, giving rise to diffusion. Diffusion generally refers to the evolution of a spatial distribution $\rho(x, t)$ in time and is governed by the diffusion equation:

$$\frac{\partial \rho}{\partial t} = D \frac{\partial^2 \rho}{\partial x^2} \quad (2.3)$$

And for the polystyrene beads mentioned above, $D \approx 2\mu\text{m}^2/\text{s}$. Einstein's contribution to the understanding of Brownian motion was the realization that both the drag force, $-\gamma\dot{x}$, and diffusion were manifestations of collisions at the microscopic level. The connection can be formulated in the overdamped limit as [12]:

$$D = \frac{k_B T}{\gamma} \quad (2.4)$$

(Incidentally, this result was also published by William Sutherland a few months before Einstein [32], but the relation typically only bears Einstein's name.) Since Brownian motion is isotropic and the displacements are uncorrelated with each other, in the overdamped limit, the mean displacement of a particle is always zero:

$$\langle x \rangle_t = 0 \quad (2.5)$$

where the average here is the ensemble average, and the subscript t indicates that this is true for all times. The only caveat here is that this is strictly true for a single particle only for time scales where Eq. 2.2 holds. As shown by the classic random walk calculation, the square of the displacement does not vanish, but grows linearly with time.

$$\langle x^2 \rangle_t = 2Dt \quad (2.6)$$

This equation provides a method to directly measure D : simply record a particle's position over time and take the appropriate average. Measuring D from experimental trajectories (which are likely to include noise and statistical limitations) has some

notable complications that are relevant to this work and will be discussed in Sec. 2.3.1.

The Flashing Ratchet

The flashing ratchet was introduced in Sec. 1.3, and this more detailed description of its workings refers to the system described there, especially Fig. 1.1. The characteristic time scales for the processes involved in the on and off states can be derived from the particles' diffusion coefficient D , the strength of the potential, $U(x)$, its asymmetry, α , and L , the spatial period of the potential [23, 25]. The analysis below follows [23, 25, 6] and is divided into the times when the potential is on (1.) and off (2.).

1. Potential ON: Of interest here is the longest time needed for a particle to reach the minimum of the potential. The one-dimensional equation of motion for an overdamped particle in a fluid is given in Eq. 2.2. The particles' drag coefficient can be calculated using the Einstein relation Eq. 2.4, and the force applied on the particle in the piecewise-linear potential shown in Fig. 1.1 is just the derivative of the potential:

$$F_{Applied} = -\frac{\partial U(x)}{\partial x} = \begin{cases} \frac{U_0}{(1-\alpha)L} & (n-1)L < x < (1-\alpha)nL, n \in \mathbb{Z} \\ \frac{U_0}{\alpha L} & \text{otherwise.} \end{cases}$$

The time for a particle to move from 0 to $(1-\alpha)L$ is then

$$\tau_{ON} = \frac{\gamma(1-\alpha)^2 L^2}{U_0} \quad (2.7)$$

Where U_0 is the maximum of the potential $U(x)$. For the case of individual particles that are small compared to αL , the direction of transport will always be along the longer slope. For the flashing ratchet transport of objects with extent

comparable to the dimensions of the ratchet, the effective potential experienced by the object can have different asymmetry from the ratchet potential. This can lead to transport reversals as a function of size in flashing ratchet systems [27].

2. Potential OFF: The characteristic time τ_{OFF} is the time needed for particles to diffuse the distance from a potential minimum to the nearest maximum: particles that make it this far during t_{OFF} will then contribute to the net motion. For $U_0 \gg k_B T$, the distribution is confined near the minimum and the initial condition for the probability density $\rho(x, t)$ can be taken as a delta function at the minimum located at $x = 0$.

$$\rho(x, t = 0) = \delta(x) \quad (2.8)$$

After a time Δt , the distribution is given by

$$\rho(x, \Delta t) = \frac{e^{-\frac{x^2}{4D\Delta t}}}{\sqrt{4\pi D\Delta t}} \quad (2.9)$$

By setting the width of this Gaussian distribution equal to the distance between a minimum and the nearest maximum we can estimate τ_{OFF} . The characteristic time during which the ratchet potential should be off comes out as

$$\tau_{OFF} = \frac{(\alpha L)^2}{2D} \quad (2.10)$$

The motion of the center of mass of the distribution can be used to calculate the average flux of particles in response to switching. In the limit of very good confinement, all particles end up at the minima when the potential has been on for longer than τ_{ON} . First, consider the case where $t_{OFF} \gg \tau_{OFF}$ and so the distribution is essentially flat by the time the potential is turned on again. For a flat distribution, the center of mass in each period is just at $L/2$, so if all particles are then confined

to the minimum at the end of t_{ON} , we can write down the velocity per cycle:

$$|v_{cycle}| \equiv \frac{\Delta x}{t_{cycle}} = \frac{\frac{L}{2} - \alpha L}{t_{ON} + t_{OFF}} \quad (2.11)$$

This provides an upper bound for the ratchet displacement per cycle for a given t_{ON} and t_{OFF} : poor confinement will reduce the effective asymmetry by moving the center of mass towards $L/2$ and a finite t_{OFF} will lead to less spreading during the off state. Since the center of mass does not move during the off state, the effect of t_{OFF} on the velocity is through the shape of the distribution. For $t_{OFF} < \tau_{OFF}$, where $\rho(|x| \geq L, t_{OFF}) \approx 0$, we can write f , the fraction of particles that move in the transport direction, as

$$f = \int_{-\infty}^{-\alpha L} \rho(x, t_{OFF}) dx = \frac{1}{2} \operatorname{erfc} \left(\sqrt{\frac{\alpha^2 L^2}{4Dt_{OFF}}} \right) \quad (2.12)$$

where ‘erfc’ is the complementary error function. The remaining fraction of the distribution will stay in the same potential minimum when the potential is again turned on, while the fraction f will travel a full period L to the next minimum, so the net center of mass motion will be given by

$$v_{net} = \frac{fL}{t_{ON} + t_{OFF}} = \frac{L}{2(t_{ON} + t_{OFF})} \operatorname{erfc} \left(\sqrt{\frac{\alpha^2 L^2}{4Dt_{OFF}}} \right) \quad (2.13)$$

In terms of an absolute velocity, t_{ON} and t_{OFF} must be optimized for particular experimental conditions. In the context of experiments in Chapter V, confinement and velocity per cycle is sufficient detail to analyze the observed particle motion.

Trajectory Analysis

The experiments (discussed in detail in Chapter V) involve collecting images of diffusing particles using fluorescence microscopy. The details of locating objects in images and assembling their positions into individual trajectories is discussed

in Appendix A, but with trajectories in hand, the work of extracting quantitative physical information from experimental data can begin. In the present context, the important characteristics of the object include its diffusion coefficient, D , the mean velocity, $\langle v \rangle_t$, and the displacement, $\langle \Delta x \rangle_t$, of an ensemble of particles when the number of particles visible in an image may vary over time. These quantities and the methods to calculate them will be discussed in detail here and the interpretation of the results will form substantial parts of Chapters V and VI.

Measuring Diffusion Coefficients from Trajectories

For any ensemble of identical diffusing particles, calculating D is simple in theory: it is the slope of a graph of mean square displacement (see Eq. 2.6). For a time between measurements, Δt_{test} , the displacements are sampled from the Gaussian probability distribution, $\rho(\Delta x, \Delta t_{test})$ given in Eq. 2.9, which is the normalized solution to the diffusion equation (Eq. 2.3). It may seem that a measurement of D would require only two position measurements, since a displacement Δx_{test} and corresponding time Δt_{test} can be combined as follows

$$D_{test} = \frac{\Delta x_{test}^2}{2\Delta t}. \quad (2.14)$$

to give D . Since diffusion is a random process, the actual measured value, Δx_{test}^2 is a random value sampled from $\rho(\Delta x, \Delta t_{test})$. To overcome the noise associated with the random process, it's tempting to let Δt be as large as possible (increasing the 'signal', Δx_{test}^2). However, since all the non-zero moments of $\rho(\Delta x, \Delta t_{test})$ share the same time dependence, the variance in $\langle \Delta x_{test}^2 \rangle$ is also proportional to Δt . This means that the signal-to-noise ratio from D calculated this way doesn't increase with increasing Δt , in fact, the signal to noise ratio is $2^{-1/2}$, which is less than one [33]. This inherent broadening of the distribution of Δx_{test}^2 is clearly visible in Fig. 2.1, which illustrates the squared displacements of 12 particles in a microchannel. Simply measuring Δx_{test}^2 after a single Δt is not a good method to measure D because the distribution of measured D 's is wider than the value itself.

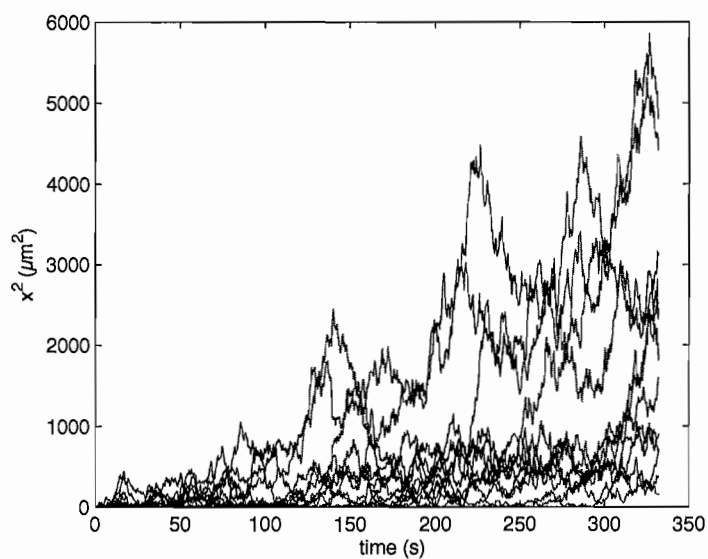


FIGURE 2.1: Squared displacements of 12 $0.2\mu m$ -diameter particles in a $1.5\mu m$ -deep microchannel. The range of squared displacements increases linearly with time. These 12 particles were all present in the field of view for 1000 frames collected at about 3 frames/sec.

But the above method only uses two data points and thus ignores much of the data in the experimentally measured trajectory. One way to include the large number of intervening data points is to divide each trajectory into a sequence of shorter trajectories of length Δt . If these segments are adjacent to each other (as indicated in Fig. 2.3.1), they are statistically independent and so the mean square displacement measured N times in this way has an error associated with it proportional to $\sqrt{1/N}$, specifically, the standard deviation is $2D\Delta t\sqrt{2/N}$ [33]. So the error in D is minimized by measuring the mean square displacement for the smallest Δt . Slightly different estimates on D can be obtained by using a sliding time window Δt instead of the uncorrelated adjacent Δt s. This technique of oversampling can make mean square displacement data easier to fit, but the individual data points for a given Δt are then correlated. Appropriate error and related subtleties associated with oversampling are discussed extensively in [33].

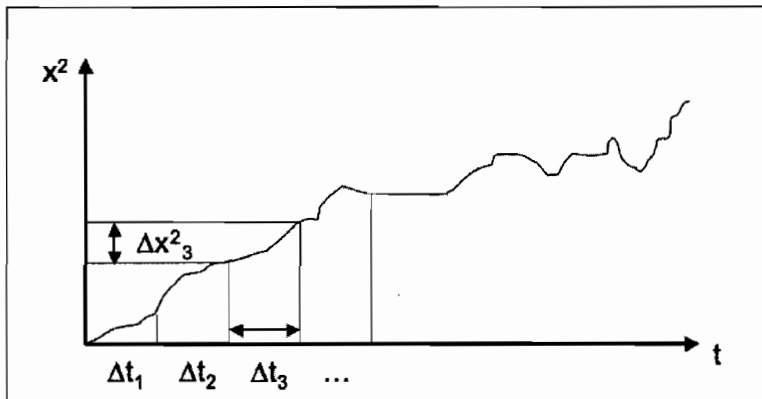


FIGURE 2.2: Sketch of a trajectory divided into adjacent segments of Δt for square displacement analysis.

However, in experiments, there is also error associated with each particle position measurement, which further complicates the process of estimating D from trajectories. Each measured position x_i can be written as

$$x_i = \tilde{x}_i + \epsilon_i \quad (2.15)$$

where \tilde{x}_i is the actual position and ϵ_i is the measurement error. The i^{th} measurement error ϵ_i is not correlated with any position or any other errors:

$$\langle \epsilon_i \tilde{x}_j \rangle = 0 \quad \langle \epsilon_i \epsilon_j \rangle \equiv \sigma^2 \delta_{ij} \quad (2.16)$$

where σ^2 will be discussed below. How does this error affect measured mean displacements?

$$\Delta x_i \equiv x_{i+1} - x_i = \tilde{x}_{i+1} + \epsilon_{i+1} - \tilde{x}_i + \epsilon_i$$

$$\Delta x_i \Delta x_j = (\tilde{x}_{i+1} + \epsilon_{i+1} - \tilde{x}_i - \epsilon_i) \cdot (\tilde{x}_{j+1} + \epsilon_{j+1} - \tilde{x}_j - \epsilon_j)$$

$$= (\tilde{x}_{i+1} - \tilde{x}_i)(\tilde{x}_{j+1} - \tilde{x}_j) + \epsilon_i \epsilon_j + \epsilon_{i+1} \epsilon_{j+1} - \epsilon_i \epsilon_{j+1} - \epsilon_j \epsilon_{i+1}$$

+ cross terms with x and ϵ

$$(2.17)$$

And now the expectation values

$$\langle \Delta x_i \Delta x_j \rangle = \langle \Delta \tilde{x}_i \Delta \tilde{x}_j \rangle + \langle \epsilon_i \epsilon_j \rangle + \langle \epsilon_{i+1} \epsilon_{j+1} \rangle$$

for $i = j$ we have

$$\langle \Delta x^2 \rangle = 2D\Delta t + 2\sigma^2 \quad (2.18)$$

This means that errors in position measurements introduce a *systematic* bias in D calculated from trajectories [33]. Fortunately, this error can be quantified from the measured positions:

$$\langle \Delta x_i \Delta x_j \rangle = -\epsilon_i \epsilon_{j+1} - \epsilon_j \epsilon_{i+1} = -\sigma^2$$

for $i = j + 1$

$$(2.19)$$

Eq. 2.19 shows that adjacent displacements Δx_i and Δx_{i+1} are correlated because of the error in the position measurement shared by both displacements. By calculating $\langle \Delta x_i \Delta x_{i+1} \rangle$ from an experimentally measured trajectory, the systematic error introduced into D by imperfect position measurements can be quantified and then eliminated.

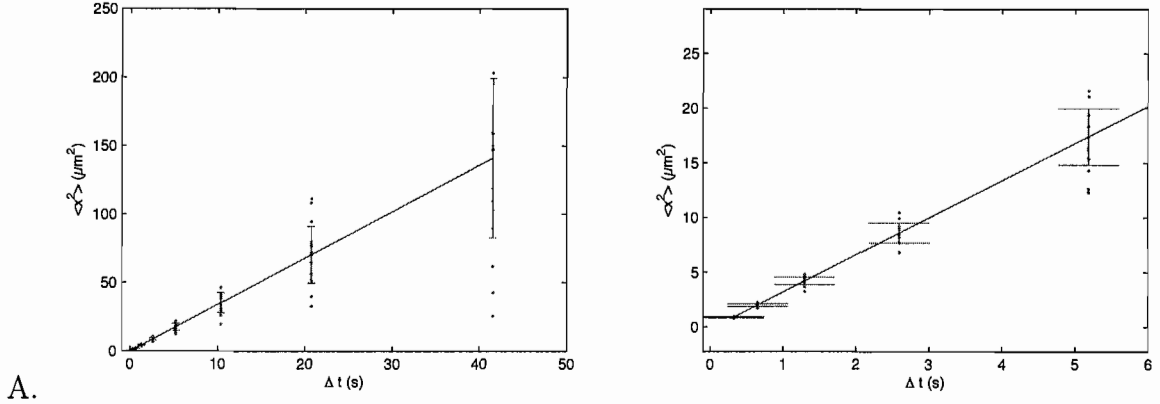


FIGURE 2.3: A. Mean squared displacement $\langle \Delta x^2 \rangle$ for 12 particles plotted versus Δt . The line plotted is $2D\Delta t$ using D calculated as described in the Sec. 2.3.2. B. The same data near the origin.

Summary: Method for calculating D

The statistical and systematic constraints on calculating D discussed above can be effectively dealt with using the following prescription:

- Collect particle trajectories.
- Calculate $\langle \Delta x^2 \rangle$ as a function of Δt
- Calculate $\langle \Delta x_i \Delta x_{i+1} \rangle$ for each Δt used. This then yields σ^2 , the error in $\langle \Delta x^2 \rangle$ due to error in position measurement.
- Subtract the appropriate σ^2 from each measured $\langle \Delta x^2 \rangle$
- Calculate D using the corrected $\langle \Delta x^2 \rangle$ corresponding to the smallest Δt

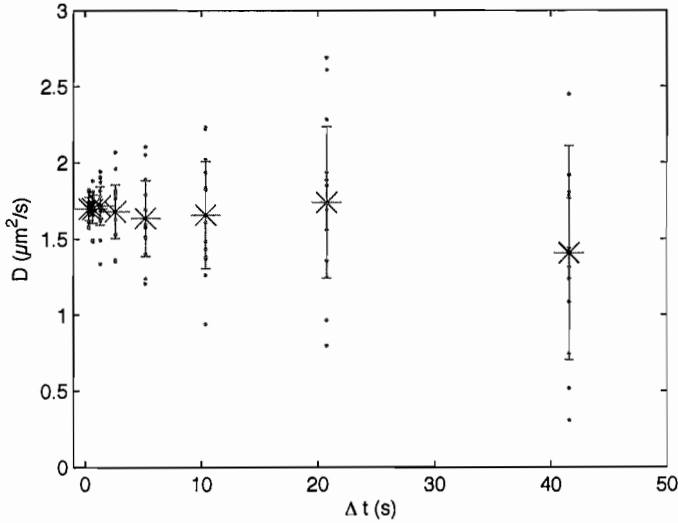


FIGURE 2.4: Calculated values of D with error bars for the data shown in Figures 2.3 and 2.1.

- The error in D is given by $2D\Delta t\sqrt{2/N}$, where N is the total number of samples associated with the smallest Δt .

Mean Displacement

Whether due to diffusion or drift, particles often enter and leave the field of view. This leads to situations where the average position of all particles is not a useful quantity to track as a function of time. For example, uniform particle density and uniform flux in one direction clearly corresponds to a net displacement at all times, but the center of mass in each frame would be close to the center of the image for all frames and show no net transport. Instead of tracking the mean position of the visible particles as a function of time, the mean displacement $\langle \Delta x \rangle_t$ can be calculated using the velocity of all visible particles in each frame, $\langle v \rangle_i$.

$$\langle v \rangle_i = \frac{1}{n_t} \sum v_k \quad (2.20)$$

where the sum indicated is over all particles visible in the i^{th} frame. This quantity is cumulatively summed over the image sequence to give the mean displacement \langle

$\Delta x >_i$:

$$\langle \Delta x \rangle_i \equiv \langle v \rangle_i \Delta t_i + \sum_{j=1}^{i-1} \langle v \rangle_j \Delta t_j \quad \langle \Delta x \rangle_t = \frac{\langle \Delta x \rangle_i}{f} \quad (2.21)$$

where f is the frame rate.

Mean Velocity

The mean velocity is calculated by averaging over all particles moving in each frame (see Eq. 2.20). To show the particles' response to the applied potential, this quantity is graphed alongside the potential in Fig. 5.3. Fig. 5.3 also averages the mean velocity over all of the temporal periods of the voltage.

CHAPTER III

POLYMERS IN A FLASHING RATCHET

Polymer Ratchet Model

As mentioned in Chapter I, the flashing ratchet idea has been applied to more than just independent particles in solution [26, 8, 27, 9]. The key results from the numerical simulations in [9] are discovery of a novel ratcheting mechanism and quantitative estimates for physical parameters accessible in an experiment. The simulation used a Rouse model for the polymer, specifically $N \approx 50$ masses linked by a spring-like potential. The masses each have a drag coefficient γ and are subjected to thermal noise, viscous drag, the coupling force between links of the polymer and the applied ratchet potential. A wide range of ratchet parameters were discussed in the publication and the only the essential points are recapitulated here.

Novel Ratchet Mechanism

The most intriguing result published in [9] is the discussion of a new mechanism of transport in a flashing ratchet. The steps leading to transport of a polymer in a flashing ratchet are as follows:

1. Potential Off: The polymer is in an equilibrium coil configuration with a characteristic size larger than, but on the order of a ratchet period L .
2. Potential On: The polymer density is spread over several ratchet periods and partially confined to the minima. Due to the asymmetry of the ratchet potential, the confinement process includes a slight shift of the center of mass.

3. Potential Off: The polymer returns to its equilibrium coil configuration and the system is returned to state 1.

As with the particle ratchet, transport on arbitrary length scales can be achieved by repeatedly ‘flashing’ the potential. The polymer’s motion in response to the applied potential is also similar to the particle’s: the polymer’s center of mass moves a fraction of the period L as it equilibrates in the ratchet potential. The difference between transport in the particle and polymer ratchets is the mechanism by which the system ‘resets’ during t_{OFF} . When the potential is turned off, the polymer relaxes to an equilibrium coil configuration which, on average, is radially symmetric. This equilibration allows the ratchet to return to its initial state so the ratchet cycle described above can be repeated. In contrast to the particle ratchet, which resets through center-of-mass diffusion, this novel ratchet mechanism relies on a different reset mechanism: the relaxation of the internal degrees of the polymer. A particle in the ratchet must diffuse the distance αL during t_{OFF} in order to achieve net transport over a temporal cycle of the ratchet potential, and the longer a particle takes to diffuse the short distance αL of the ratchet during t_{OFF} , the slower its overall velocity. Since

$$D = \frac{k_B T}{6\pi\eta r}, \quad (3.1)$$

the first passage time for a particle from a minimum to the nearest maximum is just

$$\Delta t = \frac{3\pi\eta r \alpha^2 L^2}{k_B T}, \quad (3.2)$$

which is inversely proportional to the particle’s radius r . Data in [9] show that polymers modeled as Rouse chains with $N > 20$ are transported faster in a flashing ratchet than single particles with the same diffusion constant as the polymer.

The internal dynamics of the polymer are easily accessible in simulation data because the position of every monomer is calculated in each time step. This allows for observation of conformational changes associated with ratcheting, specifically the excitation of low Rouse modes in response to the applied potential. Rouse modes are

a convenient basis for expressing the dynamics of polymer chains [34]. The position \mathbf{R}_n of the n^{th} monomer in a chain of N monomers linked together can be transformed into the basis of Rouse modes \mathbf{X}_p :

$$\mathbf{X}_p = \frac{1}{N} \sum_{n=1}^N \cos\left(\frac{p\pi(n-1)}{N-1}\right) (\mathbf{R}_n - \mathbf{R}_{cm}) \quad (3.3)$$

where \mathbf{R}_{cm} is the center of mass position. The amplitude of the first two Rouse modes along the direction of transport is shown in [9] to increase during temporal cycles of the potential when the polymer is transported. This indicates that long wavelength conformational changes (small p in the above definition) accompany ratchet transport of a polymer. These conformational changes could provide qualitative measures of ratchet behavior in an experimental realization of a polymer ratchet.

Experimental Relevance

Although interesting in its own right from a statistical mechanics point of view, creating an experimental realization of such a system requires more from the simulation than just qualitative information. To assess the applicability of their work to experiment, the authors of [9] scaled the results of the simulations into physical units, choosing DNA as the polymer because of its negative charge in solution and commercial availability. Their simulations indicate that λ DNA (contour length $\approx 16\mu m$) would require a maximally asymmetric ratchet potential with a spatial period $L \approx 0.2-0.6\mu m$. This range of L with asymmetry $\alpha \approx 0.3$ is experimentally accessible using interdigitated electrode arrays fabricated with electron beam lithography (EBL) techniques. With this information in hand, experimental investigations of λ DNA above interdigitated electrode arrays were undertaken. The experiment and its results are discussed in detail in Chapter VI

CHAPTER IV

BACKGROUND: RELEVANT PHYSICAL CHEMISTRY OF AQUEOUS SOLUTIONS

Introduction

In most physics texts and courses, Brownian motion takes place in a ‘thermal bath’, a term which evokes the image of water. The concept of a thermal bath is convenient for physicists because of what it doesn’t include: any kind of chemistry or material properties that may characterize an actual solvent. However, the experiments described in Chapters V and VI take place in aqueous solutions and some of the properties of this environment must be considered. Specifically, the behavior of ions and the screening of electrostatic charges in solution will be discussed here.

pH and Ions in Solution

Liquid water partially autodissociates into ions in solution, of which H_3O^+ and OH^- are the most stable. In the absence of other additives, the dissociation constant of water, k_{H_2O} determines the concentrations of H_3O^+ and OH^- in solution. The concentrations of these highly reactive ions determines much of the chemical activity of a solution. The negative log of concentration of H_3O^+ (written $[H^+]$) was developed by S. P. L. Sørensen in 1909 as a means of quantifying the acidity or alkalinity of a solution [2, 35]:

$$pH = -\log_{10}([H^+]) \quad (4.1)$$

At room temperature, $[H^+]$ is about 10^{-7} mols/liter, giving the familiar pH of 7 for pure water. Of course other ions can be introduced into aqueous solution, a common example being the dissociation of ionic solids such as NaCl into Na^+ and Cl^- in water. To describe the overall concentration of ions in solution, the ionic strength, I , is defined as follows:

$$I \equiv \frac{1}{2} \sum_i n_i z_i^2 \quad (4.2)$$

where z_i and n_i are the charge and concentration of the i^{th} ion in solution. Electrolytes such as *NaCl* where the dissociation is complete and there are equal numbers of ions with single positive and negative charges are called 1:1 electrolytes. In cases where the salt concentration is higher than 10^{-6} M, the concentrations of H^+ and OH^- do not contribute substantially to the ionic strength, and so I is just given by the concentration of salt, $[NaCl]$.

DNA in Solution

Another important case of dissociation in water involves the charge of *DNA* molecules in solution. Double-stranded DNA (deoxyribonucleic acid) is a polymer composed of two phosphate-sugar backbones (the sugar is 2-deoxyribose) linked by pairs of complementary nucleotide bases, as indicated in Fig. 4.1.

The phosphate groups dissociate in water, releasing a proton into solution, where it combines with water to form H_3O^+ and lower the pH (hence the ‘acid’ in ‘deoxyribonucleic acid’). The dissociation leaves the DNA backbone charged with $-2q_e$ per base pair. The oppositely charged ions in solution are called counterions and their behavior and effect on electric potentials in solution is discussed below.

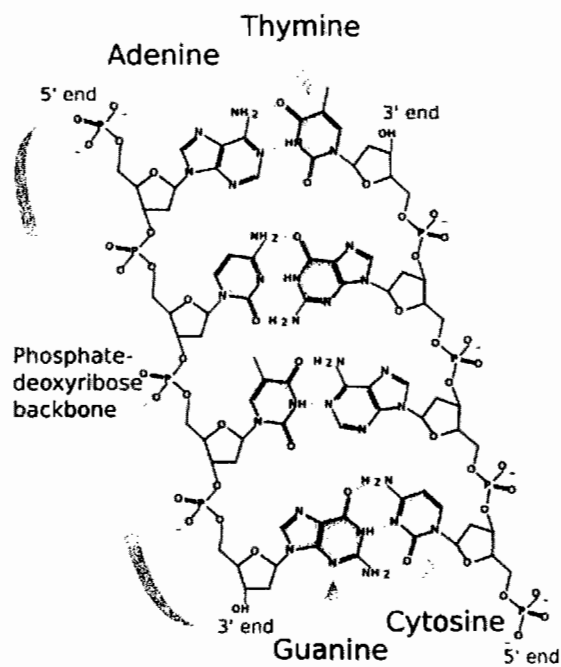


FIGURE 4.1: The chemical structure of DNA showing the paired nucleic bases (guanine-cytosine and adenine-thymine) connecting the two phosphate-sugar backbones. Image from [1]

Electrostatic Screening

The presence of these free ions in solution, even when they are at thermal equilibrium, introduces new complexity to electrostatics. The thermal and electrostatic forces must both be considered to determine the equilibrium distribution of ions in solution. The Poisson-Boltzmann equation is the primary tool for dealing with these conditions in the continuum limit where ions in solution can be summarized as a smoothly varying charge (or number) density. The purpose of this section is to show the foundation of the screening of charges by ions in solution. The derivation presented below follows that in [36].

The Poisson-Boltzmann Equation

The electrostatic potential $\Phi(\mathbf{r})$ is related to the charge density $\rho(\mathbf{r})$ through the Poisson equation:

$$\nabla^2 \Phi(\mathbf{r}) = \frac{\rho(\mathbf{r})}{\epsilon \epsilon_0} \quad (4.3)$$

Where ϵ and ϵ_0 are the permittivity of free space and the dielectric constant of the solution, respectively. The Poisson equation covers electrostatics, but in addition, the statistical mechanics of the ions in solution must be dealt with. Consider the case of 1:1 electrolytes with equal concentration of positive ions, n_+ , and negative ions, n_- , with charge zq_e , where $z = \pm 1$ and both equal to the salt concentration n_0 . The equilibrium densities of negative ions $\rho(\mathbf{r})_-$, and positive ions, $\rho(\mathbf{r})_+$, are determined by Boltzmann statistics:

$$\rho(\mathbf{r})_- = q_e n_0 e^{\frac{+ze\Phi(\mathbf{r})}{k_B T}}$$

and

$$\rho(\mathbf{r})_+ = q_e n_0 e^{\frac{-ze\Phi(\mathbf{r})}{k_B T}}.$$

These two give the total charge density

$$\rho(\mathbf{r}) = \rho(\mathbf{r})_+ - \rho(\mathbf{r})_-$$

$$\begin{aligned}\rho(\mathbf{r}) &= q_e n_0 \left[e^{-\frac{e\Phi(\mathbf{r})}{k_B T}} - e^{\frac{e\Phi(\mathbf{r})}{k_B T}} \right] \\ \rho(\mathbf{r}) &= -2q_e n_0 \sinh\left(\frac{e\Phi(\mathbf{r})}{k_B T}\right)\end{aligned}\quad (4.4)$$

This can be combined with Eq. 4.3 to give the Poisson-Boltzmann equation:

$$\nabla^2 \Phi(\mathbf{r}) = -\frac{2q_e n_0}{\epsilon \epsilon_0} \sinh\left(\frac{e\Phi(\mathbf{r})}{k_B T}\right) \quad (4.5)$$

The Poisson-Boltzmann equation is typically expressed nondimensionally through the use of a potential scaled to $k_B T$

$$\phi(\mathbf{r}) = \frac{e\Phi(\mathbf{r})}{k_B T}$$

and a dimensionless length

$$\tilde{\mathbf{r}} = \mathbf{r} \sqrt{\frac{2q_e^2 n_0}{\epsilon \epsilon_0}}$$

giving

$$\nabla^2 \phi(\tilde{\mathbf{r}}) = \sinh \phi(\tilde{\mathbf{r}}) \quad (4.6)$$

The length used here defines the Debye length, λ_{Debye} :

$$\lambda_{Debye} \equiv \sqrt{\frac{\epsilon \epsilon_0}{2q_e^2 n_0}}$$

so

$$\tilde{\mathbf{r}} = \frac{\mathbf{r}}{\lambda_{Debye}} \quad (4.7)$$

And changing the units of n_0 from number volume density to concentration, it is found that

$$\lambda_{Debye} = \sqrt{\frac{\epsilon \epsilon_0}{2q_e^2 N_A (10^{-3}) I}} \quad (4.8)$$

where I is the ionic strength from Eq. 4.2 and N_A is Avagadro's number. A few values for λ_{Debye} for various ionic strengths are shown in Sec. 5.6.2.

The Poisson-Boltzmann equation is limited in a few respects:

- It requires that the continuum limit is valid, i.e. N_{test} , the number of ions in a relevant volume must be large enough that $\sqrt{N_{test}}$ number fluctuations are much smaller than N_{test} .
- ϵ must be constant and isotropic (or else Eq. 4.3 must be modified).
- It is nonlinear in ϕ and difficult to solve analytically.

The process of linearizing the Poisson-Boltzmann equation gives the Debye-Hückel approximation, which is described below.

The Debye-Hückel Approximation

The problematic term in Eq. 4.5, $\sinh \phi(\tilde{\mathbf{r}})$, can be expanded to linear order in $\tilde{\mathbf{r}}$ to give

$$\nabla^2 \phi(\tilde{\mathbf{r}}) = \phi(\tilde{\mathbf{r}}) \quad (4.9)$$

This approximation is only as valid as the expansion $\sinh z \approx z$, which is to within 1% for $z < 0.25$. This delineates the Debye-Hückel regime:

$$0.25 > \phi$$

or, equivalently,

$$q_e \Phi < 0.25 k_B T \quad (4.10)$$

This regime is of interest mostly because Eq. 4.9 is much more tractable than Eq. 4.5 and gives solutions in several geometries. One case of particular interest is cylindrical symmetry, where Φ only depends on s the distance from the z -axis. This is a useful approximation for the potential due to an infinite line of charge. In this case, Eq. 4.9 becomes

$$\tilde{s}^2 \frac{d^2}{d\tilde{s}^2} \phi(\tilde{s}) + \tilde{s} \frac{d}{d\tilde{s}} \phi(\tilde{s}) - s^2 \phi(\tilde{s}) = 0 \quad (4.11)$$

where \tilde{s} is the nondimensional distance from the z axis, scaled again by the Debye length λ_{Debye} . This equation is a zeroth order modified Bessel equation [37], which has

the modified Bessel function of the second kind, K_0 , as its only solution that is well behaved at large \tilde{s} , so $\phi(\tilde{s}) \propto K_0(\tilde{s})$. $K_0(\tilde{s})$ is a monotonically decreasing function of \tilde{s} that approaches $\sqrt{\frac{\pi}{2\tilde{s}}}e^{-\tilde{s}}$ [37]. (This last approximation is within 1% of $K_0(\tilde{s})$ around $\tilde{s} = 10$.) Returning to the original variables, s and Φ ,

$$\Phi(s) \propto \frac{1}{s^{1/2}} e^{\frac{s}{\lambda_{Debye}}} \quad (4.12)$$

This final form exhibits the screening effect of ions in solution: regardless of the value of the potential at the z -axis (which just determines prefactors [36]), $\Phi(s)$ decreases (slightly faster than) exponentially with s and λ_{Debye} is the characteristic length scale.

Φ near a charged object

The Debye-Hückel approximation breaks down for values of $e\Phi$ larger than about $0.25k_B T$, so Φ at room temperature must be less than about $6mV$. In regions close to highly charged objects such as λ DNA in solution, $\Phi(r)$ must be calculated by solving Eq. 4.5 numerically. The prefactors of the true $\phi(\tilde{r})$ (solution to the Poisson-Boltzmann equation) and the prefactor for $K_0(\tilde{r})$ (solution to the linearized Poisson-Boltzmann equation) are both set by boundary conditions at a point near the z -axis, (usually the physical extent of the object). Results from numerical solutions to the full Poisson-Boltzmann equation show that $K_0(r)$ underestimates $\Phi(r)$ at $r = \lambda$ by less than a factor of 2, even when the value of $\phi(\tilde{r})$ at the boundary is six times that of the solution to the linearized equation [38]. In conclusion, $K_0(\tilde{r})$ is a good estimate for the actual $\phi(\tilde{r})$, with the caveat that $\phi(\tilde{r})$ is greater (and decays faster) near the charged object than $K_0(\tilde{r})$. Additionally, the exponential screening of potentials in solution ($\phi(\tilde{r}) \propto e^{-\tilde{r}}$) gives an *low* estimate of the rate of decay of ϕ for cylindrical symmetry, so the exponential falloff of ϕ gives a strong upper bound on the potential in solution. This rapid decay of ϕ in solution is relevant to the discussion of electrode screening in Chapter V.

CHAPTER V

PARTICLE EXPERIMENTS AND RESULTS

Introduction

As discussed in Sec. 1.4, several different methods have been used to experimentally realize Brownian ratchet transport [23, 24, 22, 18, 19, 20]. The experimental precedent set by Bader, *et al*, who reported Brownian ratchet transport of charged particles in solution above interdigitated electrode arrays, was introduced in Sec. 1.4. This result was the primary impetus for pursuing the use of interdigitated electrode arrays to create ratchet potentials for objects in solutions [23, 24, 25]. This work inspired a range of experimental ideas, including the proposed use of many charged polymers such as DNA in a flashing ratchet to generate macroscopic forces. As a preliminary step to characterize the putative ratchet potential above interdigitated electrode arrays, carboxylate-modified polystyrene microspheres were used as test particles. The $0.2\mu\text{m}$ diameter, fluorescent particles allowed for tracking of individual particles using fluorescence microscopy- something needed to understand the potential in detail. The use of particle tracking to quantify the motion of individual particles in the experiments described here has revealed a much more complex picture of the dynamics in interdigitated electrode array systems than the description presented in the literature by Bader, *et al*, [23, 24, 25]. Their work describes the only other ratchet transport experiments using interdigitated electrode arrays, and their experiment only measured overall fluorescence intensity, which is proportional to the density of the fluorescent particles they were investigating.

The wide range of behaviors exhibited by this relatively simple system of electrodes

and particles will be addressed here by comparing the observations to predictions for flashing ratchet transport made in Sec.2.2 to more complex phenomena associated with applying an electrostatic field in aqueous solution using an array of electrodes. The initial investigations of particles in interdigitated electrode array devices were done in deionized water to reduce counterion screening as much as possible, but later experiments varied ionic strength to investigate the phenomena underlying observed transport in response to an applied flashing potential. In particle experiments, fluorescence microscopy can easily resolve the interdigitated electrodes and provide direct information about the effect of the potential on objects in solution. Overall, the picture that has emerged from analysis of this experimental system is not easily characterized by a single dominant effect, but rather, exhibits an interplay between electrostatics, hydrodynamics and chemical phenomena.

Experiment Protocol

Interdigitated arrays of metal electrodes on silicon oxide surfaces sketched in Fig. 5.1 were fabricated using the lithography methods described in Appendix C. The microchannel above the electrode array (depth $h \approx 1.6\mu m$) was created by sealing a coverslip across the patterned photoresist. After creating the microchannel, a small ($\lesssim 0.5\mu L$) drop of the bead solution was placed on the chip surface at the end of the channel where, once in contact with the edge of the coverslip, it was drawn into the microchannel by capillary action. The ends of the microchannel were then sealed with vacuum grease to prevent evaporation. Images of particles were collected with the CCD camera and microscope setup described in Appendix D. Voltages were brought to the electrode arrays using needle probes in manual x-y-z micrometer stages.

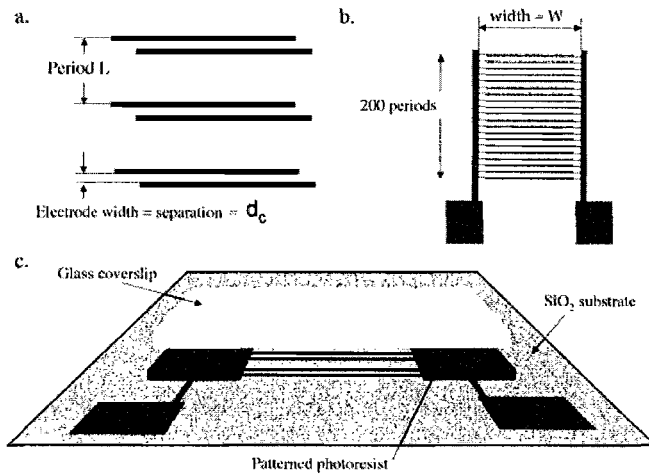


FIGURE 5.1: a. Interdigitated electrodes. For particle ratchet experiments, $L = 10 - 40\mu m$ and $d_c = 1 - 4\mu m$. b. The electrode array dimension $W = 2\text{ mm}$ for particle experiments. c. Sketch of microchamber construction.

Observations in Particle Experiments

Brownian Motion

Before any potential is applied, Brownian motion of the particles is recorded. The image sequences are processed as discussed in Appendix AA and the resulting trajectories are then analyzed using the method described in Sec. 2.3.1. Measured particle locations are overlaid on an image of the interdigitated electrode array in Fig. 5.2.

The measured value of the diffusion coefficient $D = 1.7 \pm 0.1\mu^2/s$. The value predicted by the Einstein relation (Eq. 2.4 and Stokes' formula is $D_{Stokes} = 2.2\mu m^2/s$. However, the stick boundary condition on the nearby microchamber walls provides a correction to the measured diffusion coefficient in the microchannel :

$$D_{measured} = D_{Stokes} \left(1 + \frac{9}{16} f \ln f - 1.19358f + O(f^3) \right)$$

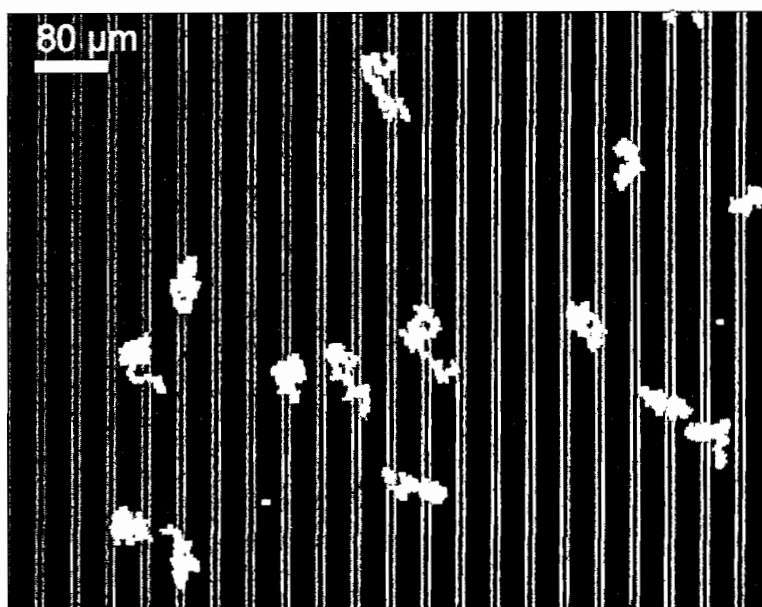


FIGURE 5.2: Particle locations from 1000 images of $0.2 \mu\text{m}$ -diameter particles overlaid on an image of the interdigitated electrode array.

where

$$f = \frac{2r}{h} \quad (5.1)$$

with r the particle radius and h the microchannel height [39]. For a microchannel thickness of about $1.6\mu\text{m}$ and a $0.1\mu\text{m}$ radius particle, $f = 0.125$ and this correction gives a predicted value of $D_{measured} = 1.55\mu\text{m}^2/s$.

Particle Motion in Response to Applied Potential

The quantities discussed in Sec. 2.3 change as voltages are applied across the electrode array and the details of that response, including variation with ionic strength and applied voltage are described below. Discussion of these results follows in Sec. 5.4.

Particle Displacement and Velocities

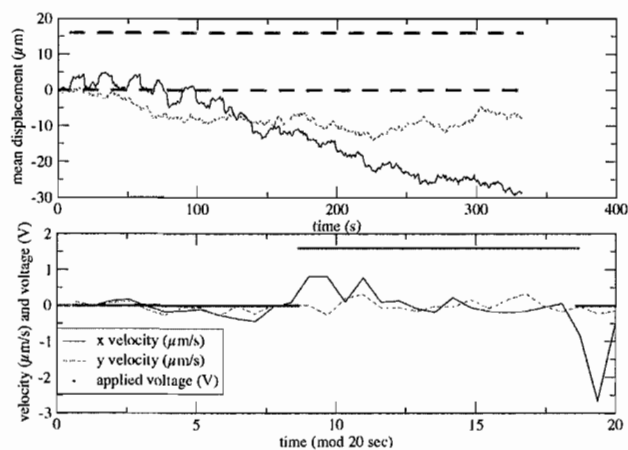
Response to the applied voltage was most often observed at voltages above $\sim 0.5V$. The y displacement in Fig. 5.3A indicates the range over which the mean displacement can vary for a small number of particles ($N \approx 10$ here). The inherent variability of mean displacement associated with $N \approx 10$ particles in A. is clearly exhibited in the y displacement of the same particles. The graph shows clear x -displacements in response to the applied voltage during the first 100 seconds or so, with x motion in synch with the applied voltage. Such displacement is less clear during the rest of the experiment and other data taken with only a slightly lower voltage show similar periods of clear response in the middle of a 350-second experiment. Fig. 5.3B shows data from a separate experiment under very similar conditions that exhibit qualitatively different behavior. Here, substantial drift in x - and y -directions is visible in the mean displacement. In addition to this, there is a small increase in velocity during t_{ON} . Such variability in mean displacement illustrates the need for averaging quantities over many temporal periods in order to extract a mean response

to the applied voltage for an entire data set. An example of this is the mean velocity over one temporal cycle plotted in Fig. 5.3A and B, averaged over 17 temporal cycles. This quantity gives an average response to the applied potential for these particular data sets. Together, A and B exhibit features seen in various combinations in much of the data:

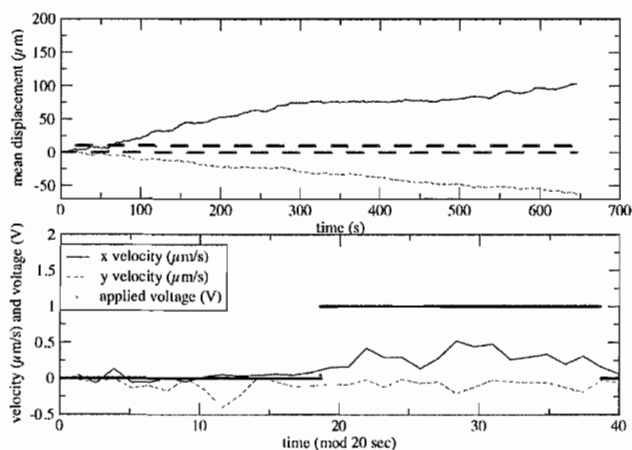
1. Relatively small x velocity when the potential is off, usually comparable to the noise seen in the y -velocity.
2. Clear spikes in x velocity in response to the switching the applied voltage on and off. These spikes vary in magnitude from the noise at about $0.1\mu\text{m}/\text{s}$ to $v_{\text{peak}} \approx 3\mu\text{m}/\text{s}$ and also vary in direction as discussed in Sec. 5.3.2.
3. An overall change in velocity when the potential is on.

In addition to the quantities discussed in Sec. 2.3 and plotted in Fig. 5.4 and 5.3, the transient response to voltage switching (peak $\langle v \rangle_t$) has been chosen to exhibit trends in how the particles respond to applied voltages under varying ionic strength and voltage. The peak $\langle v \rangle_t$ is the largest speed ($|\langle v \rangle_t|$) immediately after the potential is switched on and off. An example of the data is shown in Fig. 5.4. The peak mean velocity is convenient for quantifying the transient motion of particles in response to a switching potential.

The peak $\langle v \rangle_t$ of the particles after switching the potential on and off is shown graphed as a function of applied voltage in Fig. 5.5. Data collected at voltages below $V \approx 0.5V$ showed no peak velocities that were discernible from the noise. This data shows that the peak $\langle v \rangle_t$ is highly variable in sign and magnitude and that variability increases with applied voltage. The variability in magnitude in Fig. 5.3 is comparable in x and y directions, suggesting that each data point in Fig. 5.5 has an approximate error of $\pm 0.2\mu\text{m}/\text{s}$. However, the source of the observed variability in direction is less clear and will be discussed in Sec. 5.8.



A.



B.

FIGURE 5.3: Applied voltage, $\langle \Delta x \rangle_t$ (top) and time-averaged mean velocity over each experiment (bottom) for two experiments showing response to applied voltage. The direction of transport is x (perpendicular to the electrodes) while y is parallel to the electrodes and transverse to the microchannel. Data is for about 10 $0.2 \mu\text{m}$ -diameter, carboxylate-modified, fluorescent microspheres in 10^{-3} M NaCl solution.

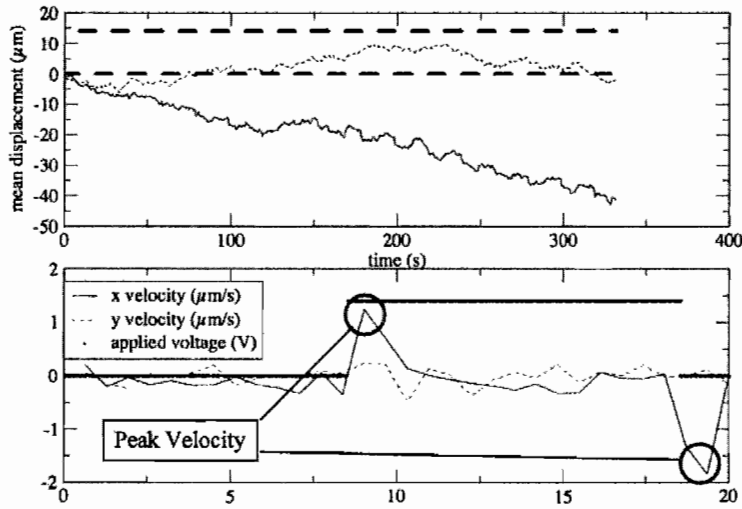


FIGURE 5.4: Applied voltage, mean x displacement and time-averaged mean velocity, $\langle \Delta x \rangle_t$. Peak mean velocities are circled.

Position Histograms

Particles at equilibrium in a periodic potential should exhibit a spatially periodic distribution. By calculating a histogram of observed particle positions modulo the spatial periodicity of the ratchet, an average distribution per period is obtained, giving a measure of the confinement of particles in the ratchet potential. In Fig. 5.6 A, the average distribution for a spatial period is plotted after the potential has been turned on and after it has been turned off.

Using basic Boltzmann statistics, the effective potential $\Phi_{effective}(x)$ can be calculated from the average spatial distribution $\rho(x)$. For each position x_i we have

$$\frac{n_i}{n_{total}} = e^{-\frac{\Phi(x_i)}{k_B T}}$$

and so

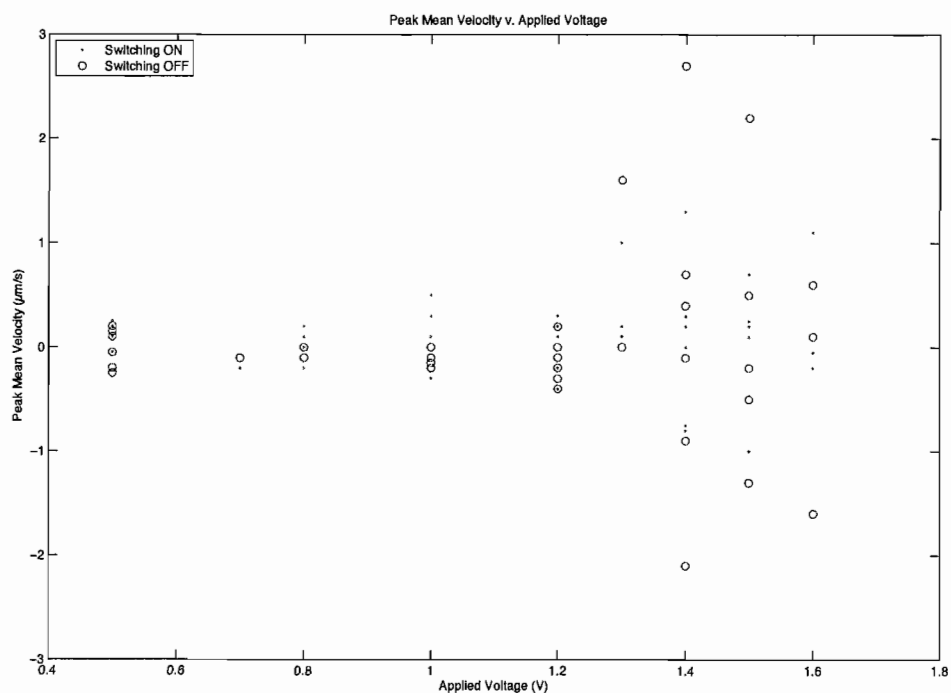


FIGURE 5.5: Peak $\langle v \rangle_t$ versus applied voltage. Variability in the peak $\langle v \rangle_t$ immediately after switching on and switching off increases for greater applied voltage. The magnitude and direction of peak velocities is variable at all voltages despite electrode arrays being in the same orientation for all experiments. These data were collected under the range of ionic strengths plotted in Fig. 5.7.

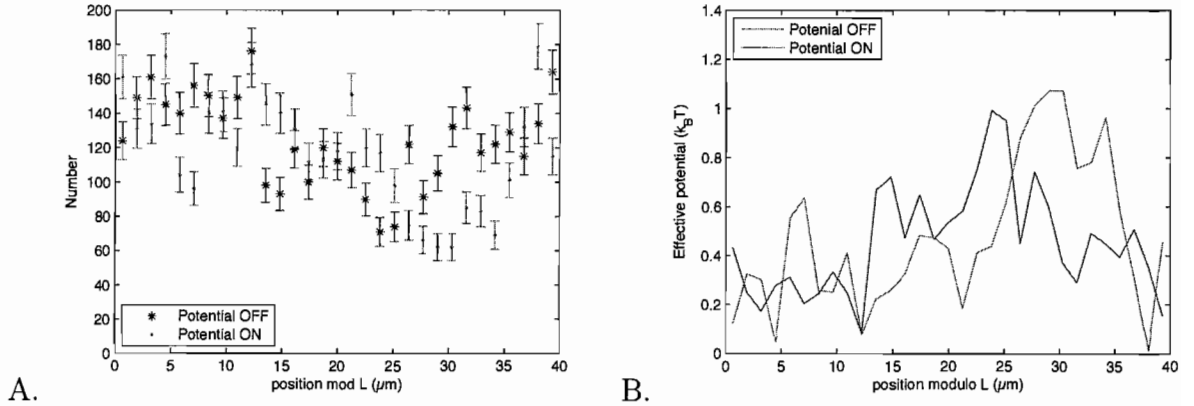


FIGURE 5.6: A. Particle position histograms during experiment shown in Fig. 5.3A. Error bars are for each data point. B. Effective potential calculated from the distribution in A.

$$\frac{\Phi(x_i)}{k_B T} = -\ln\left(\frac{n_i}{n_{total}}\right). \quad (5.2)$$

Fig. 5.6 B. shows the effective potential calculated from the histogram data using Eq. 5.2. There is some change between the ‘ON’ and ‘OFF’ data, but the largest possible potential depth from this data is $\Delta V \approx 1k_B T$.

Ionic Strength

In the particle ratchet system implemented here, the range of ionic strengths available for experimental investigation is limited above by nonspecific binding of the particles to the microchamber and below by the dissociation of water (see Sec. 4.2). The ionic strength characterizing these solutions for $[\text{Na Cl}] \approx 10^{-6} - 10^{-3} \text{ M}$ is the salt concentration, and the lower limit of ionic strength is set by the dissociation of water into its various ionic forms: completely pure water at room temperature has an ionic strength of $I \approx 10^{-7}$. One way that the experiments are affected by ionic strength is through nonspecific binding of particles to microchannel surfaces. Solutions with ionic strength above $I \approx 10^{-3} \text{ M}$ led to immediate immobilization of the particles on

the top and bottom surfaces of the microchannel as soon as the solution was drawn in by capillary flow. Salt concentrations with $I \approx 10^{-4}M$ often lasted about an hour before all the particles were immobile, while solutions with very low ionic strength ($I \approx 10^{-7}M$) could be observed for several hours without any nonspecific binding of the particles to microchannel surfaces. The effect of ionic strength on peak $\langle v \rangle_t$ can be seen in Fig. 5.7. Overall, wide variability in the observed response to applied voltage makes correlation with ionic strength difficult. The impact of this on analysis is discussed in Sec. 5.4.

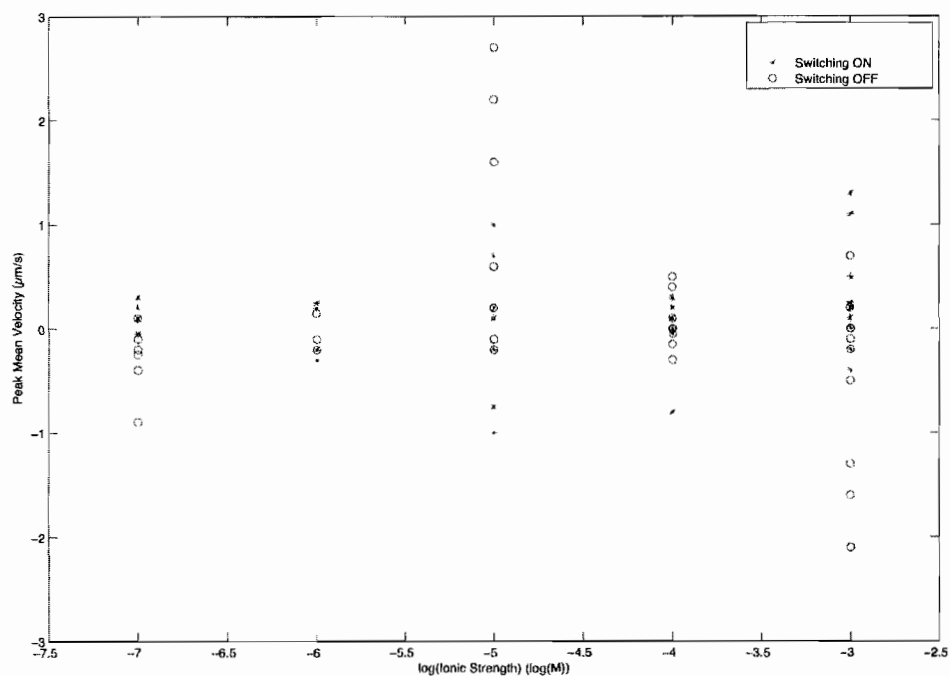


FIGURE 5.7: Peak mean velocities after switching on and off are plotted here versus ionic strength. Applied voltages cover the range shown in Fig. 5.5.

Discussion

With the experimental results in hand, qualitative and quantitative comparisons can be made between the predicted ratchet transport mechanism and experimental observations.

1. Overall mean transport velocity in the data shown here is $0.1 - 0.3 \mu\text{m}/\text{s}$.
2. There is often a transient velocity response when the applied voltage is switched on and off.
3. The transient response varies in direction and magnitude with little correlation to ionic strength or applied potential.
4. Some data show a relatively steady increased velocity while a voltage is applied.

As alluded to in Sec. 5.1, the data do not demonstrate ratchet transport of the type set out in Sec. 2.2. Within this subset of data, the total mean displacement of particles over a series of typically 10-20 voltage cycles was highly variable, with no consistent pattern relating overall transport to the strength of applied voltage, ionic strength of the solution or dimensions of the electrode array.

Signatures of Ratchet Transport

The results from the calculations in Sec. 2.2 can be applied using the conditions of the particle experiments to obtain an estimate for an expected ratchet velocity. Under ideal conditions (including good confinement of particles to the minima), Eq. 2.11 can be used, providing a very strong upper bound on the expected ratchet velocity. Ratchet asymmetry α can be estimated from the electrode array dimensions as

$$\alpha \approx \frac{2d_c}{L} = \begin{cases} 0.2 & L = 10d_c, \\ 0.15 & d_c = 3, L = 40. \end{cases} \quad (5.3)$$

where d_c , the critical dimension for lithography, is equal to the electrode width and the separation between electrode pairs. The array period L is the spatial repeat of the electrode array. When applied to an experiment with $t_{ON} = t_{OFF} = 20s$ and $L = 10d_c = 40\mu m$, (such as those shown in Fig. 5.3), Eq. 2.11 gives $v = 0.3\mu m/s$. Some of the observed data are near this predicted value, but as can be seen below, there are qualitative features of ratchet transport that are contradicted by the experimental observations. The treatment of the velocity above is independent of the details of the potential that drive confinement, but assumes that confinement is perfect and diffusion over the ratchet period L happens much faster than t_{OFF} . Without knowing exactly the potential experienced by the particles, it is difficult to make quantitative predictions about the average velocity of particles on timescales smaller than the temporal period of the ratchet. There are, however, a few clear qualitative signatures of flashing ratchet transport explained in Sec. 2.2.

- Mean particle velocity during t_{ON} is expected to decay to zero as the distribution equilibrates.
- Mean particle velocity during t_{OFF} is zero: diffusion is isotropic, unbounded in the region of interest and there is no net force on the particles.

Electrophoresis

Electrophoresis is the directed motion of charged objects in response to a DC electric field in a viscous medium. The intended electrostatic version of the flashing ratchet described here relies on electrophoresis as the mechanism for confining particles near the electrodes on one side of each pair in the interdigitated array shown in Fig. 1.1. The motion of particles under the conditions of the bead experiments is described by Eq. 2.2, and the relevant external force is just q , the charge of the particle, times the electric field along the direction of transport, E_x :

$$\dot{x} = \frac{qE_x}{\gamma} \quad (5.4)$$

For the sake of extracting an estimate of the maximum average velocity for particles during t_{ON} , assume that the applied force is constant. While this is only the case for piecewise-linear potentials, it allows a comparison between velocities expected in the short and long separations between electrodes.

A crude upper estimate for E_x is just the voltage drop between the electrodes divided by their separation, either αL or $(1 - \alpha)L$. Difficulties with this estimate are discussed in some detail in Sec. 5.5 and the inclusion of several additional effects will all serve to lower the estimate of E_x in nearly all of the device.

$$\dot{x} \approx \begin{cases} \frac{qV}{\alpha L \gamma} & \text{short slope,} \\ \frac{qV}{(1 - \alpha)L \gamma} & \text{long slope} \end{cases} \quad (5.5)$$

using the experimental parameters $\alpha L = 6\mu m$, $(1 - \alpha)L = 34\mu m$, $V = 1.4V$, here are some estimates of v.

charge q	$3.2 \times 10^{-14}C$
γ	$2 \times 10^{-9}kg/s$
$E_x(short)$	$2.3 \times 10^5V/m$
$E_x(long)$	$4.1 \times 10^4V/m$
\dot{x}_{short}	$3.7m/s$
\dot{x}_{long}	$6.4 \times 10^{-1}m/s$
Δt	$1.6 - 53\mu s$

These numbers are several orders of magnitude higher than observed velocities (high instantaneous velocities are typically less than $10\mu m/s$). The source of this discrepancy is the estimate for the electric field; corrections to this are discussed in Sec. 5.5. The electrophoretic velocities calculated above represent only the motion during t_{ON} , the confinement stage of the ratchet cycle. The calculation of ratchet velocity in Sec. 2.2 assumes that confinement happens in a time less than t_{ON} , so high electrophoretic velocities do not correspond to overall ratchet velocities exceeding

those calculated in Sec. 2.2. The observed transient velocities in response to switching ON may be related to electrophoretic forces, but those in response to switching OFF are not predicted by the flashing ratchet model. The inconsistencies between observations and the signatures of simple flashing ratchet transport will be discussed below along with other possible transport features of the system.

Screening and Electrostatic Potentials in Interdigitated Electrode Array Devices

It is tempting to think of a voltage applied across interdigitated electrode arrays to result in an electrostatic potential for charged particles in solution equal to the charge times the applied voltage. This would be approximately true for a simple dielectric, but the ions present in every aqueous solution are free to move and readily respond to applied fields. The screening in response to an electrostatic potential in solution has been described in some detail in Chapter IV and the relevant results are:

- The potential $\Phi(s)$ due to a line charge decreases with distance s :

$$\Phi(s) \propto \frac{1}{\sqrt{s}} e^{-\frac{s}{\lambda_{Debye}}}$$

for

$$s \gtrsim 10\lambda_{Debye} \tag{5.6}$$

- Closer than λ_{Debye} , Φ is larger than in the above limit, but decays faster.

For the dimensions of the electrode arrays used in particle experiments described here, counterion screening near the electrodes and the sub-micron Debye lengths in solution mean that the electrostatic potential in the bulk solution is likely very small. The ions in solution adjust their spatial distribution to oppose the field and reduce the potential energy of an ion in solution to approximately $k_B T$. However, the particles of interest have a much greater charge and a lower Debye frequency than the ions

that screen the electrodes. Also, counterions screening a particle in solution feel a force in the opposite direction of the particle itself and since they are free to move in the fluid, the particles are not effectively screened in solution. Screening of the electrodes, however, will leave a very small potential for ions in solution, as discussed in Sec. 4.4. The baseline potential for the Debye-Hückel screening to apply is about $0.25k_B T$:

$$eV \lesssim 0.25k_B T$$

but for the particles, with estimated charge

$$q \approx 10^5 e$$

$$qV \approx 10^4 k_B T \tag{5.7}$$

Screening of the electrodes results in an exponential decay of the potential with λ_{Debye} as the characteristic length. If particles with a greater charge are sensitive to very small electrostatic potentials, the relevant length scale will be more than just λ_{Debye} . In order to experience some kind of confinement, a potential of at least a few $k_B T$ is needed, and in order for *particles* to feel a $k_B T$ potential, the potential for an ion can be as low as $10^{-5} k_B T$.

$$10^{-5} k_B T \approx 0.25 k_B T e^{-\frac{x}{\lambda_{Debye}}}$$

The distance x at which a particle with charge

$$q = 10^5 e$$

feels a potential of around $k_B T$ is then

$$x \approx 10 \lambda_{Debye} \tag{5.8}$$

This indicates that experiments done at low salt concentrations (e.g. where $\lambda_{Debye} = 0.1 - 1 \mu m$) should see very good confinement near the electrodes and

confinement should be highly dependent on salt concentration. In fact, neither of these is the case. Position histograms in Fig. 5.6 from the same experiments shown in Fig. 5.7 show no clear sign of confinement and the dependence of peak $\langle v \rangle_t$ on ionic strength is indeterminate. So electrophoretic forces, while potentially relevant for highly-charged particles in solution, do not offer a complete explanation of the data. In order to develop a more nuanced picture of what happens to particles when voltages are applied across interdigitated electrode arrays, other effects such as electroosmosis must be considered.

Electroosmosis

Electroosmosis is fluid flow that arises from applying an electric field to layers of charged fluid near surfaces. The relevant source of surface charge here is the dissociation in water of silanol groups on oxidized silicon surfaces. This dissociation leaves a surface charge that is screened by counterions in solution and these counterions form a layer of charged fluid. As discussed in Sec. 4.4, the charge densities and electric fields can be described by the linearized Poisson-Boltzmann equation, which gives a (steeper than) exponential falloff of charge density into the fluid with the Debye length, λ_{Debye} as its characteristic length. A uniform field applied parallel to the charged surface will generate a stress in the charged portion of the fluid, leading to a velocity profile that starts at zero at the surface and increases to a slip velocity v_{slip} about a Debye length from the surface, as shown in Fig. 5.8. v_{slip} is determined by λ_{Debye} , σ_{glass} , η the viscosity of the medium and the strength of the applied field E [40].

$$v_{slip} = \frac{\lambda_{Debye} \sigma_{glass}}{\eta} E \quad (5.9)$$

This slip velocity is obtained by taking the velocity gradient caused by applying a uniform field to the non-uniform charge density of the Debye layer and integrating it from the surface to infinity. The glass surfaces of the microchannel are charged in solution due to dissociation of silanol (SiOH) bonds at the glass-water interface [41].

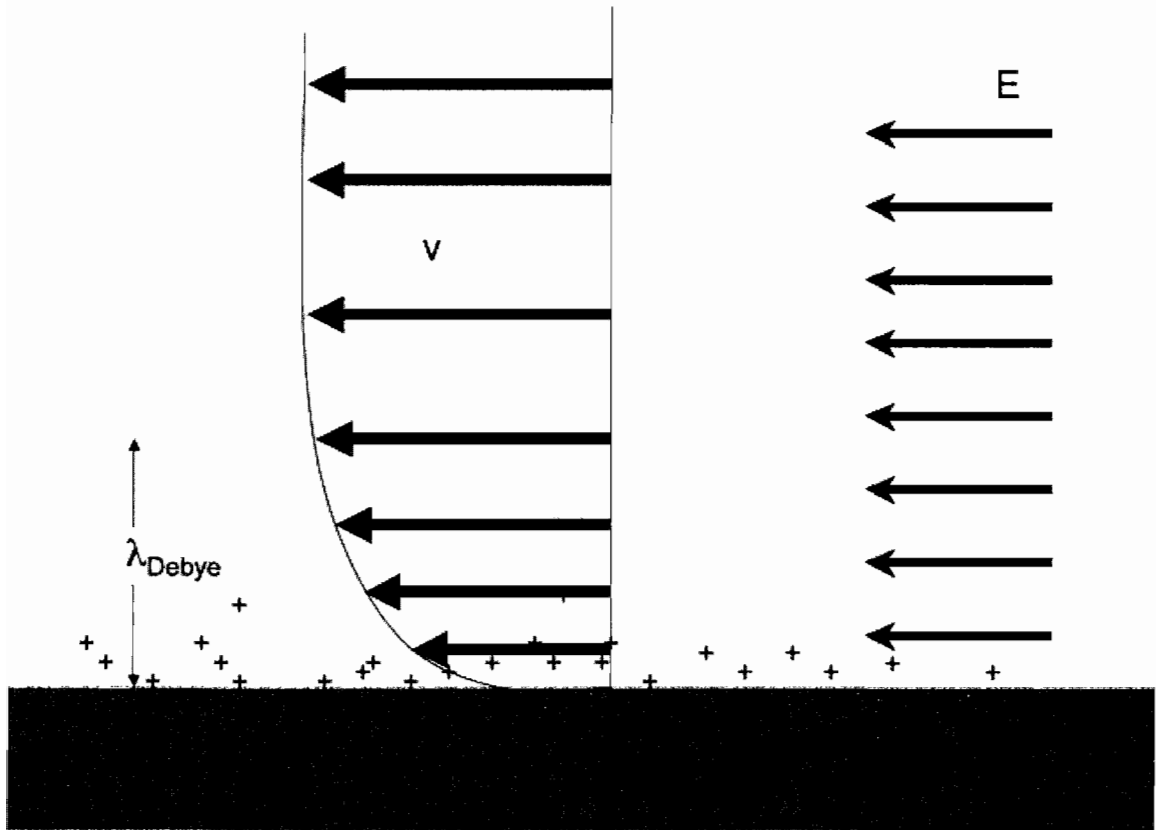


FIGURE 5.8: Electroosmotic flow at a charged surface driven by a uniform electric field E .

Qualitative features of electroosmosis

The details of electroosmotic fluid flow in interdigitated electrode systems are more complex than the simple case of uniform E field described above. One source of the complexity is that there are necessarily competing fluid flows: even in symmetrically

spaced arrays, the electric field along one section of the array is in the opposite direction of the field in adjacent sections. These fluid flows form circulating rolls with velocities that decrease with distance into the bulk, and the velocity decreases further from the surface with the spatial extent of the driving slip velocity as a characteristic length scale, as sketched in Fig. 5.9A. In the case of symmetric electrodes, these fluid flow structures give no net velocity, however, if the symmetry of the array is broken, an AC voltage applied across the array would generate a net fluid flow [42, 43]. There are several proposed methods to break this symmetry, including: making one electrode in each pair wider, altering the topography of the surface or allowing for current to flow through electrochemical reactions that are biased to one electrode in each pair. For experimental systems with asymmetric electrode sizes, pumping speeds are often on the order of mm/s for applied voltages of a few volts at frequencies usually in the kHz range [43, 44, 45, 46, 47, 40, 48]. It is unclear if simple asymmetric spacing of electrodes should necessarily break the symmetry that prevents fluid flow for AC voltages applied to symmetric arrays. It is also unclear how the fluid should respond to a DC voltage or what transient behavior can be expected. Some recent work from the field of AC electroosmotic pumping that is imminently relevant to the system studied here was published in 2006 [46]. In that paper, it is predicted that even in the limit of zero frequency with symmetric electrodes, asymmetric charge injection will generate a net fluid flux. Careful analysis of the impedance of electrode arrays has been helpful in investigating AC electroosmosis in electrode arrays [45]. Unfortunately, complete electrochemical characterization of the devices would be especially difficult in a sealed microfluidic environment because an electrochemical reference electrode such as a salt bridge would have to be coupled to the microchamber. The comparison to AC electroosmotic effects is also complicated by the nature of the flashing ratchet potential. The ratchet potential generates forces that, when integrated over all *space*, sum to zero. However, unlike the AC electroosmosis case, the *time averaged* force at any point is not zero. This alone

could provide a ratchet effect if a transient fluid flow induces net transport that is not completely reversed when the potential is turned off.

Despite these difficulties, it is instructive to sketch out a possible fluid flow that could be induced by electroosmosis in the interdigitated electrode arrays. It is worth recalling here that the counterions near silicon oxide surfaces are positive, meaning that in a uniform electric field the electrophoretic force on a negatively-charged particle or polymer would be in the opposite direction of the slip velocity at the surface. This does not necessarily mean that the two effects are in opposition in an interdigitated electrode array: electroosmotically-induced slip velocity at the surface can generate circulating flows in the bulk that are antiparallel to the electric field causing the slip velocity. In early analysis of electroosmotic pumping by periodic surface potentials, Ajdari included only counterion screening due to an applied surface voltage [42]. If this approach is applied to asymmetrically-spaced interdigitated electrode arrays, the resulting hydrodynamic boundary conditions regain $x \rightarrow -x$ symmetry because the charged fluid near each electrode opposes the charge of that electrode. A sketch of resulting fluid flow is shown in Fig. 5.9A. However, if the charged surface of the glass is taken into account, the resulting pattern of slip velocities retains the $x \rightarrow -x$ asymmetry of the charged electrode array (Fig. 5.9B).

One basic feature of electroosmotic flow is that if a field is maintained, it leads to steady fluid flow in the region outside the Debye layer. This is in contrast to the response of particles to a spatially periodic ratchet potential, where turning on the potential leads to a *displacement*, not a steady velocity. Of course this fluid flow in a viscous medium cannot go on forever without energy input. The geometry of electroosmotic flow driven by a uniform electric field parallel to the surface as shown in Fig. 5.8 precludes surface screening from decreasing flow velocity. This is problematic for the case at hand: without some kind of screening reducing the field or current flow into the electrodes, such a setup would drive fluid flow *ad infinitum* without requiring any power input. However, the field in an interdigitated electrode array is not always

parallel to the surface and the buildup of charge in the screening layer around the electrodes will reduce the transverse electric field and thus the fluid flow. The fluid patterns shown in Fig. 5.9 are then transient unless electrochemical reactions at the electrodes allow current to flow and sustain the fields in solution. The data in Fig. 5.3.B show a signature of likely charge injection at the electrodes: in this experiment, an overall increase in velocity is coincident with the applied voltage.

Another important factor in analyzing the role of electroosmotic flow in the devices is considering the impact of finite chamber height. Recently published theoretical analysis of AC electroosmotic pumping concluded that for AC electroosmosis, decreasing chamber height actually increased the maximum pumping speed and decreased the optimal AC frequency [49]. This would suggest that in devices where the microchannel height is much smaller than electrode array periodicity, (such as those used in the experiments described here), transient velocities could be greater than in devices with larger microfluidic channel heights.

Hydrodynamic and Electrodynamic Conditions

This surface charge density is largely set by the pH of the solution, which is always near 7 for the experiments discussed here [41]:

$$\sigma_{glass} \approx -5 \times 10^{-4} \text{ C/m}^2 \quad (5.10)$$

The solutions used in particle experiments ranged in ionic strength from 10^{-7} M to 10^{-3} M sodium chloride, giving a range of Debye lengths:

$$\lambda_{Debye} = \sqrt{\frac{\epsilon_0 \epsilon_{H_2O} k_B T}{N_A e^2 I}} \quad (5.11)$$

Ionic Strength (Molar)	Debye Length (μm)
10^{-7}	1
10^{-5}	0.1
10^{-4}	0.03
10^{-3}	0.01

For the conditions described above,

$$v_{slip} = \frac{\{1, 0.1, 0.03, 0.01\} \times 10^{-6} m \cdot 10^{-4} C/m}{10^{-3} Pa \cdot s}$$

$$= \frac{\{5 - 0.05\} \times 10^{-7} m^2}{V \cdot s} E \quad (5.12)$$

Using the crude field estimates described above, $v_{slip} = \{1 - 0.01\} \times 10^{-1} m/s$ for the short electrode separation (αL) and $v_{slip} = \{2 - 0.02\} \times 10^{-2} m/s$ for the long electrode separation, ($(1 - \alpha)L$). Again, the discrepancy here between observed peak $\langle v \rangle_t$ and predicted velocity is due in part to overestimating the electric field. See Sec. 5.5 for a discussion of this.

Transient Reversals

One unexplained aspect of the data shown in Fig. 5.3 is the rapid response to the potential switching off. The basic descriptions of electroosmosis and electrophoresis given above do not allow for any sort of reverse response when the potential is turned off. Therefore, the source of the external electric field and the screening process need to be considered over the entire voltage cycle. When a voltage is applied across the electrode array, counterions in solution move to screen the charges that accumulate in the electrodes. When the potential is switched off, the electrodes are linked together and charges equilibrate. This includes a reversal of the screening process. The charges on the electrodes (now electrically connected) decrease faster than the charges in solution diffuse away and the counterions themselves will form a temporary, oppositely-charged region of fluid near the electrodes. This residual charge inhomogeneity likely creates transient electroosmotic flow or electrophoretic drift, leading to the spike in mean particle velocities seen in the data.

Additional Observations

Inconsistent Transport Direction

One possible source of the inconsistent velocity direction seen in Fig. 5.7 is the variability in hydrodynamic boundary conditions at the ends of the microchannel. A bulk flow effect, such as a net electroosmotic flow due to charge injection, may be frustrated by complete sealing of the ends of the microchannel. A no-flow boundary hydrodynamic boundary condition eliminates the possibility of net flow in the channel and may result in reduced transport of particles. However, if one end of the microchannel offers a weak boundary (e.g. a flexible interface or a small constriction leading to air), the direction of bulk flow may be determined by this broken symmetry. The sealing method used (Appendix C) necessarily seals one end of the chamber first; this may mean that one end of the channel has different sealing characteristics than the other.

Thermophoresis

The data in Fig. 5.3B show simultaneous drift in the x - and y -direction. This and the occasional observation of slow, radial movement of particles in other experiments suggest that another effect could be at work. One possibility is that heating of the device (through absorption of the fluorescence excitation light) created local temperature gradients, causing thermophoresis of the particles. Thermophoresis is the motion of objects in solution along thermal gradients due to the temperature dependence of ionic shielding and the solvation of the particles. Detailed description of thermophoresis is beyond the scope of this work, but recently published work includes experimental conditions very similar to those of the data discussed above [50]. Among the results published are that for a $0.2\mu m$ diameter bead, a Soret coefficient $S_T = 0.5K^{-1}$ has been measured, corresponding to a thermodiffusion coefficient of

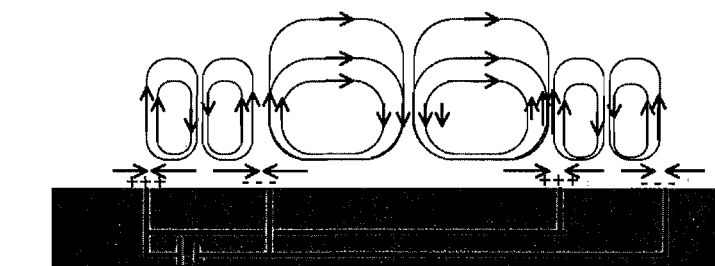
$$D_T = 1\mu m^2 s^{-1} K^{-1}.$$

$$v_{drift} = D_T \frac{\Delta T}{\Delta x} = 1\mu m^2 s^{-1} K^{-1} \frac{\Delta T}{\Delta x} \quad (5.13)$$

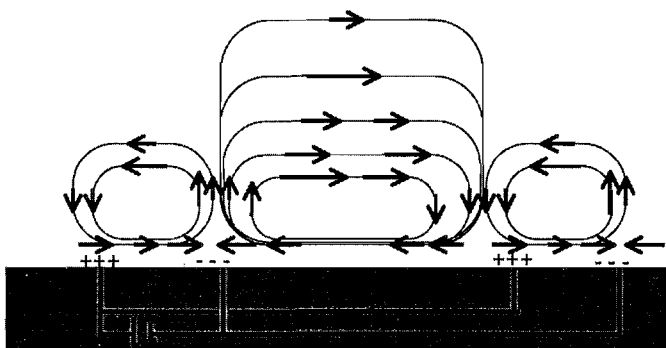
The drift of $v_{drift} \approx 0.1\mu m/s$ seen in the y -direction in Fig. 5.3B. corresponds to a temperature gradient of $0.1K/\mu m$.

Summary of Results from Particle Experiments

Particle tracking has revealed a wide range of responses to applied voltages in interdigitated electrode array devices. The motion of microspheres includes transient spikes in velocity in response to switching that vary in magnitude and direction. The electrophoretic forces that were planned to drive confinement in a flashing ratchet have not provided consistent measurable confinement. However, particles do move in response to switching voltage, indicating that other effects are at work. A likely source of particle movement is the motion of the fluid that surrounds them. Electroosmotic flow has been shown to drive fluid transport in related types of electrode arrays, although it is not discussed for DC voltages in the literature. A qualitative assessment of the flows induced by slip boundary conditions suggests that asymmetrically-spaced interdigitated electrode arrays can support transient directed bulk flow despite the spatial periodicity of the potential applied to the array.



A.



B.

FIGURE 5.9: Sketches of electroosmotically driven flows. Electroosmosis drives fluid flow within a Debye length of the surface, represented as a slip velocity here. The velocity falls off away from the surface with the size of the region driving the flow as a characteristic length scale. A. If screening of substrate charge is ignored, the slip boundary conditions at the surface and the resulting flows are symmetric. B. The presence of a positive screening layer across the surface induces an asymmetric slip velocity, thus preserving the asymmetry of the underlying applied potential.

CHAPTER VI

POLYMER EXPERIMENTS AND RESULTS

Introduction

Simulation work described in Sec. 3.1 predicted a novel mode of Brownian ratchet transport that utilized the internal degrees of freedom of a polymer to randomize the polymer configuration during the ‘off’ cycle of a flashing ratchet potential. Experiments described here were undertaken in order to observe the ratchet transport of polymers above an interdigitated electrode array. As mentioned in Chapter V, the results of particle ratchet experiments strongly suggest that micron-scale interdigitated electrode arrays do not effectively create ratchet potentials in solution. This did not, however, obviate the need for polymer ratchet experiments. The particle and polymer ratchet experiments took place in different experimental regimes, e.g. different microchamber heights, electrode array dimensions and Debye lengths. The correspondence between experimental conditions was not clear enough to predict all the behavior of a polymer confined in a microchannel above an interdigitated electrode array.

The data collected in polymer ratchet experiments includes high-resolution fluorescence images of individual λ DNA molecules and these images contain a wealth of conformational information about the molecules in addition to their center-of-mass trajectories. This chapter discusses the data and also describes the processes for extracting quantitative information from images of individual DNA molecules. Measured quantities such as the mean polymer density distribution are discussed, along with a detailed discussion of applying principal components analysis to images of

polymers. Principal components analysis is applied to images of individual molecules in microchannels above interdigitated electrode arrays, giving a measure of the conformations explored by the molecules when a flashing voltage is applied across the electrode array.

Background

Although it is only 2 nm wide, double-stranded DNA can be made visible through the use of intercalating fluorescent dyes. When these dye molecules bind between DNA base pairs (bp) (typically one dye molecule per 4-5 base pairs), their quantum efficiency increases 100-1000 fold [51]. This bright fluorescence of the dye-DNA complex allows single DNA molecules to be imaged in solution using epi-fluorescence microscopy, such as the system described in D. For large DNA, such as the 48kbp λ DNA used here, the constantly changing conformation of DNA can be observed in sequences of images collected as DNA is subjected to thermal forces, as seen in Fig. 6.1.

Theoretical descriptions of polymer conformations and dynamics generally begin with the polymer as a set of ordered locations in space [34, 52]. An abundance of theoretical work on polymers focuses on using this set of locations to calculate the scaling of various quantities (e.g radius of gyration, diffusion coefficient, electrophoretic mobility) with the number of monomers, N , the persistence length l_p or related microscopic parameters. Such work relies on knowing each segment's location along the polymer contour, not just its location in space. There is considerably less work detailing the spatial distributions of polymers observable in series of two-dimensional images of a polymer. Two-dimensional images are, at best, a projection of the polymer into a single (x, y) plane, in which case z position information is simply lost. More likely, light is defocused from parts of the polymer making large excursions in the z -direction, and so (x, y) information is less precise for

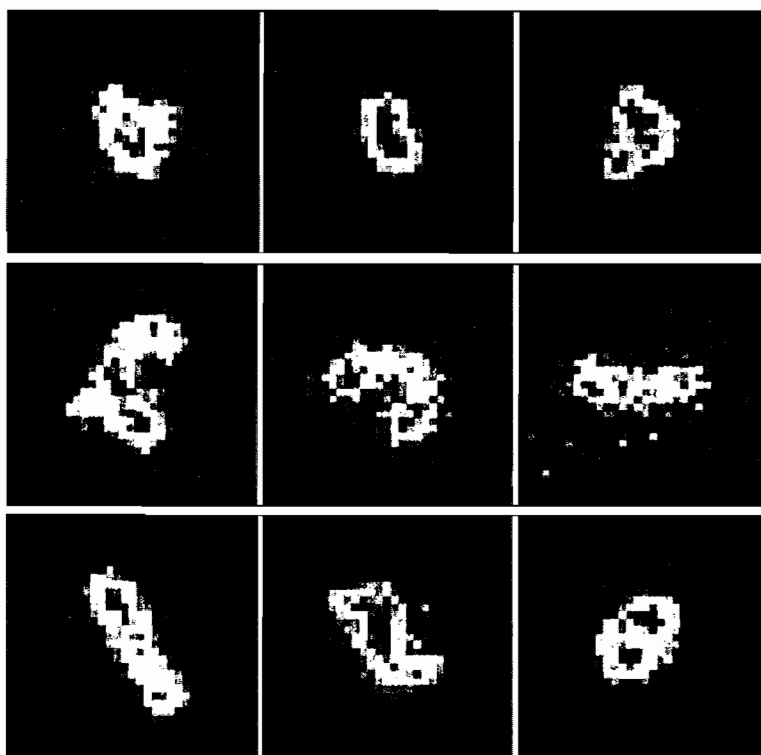


FIGURE 6.1: False color images of λ DNA molecules in a microchannel above an interdigitated electrode array. Each image is about $5 \mu m$ across and was collected over an exposure time of 50 ms.

that part of the polymer. So even with perfect resolution, a two-dimensional image of a polymer lacks the information needed to unambiguously reconstruct its three-dimensional structure. In the case of imaging polymers using fluorescence microscopy, the two-dimensional projection of the three-dimensional polymer configuration is also convolved with the optical point spread function, contaminated by additive noise from the CCD camera and essentially integrated over the exposure time.

Quantitatively describing the dynamics of polymer conformations is another analytical challenge. One theoretical method of describing the motion of polymers is the Rouse model, wherein the polymer is treated as a series of masses connected by spring-like potentials. This treatment leads to the decomposition of a polymer's motion into dynamical modes analogous to the vibrational modes of a string, called Rouse modes [34]. However, this requires knowledge of the entire chain as a sequence of positions and as mentioned above, this information is lost in two-dimensional images of DNA. One alternative method to quantify the conformational dynamics documented in images of DNA is the use of principal components analysis (PCA). PCA, which is discussed below in Sec. 6.6, can extract normal modes of the polymer's conformational variation as measured from images of DNA molecules.

Experiment Design and Description

Interdigitated Electrode Array Devices

Dimensions of the interdigitated electrode arrays for polymer experiments were set by the polymer ratchet simulations described in Chapter III and are indicated in the device sketch in Fig. 6.2. In order for λ DNA to sample several electrode array periods, the array period L was chosen to be a fraction of the radius of gyration $R_G \approx 0.7\mu m$. With $L = 500nm$ and the electrode width and spacing set at $cd = 50nm$ by the critical dimension of the electron beam lithography processes, the asymmetry

of the array is comparable to that used in particle experiments. Note that x - and y -axis conventions here differ from those used in Chapter V.

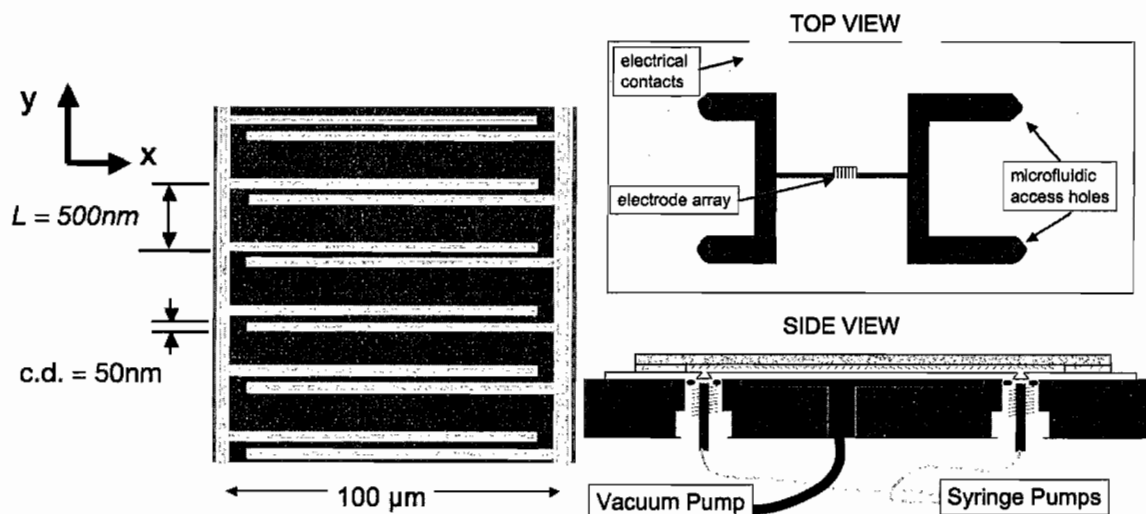


FIGURE 6.2: Left: Sketch of interdigitated electrode array used for polymer experiments. Right: Top view of device showing ‘H’ shaped microchannel design and electrical contact pads. Side view of device with chuck for microfluidic connections and vacuum seal.

The devices used in the polymer experiments were designed to be used more than once, because the sealing procedures were inconsistent and the electron-beam lithography steps time consuming. So in an effort to provide controlled microfluidic access to the microchannels above the interdigitated electrode array, an H-shaped layout was used, as shown in Fig. 6.2. The H layout consists of two long microchannels with a relatively large cross-section connected by a perpendicular microchannel of smaller cross-section. The ends of the larger microchannels are coupled through holes in the chip or coverslip to fluid reservoirs (syringe pumps in this case). Such layouts have been used successfully in similar experiments, for example, to observe the behavior of single DNA molecules in nanochannels [53, 54]. The advantage of such a layout is that solutions can be exchanged relatively rapidly in the large cross-section portions of the channel and flow can be actuated between any two access holes

by applying a pressure differential across them. To minimize the drop in pressure at the access holes, narrow (150 μm diameter) capillary tubing was used to connect syringe pumps to fittings on the chuck at the back of the chip. The chip was held in place on a custom-machined chuck by vacuum grooves and rubber-gasketed, threaded microfluidic fittings sealed capillary tubes to the holes in the chip with minimal dead volume. DNA and buffer solutions (described in App. B.1) were brought through capillary tubing from precision microliter syringes in two syringe pumps.

Experiment Protocol

Sealed devices were aligned to microfluidic fittings and secured on the chuck. Electrical contacts and microfluidic connections were made to the device and it was placed in the inverted fluorescence microscope described in Appendix D. A solution of λ DNA was pumped into the microchannel; detailed description of the DNA solution is described in Appendix B.1. The microscope objective was then focused on the microchannel and images were collected as various voltages were applied across the electrode array. Unfortunately, in many experiments there was leakage at the seal between the capillary tubing and the hole through back of the chip or at the capillary-syringe interface. These leakages or any incomplete seal of the coverslip to the microchannel led to undesired background fluid flow in the microchannel. This was combatted, with occasional success, by controlling fluid input into the system through the syringe pumps. The flow through the small microchannel itself displayed transient responses to changes in the syringe pumping rate; the characteristic time for these responses was estimated to range between 10 seconds and 2 minutes. The impact of this on the data collected can be seen in Fig. 6.4 where variable, background drifts affect measured particle velocities.

Analysis

All quantities measured in the particle experiments stem from particle trajectories only; the images of polymers collected here also include rich conformational information. This can be seen in the image taken from a polymer experiment shown in Fig. 6.1. The high magnification and numerical aperture of the microscope objective, combined with the high sensitivity of CCD camera allow great detail of the fluorescently labeled DNA molecules to be seen. The dynamics of DNA molecules described below is only possible through the high quality of these images. The level of detail also presents a challenge: how does one extract a (relatively) small amount of meaningful quantitative information from so much data? Fortunately, the polymer conformations can be quantified with a relatively small number of parameters through the use of principal components analysis, described in Sec. 6.6.

Observations in Polymer Experiments

Brownian Motion

Thermal motion in solution drives center-of-mass diffusion of a polymer, in addition to causing the constantly changing conformation observed in Fig. 6.1. The diffusion of λ DNA in the microchannel was measured from DNA trajectories using the methods described in Sec. 2.3.1, giving $D_\lambda = 0.16 \pm 0.01 \mu m^2/s$. The measured values of D for different values of Δt are plotted in Fig. 6.3. These values are considerably less than the reported value for D of λ DNA in bulk solution ($D_{bulk} = 0.46 \mu^2/s$), but are in agreement with published values of D for λ DNA in a slit with height 280 nm [55].

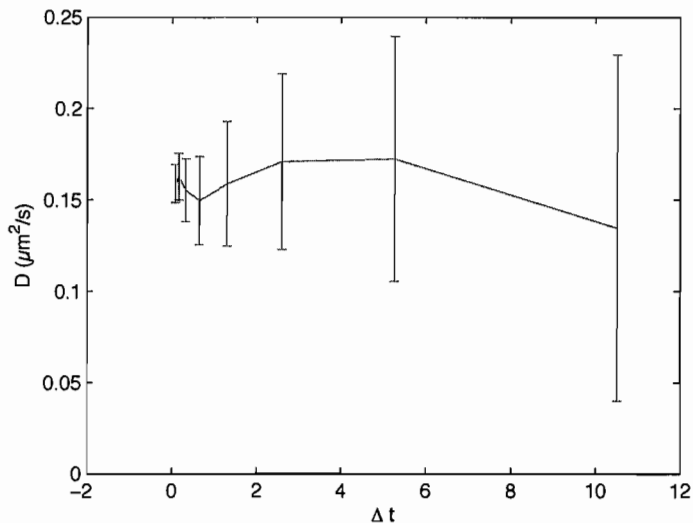


FIGURE 6.3: Measured diffusion coefficient D for λ DNA plotted *vs.* Δt in seconds. The error bars are the statistical error associated with calculating D from finite trajectories, as discussed in Sec. 2.3.1.

Polymer Motion in Response to Applied Potential

Trajectory analysis for polymer experiments starts with the image analysis steps described in Appendix A. The outputs of the image analysis are trajectories of each DNA molecule's center of mass. Relevant quantities for the analysis of polymer motion in response to the applied potential include the mean displacement and the mean velocity as a function of time.

Examples of mean polymer displacement data are shown in Fig. 6.4. In this particular experiment, no potential was applied for about the first 500 frames, providing an approximate baseline for background drift velocity. The mean DNA velocity from the same time series is shown in Fig. 6.5. It's clear from these data that there is a systematic response to the applied potential: DNA moves when voltage is applied and a net transport (here in the negative y -direction) is observed. These points would favor the polymer ratchet described in Chapter III as a mechanism for the observed transport. However, the data also show clear motion in response to

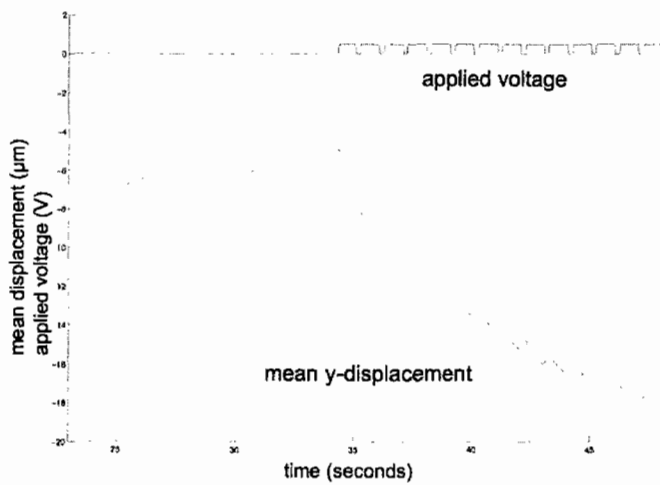


FIGURE 6.4: Mean DNA y -displacement *vs.* time before and during application of a flashing potential. DNA molecules move in the negative y -direction when the potential is on and reverse direction when the potential is turned off.

switching off the potential (something not predicted in the basic flashing ratchet) and the quantitative comparisons of velocities shown below do not confirm the polymer ratchet mechanism.

As in the particle experiments, it is helpful to average the displacement and velocity over several temporal periods of the applied potential. The results of this process are shown in Fig. 6.7 and 6.6.

The plots of mean displacement and velocity in response to the potential cycle shown in Fig. 6.7 and 6.6 provide an excellent format for comparing the observed DNA trajectories with the predictions of the polymer ratchet model. On average, there is a displacement in the positive y direction during t_{OFF} and a larger, negative displacement during t_{ON} . The displacement during t_{ON} takes place over the entire time the potential is applied. The velocity data show that during t_{ON} , there is a transient negative spike in velocity that decays relatively slowly, but never reaches zero. Qualitatively, this would be consistent with a ratchet mechanism with a prematurely stopped localization step. However, the displacement data establishes

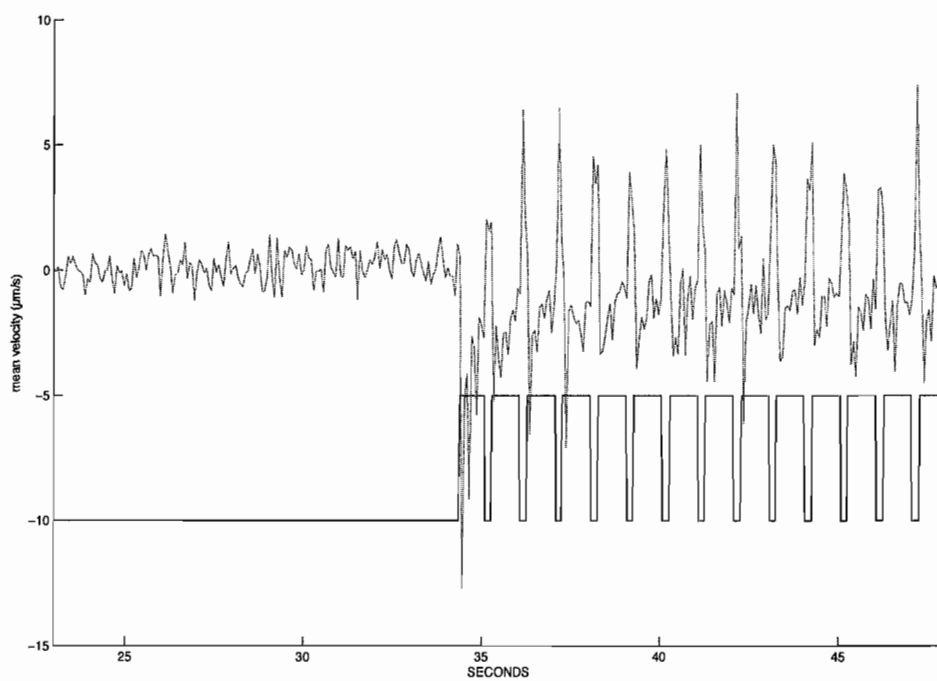


FIGURE 6.5: Mean DNA y displacement *vs.* time during the same time period shown in Fig. 6.5.

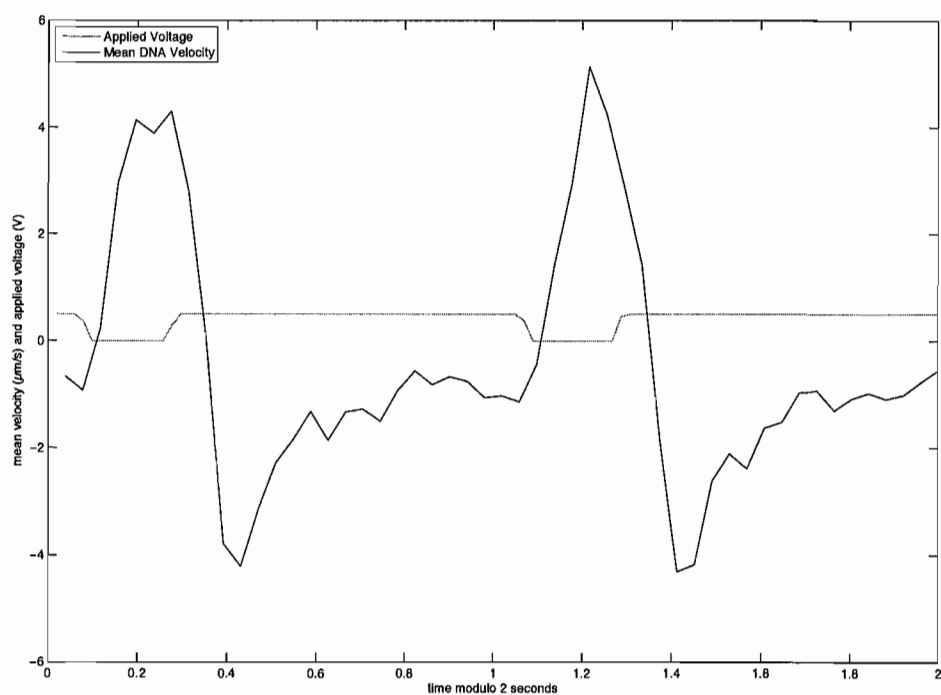


FIGURE 6.6: Mean DNA y velocity *vs.* time modulo two temporal periods of the flashing potential. For reference, the applied voltage is also plotted.

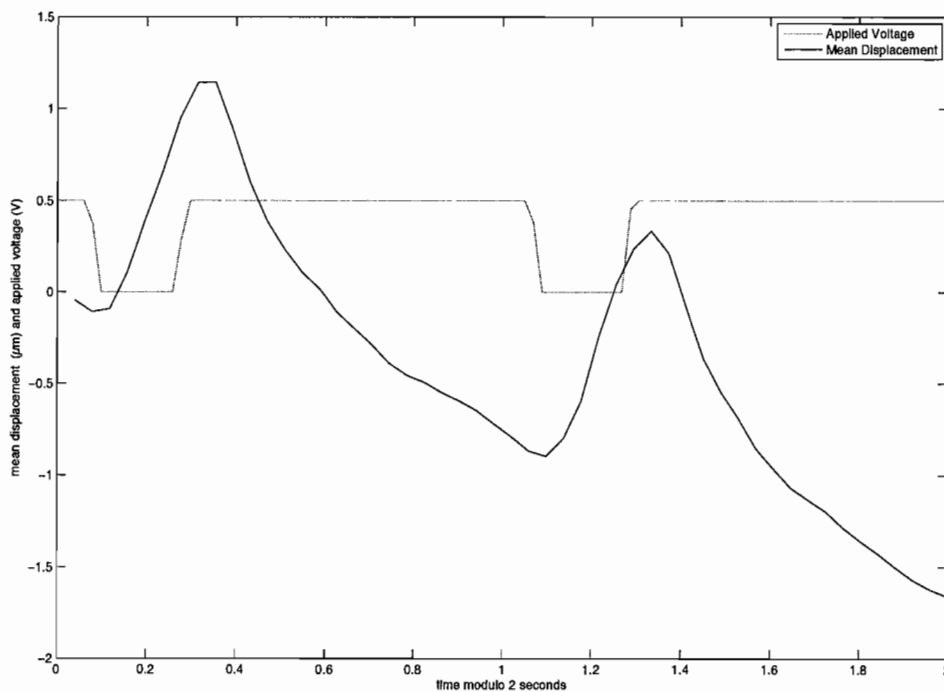


FIGURE 6.7: Mean DNA y displacement *vs.* time modulo two temporal periods of the flashing potential. This graph is derived only from time when the flashing potential was applied. The initial position at $t = 0$ is arbitrary, since this is averaged over many cycles of the applied voltage.

quantitative proof that the ratchet mechanism is not responsible for this velocity behavior: In the polymer ratchet model and the particle ratchet model, displacement of the during t_{ON} is necessarily less than the long slope of the applied potential. In the DNA experiments, the long distance between electrodes is $0.35\mu m$, so the mean displacement of a polymer ratchet during t_{ON} would have to be less than $0.35\mu m$. Here it is measured to be about $2\mu m$! This discrepancy means that whatever force is driving the motion seen in these data, it is not limited to moving DNA less than a single spatial period of the interdigitated electrode array. One phenomenon that could be responsible for this discrepancy is electroosmotically driven flow, which is discussed at length in Sec. 5.6. As long as there is a transverse electric field at the surface of the microchannel, electroosmosis will generate bulk flow above that surface. Any net bulk flow velocity response is a clear qualitative distinction from ratchet mechanisms that involve localization in a periodic potential. A qualitative feature of the velocity data that is unexplained by the basic ratchet mechanism is the response to switching off the potential. As discussed in Sec. 2.2, when a ratchet potential is turned off, diffusion will not cause systematic motion of the center of mass of the distribution. Any electric field driving an electroosmotic flow will eventually be screened by counterions in solution and the presence of a reverse velocity response to switching off the potential suggests that counterions involved in screening could generate fields to drive electroosmotic flow once the electrodes have been grounded. These features are different from the proposed ratchet mechanism, but correspond qualitatively to the observations in particle ratchet experiments (Chapter V), despite the 6-8 times smaller electrode array dimensions in the DNA experiments.

These qualitative and quantitative differences between the experimental data and the ratchet mechanism discussed in Chapter III clearly show that the motion of DNA in response to a potential applied across an interdigitated electrode array is not due to a Brownian ratchet.

Mean Polymer Conformation

The trajectory analysis discussed above conclusively shows that the observed DNA motion does not arise from a polymer ratchet mechanism. However, this does not eliminate the possibility that λ DNA undergoes conformational changes in response to the action of the interdigitated electrode array. This section addresses the experimental measurement of polymer conformations. The mean fluorescence intensity collected from λ DNA in the microchannels above interdigitated electrode arrays (shown in Fig. 6.8) is an important baseline for conformational analysis. The mean radial density distribution can be obtained by averaging the entire fluorescence intensity distribution for all λ DNA molecules over many frames. To calculate the mean intensity distribution, the center of mass of each polymer image is found during the particle tracking analysis described in Appendix A. Subsequently, a $5\mu\text{m} \times 5\mu\text{m}$ region of interest (ROI) around the center of mass location is selected for each polymer. The fluorescence intensities in each pixel of these ROIs are then averaged, forming a mean intensity distribution of the polymer. A cross-section of the mean intensity through the center of the distribution then gives a measurement of the radial distribution of the fluorescence intensity, and thus, the density of DNA. Quantities such as the second and fourth moments of the intensity distribution can be measured in every frame, but the wide variation in conformations of the DNA from frame to frame introduce fluctuations in these quantities that make analysis difficult. In many experimental images, the DNA molecule's polymer nature is clearly visible, but upon averaging, the overall shape of the DNA intensity superficially resembles a Gaussian distribution. However, if the DNA molecule were a snapshot of a random walk (which is a good approximation for a non-interacting polymer), the resulting mean intensity distribution would not be Gaussian because of how the averaging is taken (discussed below). If the DNA molecule is treated as a Gaussian coil (i.e. its segments form a random walk) and its center of mass is fixed at the origin, the mean spatial distribution about the center of mass corresponds to the ensemble average of

a sum of random walks with their centers of mass at the origin. The form of this distribution is given by $\phi(x)$:

$$\phi(x) = \frac{3}{2\pi R^2} \int_0^1 \frac{\exp(-3r^2/[2R^2(3\epsilon^2 - 3\epsilon + 1)])}{(3\epsilon^2 - 3\epsilon + 1)} d\epsilon \quad (6.1)$$

where x is the distance from the center of mass and R^2 is the mean square end-to-end distance. This form of the distribution was from [56] and originates in [57]. In the usual analysis of a random walk, one end of each random walk is fixed at the origin and the resulting mean spatial distribution is Gaussian. However, $\phi(x)$ falls off more slowly than a Gaussian because the center of mass of each distribution is placed at the origin. This means the ends of a random walk (where spatial fluctuations are the greatest), can be distributed away from the origin. In [56], Cohen and Moerner found that the average fluorescence intensity of λ DNA was fit well by this function in a microchamber with $h \approx 1\mu m$. Mean density distribution measurements made on λ DNA in interdigitated electrode array devices are shown and discussed below.

The measured intensity distribution is calculated from images collected before any voltages are applied and has been normalized so the maximum intensity is 1 and the minimum intensity is 0. Also shown in the figure are theoretical fits to the data: $\phi(x)$ has been fit to the data with end-to-end distance $R^2 = 2.68\mu m$ and a Gaussian with width $\sigma = 0.58\mu m$. The measured intensity *vs.* distance curve falls off more slowly than the Gaussian and is better fit by $\phi(x)$, the mean density of an ensemble of random walks whose centers of mass are located at the origin. These data clearly fit better to $\phi(x)$ than to the Gaussian, but not as well as previously reported data in [56], which falls off closer to $\phi(x)$. One likely source of this discrepancy is the high degree of confinement of λ DNA in a $.26\mu m$ -deep channel, which does not allow the polymer to relax to its bulk conformation [52, 55]. The slower fall-off of this intensity data could be affected by additive noise from the CCD camera, which is likely different in these data *vs.* those in [56], is more pronounced in the tails of the distribution and is not considered in $\phi(x)$.

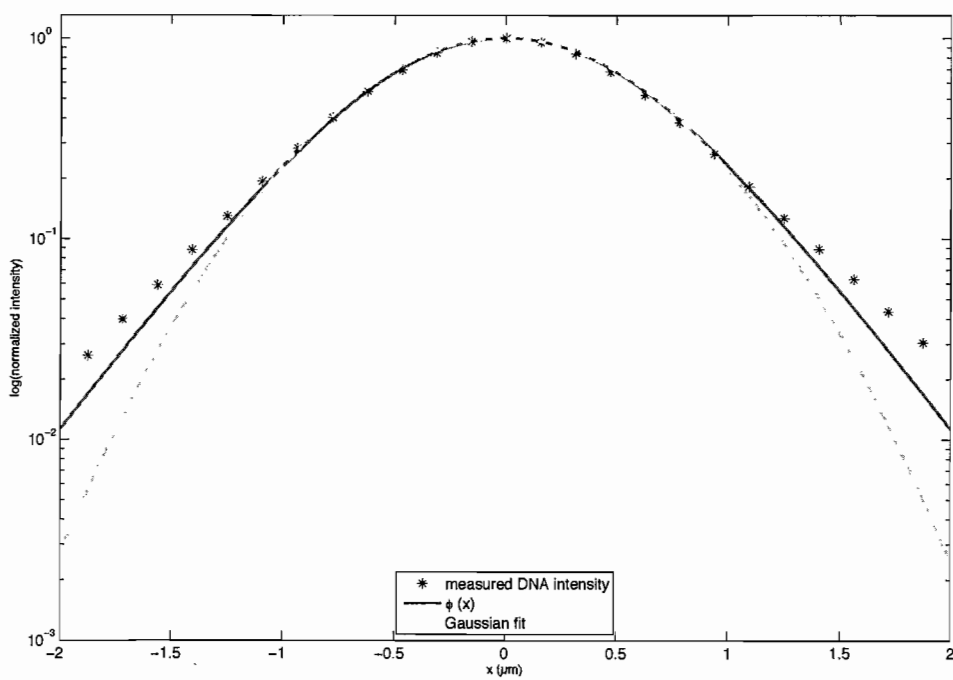


FIGURE 6.8: Mean DNA intensity with no voltage applied. $\phi(x)$ and the Gaussian fits are described in the text. Mean DNA intensity falls off more slowly than the Gaussian, but also slightly more slowly than $\phi(x)$.

Principal Components Analysis

Principal Components Analysis (PCA) is a method for extracting uncorrelated modes from correlated random variables [58]. As described below in Sec. 6.6.2, this method can be applied to sequences of fluorescence images of polymers to quantify the many conformations observed. PCA transforms the images in a large data set into a basis that efficiently expresses the sources of variance within the data. As a general method, PCA is a powerful technique to reduce data sets with large numbers of different, correlated measurements into amplitudes of a smaller number of uncorrelated modes that contain most of the variation in the data. These modes are not imposed on the data by an external model, but are extracted from the data itself, something that is particularly helpful in the absence of a predictive model or in a case where only empirical relations between different measurements are needed.

Introduction to Principal Components Analysis

Principal components are the eigenvectors of the covariance matrix made from a set of data. Mathematically, this is expressed in [58] as follows: start with a vector \mathbf{X} of p variables, each entry \vec{x}_p' containing n occasions of measuring that variable. For example, when the data are a set of n images, \vec{x}_p' contains all n values recorded for the p^{th} pixel. Since PCA deals with the variance of these variables, first subtract the mean of each entry from that row:

$$\mathbf{X}_C = \begin{bmatrix} \vec{x}_1' \\ \vec{x}_2' \\ \vec{x}_3' \\ \dots \\ \vec{x}_p' \end{bmatrix} - \begin{bmatrix} \langle \vec{x}_1' \rangle \\ \langle \vec{x}_2' \rangle \\ \langle \vec{x}_3' \rangle \\ \langle \vec{x}_{\dots}' \rangle \\ \langle \vec{x}_p' \rangle \end{bmatrix} \quad (6.2)$$

The covariance matrix \mathbf{C} is then calculated from \mathbf{X}_C . The covariance matrix \mathbf{C} is

the mean of the outer product \mathbf{X}_C and its transpose:

$$\mathbf{C} = \langle \mathbf{X}_C \mathbf{X}'_C \rangle_n \quad (6.3)$$

where $'$ denotes transpose and the averaging indicated by $\langle \rangle_n$ is over the n measurements. (In order to do this, it's clear that the second moment of x_i must exist for all rows of \mathbf{X} .) Solving the eigenvalue problem on the $p \times p$ covariance matrix \mathbf{C} gives a new matrix \mathbf{B} and a diagonal matrix of eigenvalues, λ . \mathbf{B} has columns, B_i , which, when ordered by descending eigenvalue and normalized so that $\mathbf{B}'_i \mathbf{B}_i = 1$, are the principal components of the data \mathbf{X}_C . It's worth noting that the diagonal elements of \mathbf{C} are just σ_p^2 , the variance of each of the p measured quantities. For image analysis, σ_p^2 is the variance of the p^{th} pixel. The connection between the eigenvalue matrix and the covariance matrix is important:

$$\sum_{i=1}^p \sigma_i^2 = \text{tr } \mathbf{C} = \text{tr}(\mathbf{C} \mathbf{B} \mathbf{B}')$$

since $\mathbf{B} \mathbf{B}' = \mathbf{I}$, (where \mathbf{I} is the $p \times p$ identity matrix).

$$= \text{tr}(\mathbf{B}' \mathbf{C} \mathbf{B}) = \text{tr } \lambda$$

so

$$\sum_{i=1}^p \sigma_i^2 = \text{tr } \lambda = \sum_{i=1}^p \lambda_i \quad (6.4)$$

So each eigenvalue λ_i is proportional to the fraction of the total variance of \mathbf{X}_C associated with the principal component \mathbf{B}_i .

Each data point X is comprised of one measurement of each of the p variables (in image analysis, X is a single image), and X can now be decomposed into a sum of principal components,

$$X = a_1 \mathbf{B}_1 + a_2 \mathbf{B}_2 + a_3 \mathbf{B}_3 + \dots + a_p \mathbf{B}_p \quad (6.5)$$

and since \mathbf{B} is ordered by decreasing λ , more of the variance is contained in the first component than in the second, and so on. This reveals an important feature of

PCA: by transforming the data in \mathbf{X}_C into the basis of principal components, most of the features associated with the variance in the data can be expressed in terms of just a few numbers, the coefficients of the first few principal components, a_i . This analysis has assumed that each eigenvalue λ has been unique. Mathematical methods for dealing with multiple roots are discussed at length in [58], and in practice, some modes may not be statistically distinct. In fact, principal components with similar eigenvalues in [56] were ‘mixed together’ and had to be adjusted by hand to obtain principal components with more visible symmetries. This procedure was not necessary on the data discussed here.

In summary, this is a method to express data from measurements of many correlated quantities in an orthonormal basis of principal components. Because most of the variance of the data arises from the first few principal components, the coefficients of the first few principal components capture most of a data point X ’s contribution to the variance. In other words, the first few principal components are an efficient way to express how a data point X is different from the average.

Application to Polymer Images

In the case of image analysis, PCA allows salient visual features that differentiate a particular image from others in a large set of similar images to be expressed in a few numbers. This leads to substantial data reduction and to quantification of statistically significant image features. For images, each of n data points in \mathbf{X} is just the values of the p pixels of the n^{th} image. These p quantities are clearly correlated in any kind of image sequence, but PCA transforms \mathbf{X} into a basis where the components are uncorrelated. By subtracting the mean from the data, information about the average image is removed and \mathbf{X} is expressed in a basis that efficiently identifies the sources of variance amongst images.

PCA was first applied to images of polymers by Cohen and Moerner [59] in 2007. PCA is an especially attractive tool for analysis of polymer conformations

from images because it does not rely on an external model to predict the variations in images. Instead, PCA extracts the normal modes of polymer intensity distributions and allows the conformations of a polymer seen in the images to be described with only a few parameters. The principal components themselves are an interesting source of information about the polymer density. Fig. 6.9 shows an example of PCA applied to images taken of λ DNA in a microchannel above an interdigitated electrode array before any potential is applied. The first 16 principal components are ordered left to right and top to bottom by eigenvalue. These principal components agree qualitatively with those published in [59] and the results from experiments will be discussed in detail in Sec. 6.7.

Each eigenvalue is proportional to the fraction of the variance associated with that principal component. Since the principal components are normal modes of the system, they can be treated as separate degrees of freedom. The variance σ_i^2 associated with the i^{th} principal component then provides the stiffness, k_i of that mode:

$$\frac{k_i \sigma_i^2}{2} = \frac{k_B T}{2} \quad (6.6)$$

The principal components shown in Fig. 6.9 of the DNA as recorded by fluorescence microscopy are visually similar to vibrational modes of an elastic medium, with shorter wavelength modes having a higher stiffness. The underlying physics of the modes and the associated spectra are not completely understood, although treating the polymer as a random walk has been reported to yield similar normal modes [56]. In Sec. 6.7, principal components are used to quantify the conformations explored by λ DNA molecules in response to voltages applied across interdigitated electrode arrays.

The computation of principal components from λ DNA image data was done using built-in functions in Matlab. Additional programming was done to decompose other images (see Sec. 6.6.3 and 6.7) into equilibrium principal components and analyze the resulting principal component amplitudes.

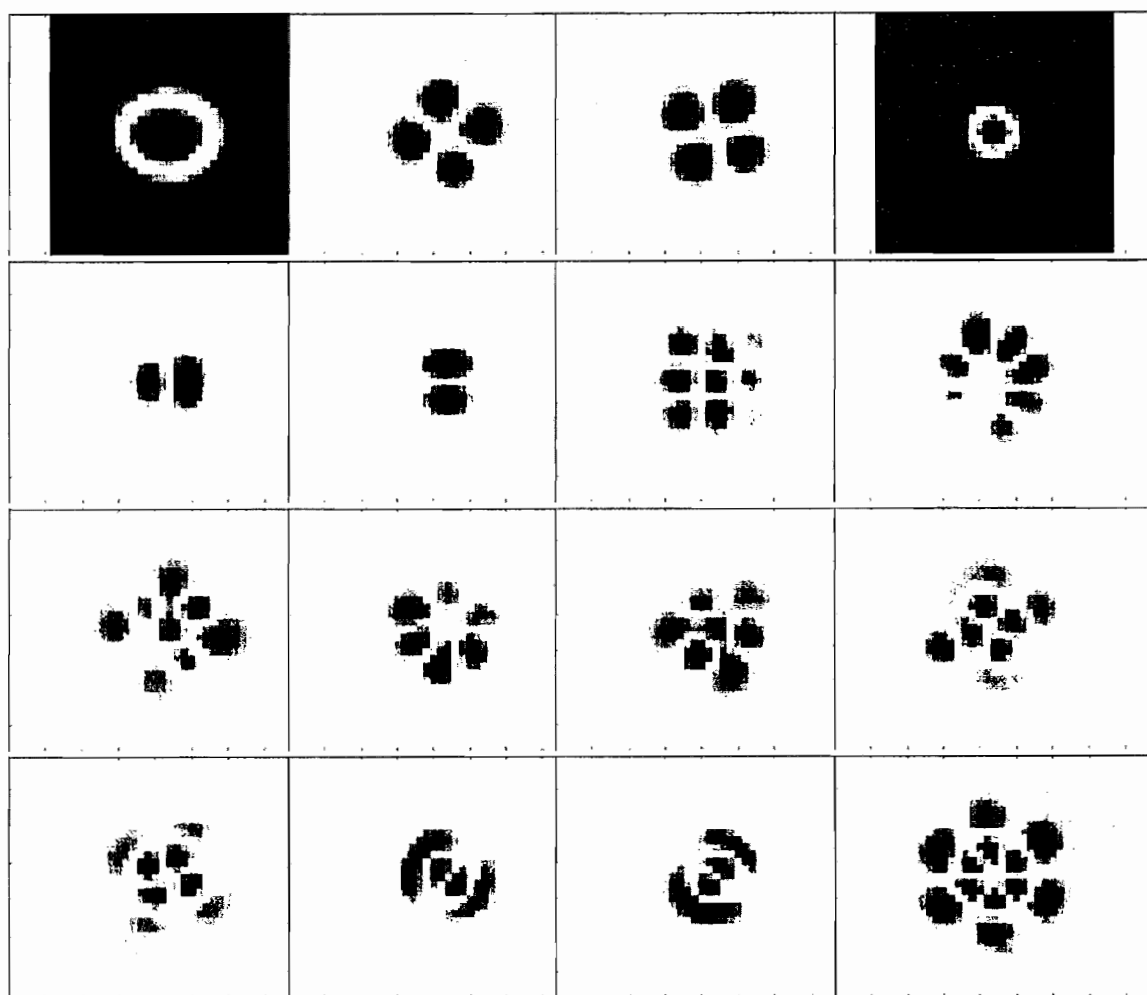


FIGURE 6.9: False color images of the first 16 principal components (ordered left to right and top to bottom) from 5224 images of λ DNA in a microchannel above an interdigitated electrode array. Each image is about 5 microns across

PCA of DNA Images with Known Conformational Changes

Before applying PCA to images of λ DNA subjected to a flashing potential, this section demonstrates the ability to measure conformational changes using PCA. A serendipitous sealing malfunction in a microchannel provided a useful test for applying PCA to conformational changes. An incomplete seal at the end of the microchannel created a narrow slit between the photoresist and the coverslip as shown in Fig. 6.10.A. There was some fluid flow through the slit, and this caused some DNA to be stuck at its entrance. The bulk fluid flow in the main microchannel stretched out the DNA, possibly making it easier for the DNA to enter the slit. Upon entering the slit, the DNA moved towards the narrow microchannel much more slowly than the bulk flow in the microchannel. As it moved, the DNA relaxed from its extended conformation towards a more compact coil. The DNA exited the slit into the narrow microchannel and rejoined the bulk solution. The various DNA conformations can be seen in the fluorescence microscopy images shown in Fig. 6.10.B. Although the stretching and relaxation process did not take place for all DNA molecules, the data still includes systematic conformational changes: the further a stretched piece of DNA moved through the slit, the less extended it became. PCA performed on these images shows two clear signals of conformational changes:

1. The principal components of DNA moving in the slit are different from those calculated from DNA in a microchannel.
2. The amplitudes of the first few principal components show clear changes as a function of position in the slit.

The analysis of these images exactly follows that described in Sec. 6.6.2, giving the first 16 principal components shown in Fig. 6.12.

The principal components calculated from the DNA moving through the slit are clearly different from those calculated from the DNA in the microchannel.

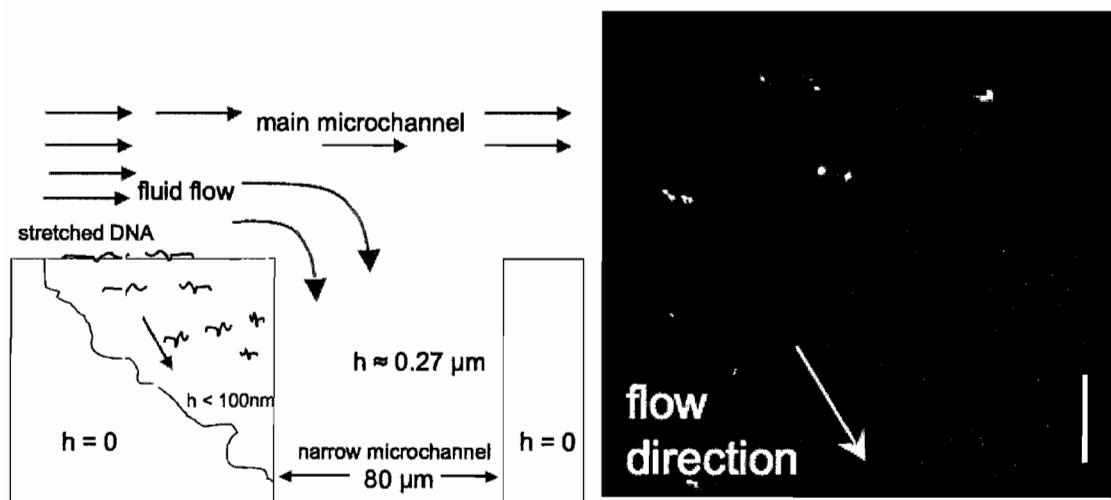


FIGURE 6.10: A. Top view sketch of the thin slit described in the text. The slit ($10\text{nm} < h < 100\text{nm}$) was formed between the coverslip and the photoresist due to incomplete sealing. λ DNA was nonspecifically bound to the edge of the slit and stretched out by fluid flow in the main microchannel. After being pulled into the slit, the DNA then returned to a less extended configuration as it moved through the slit towards the narrow microchannel. The DNA's speed through the slit was approximately $14 \mu\text{m}/\text{s}$. B. Fluorescence microscopy images of DNA in the slit, taken from the region outlined in yellow in A. Scale bar on the right is $10 \mu\text{m}$. The full contour length of λ DNA when intercalated with ToTo-1 dye molecules is $22 \mu\text{m}$.

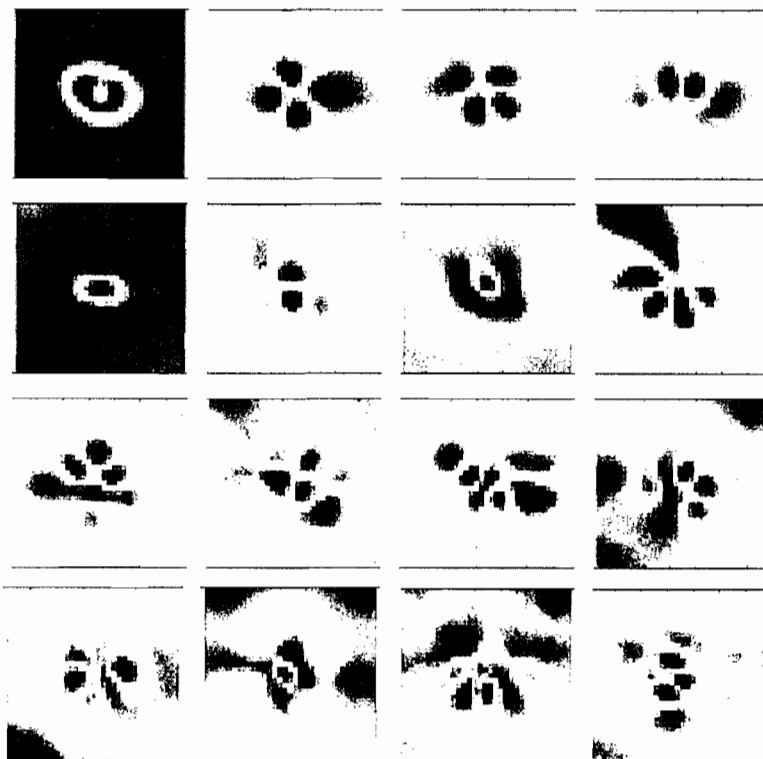


FIGURE 6.11: The first 16 principal components calculated from images of DNA in the slit described in Sec. 6.6.3. The principal components are ordered by decreasing eigenvalue left to right and top to bottom. Not all of these principal components exhibit the same clear symmetries seen in those calculated from DNA in the microchannel. The DNA in the slit is exploring a wide range of non-equilibrium configurations that are rare in the dynamics of the equilibrium configurations. Images are $5\mu m$ across.

These principal components do not show the symmetric patterns of the equilibrium components for several reasons: First, DNA molecules in the slit are far from equilibrium and are exploring highly asymmetric configurations (e.g. stretched out at the entrance to the slit). Second, the DNA are frequently interacting with the upper and lower surfaces of the slit. On a few occasions DNA was observed to be temporarily stuck to a surface in the slit and stretched out due to fluid flow in the slit. Nonspecific binding was very rare in the microchannel proper and so these interactions likely influenced the DNA dynamics. Third, the flow through the slit may not favor the DNA molecules achieving the equilibrium coil configurations before exiting the field of view. The principal component basis can provide the type of dynamical conformation information sought after in the analysis of the DNA images collected during application of the flashing potential in Sec. 6.5.2. Once the images are expressed in the basis of principal components, the amplitudes of the first few modes provide information about how the images of the polymer differ from mean intensity distribution. If changes in the conformation restrict or enhance the variability along a particular mode, the amplitude of that principal component will change accordingly. The subtraction of the mean from the original images means that each principal component also averages to zero. This is also consistent with the principal components themselves only being defined up to a sign: they are just eigenvectors of the covariance matrix. This sign ambiguity motivates plotting square amplitudes of the principal components for conformational analysis.

In order to show the conformational changes as the DNA moved through the slit, the quantities here are plotted as a function of position. Resulting plots of mean squared principal component amplitudes versus position in the slit are shown in Fig. 6.12. The decreasing trends shown in the data correspond to the changes in mean conformation as stretched DNA relaxes towards equilibrium coil configurations.

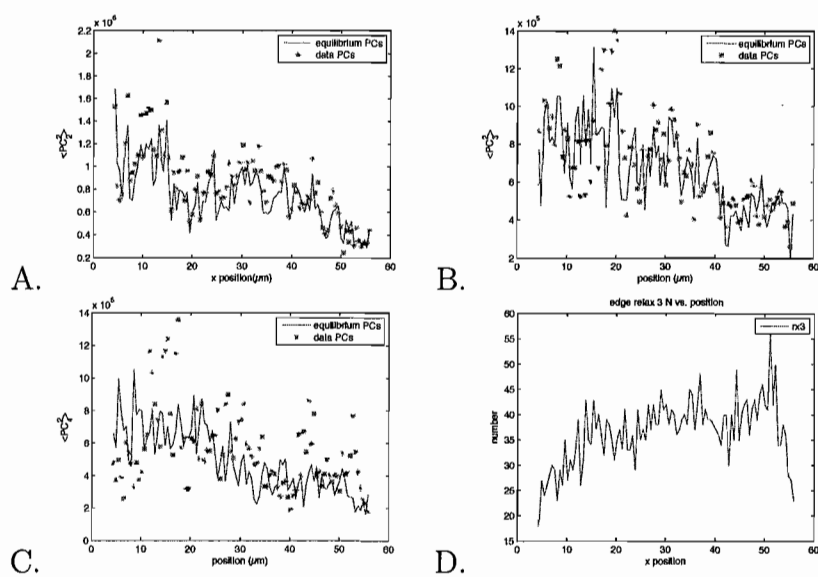


FIGURE 6.12: A-C. Mean square of principal component amplitudes 2-4 *vs.* position in the slit sketched in Fig. 6.10. The decrease in magnitude seen in these graphs shows the conformational change associated with relaxation of the extended DNA to more compact coil configurations. D. Number of data points associated with each mean plotted in A-C.

DNA Conformational Changes in Response to an Applied Potential

Now to apply PCA to images of DNA molecules collected during application of a flashing potential across the interdigitated electrode array. The image analysis and PCA techniques (which are identical to those described in Sec. 6.6.2) give a new set of principal components (Fig. 6.13). When compared to the equilibrium (no applied potential) principal components in Fig. 6.9, it's clear that the two series of images are nearly identical, indicating that the dynamics underlying their variances are very similar.

By inspection, it is clear that the variance in each mode is correlated with its spatial symmetries: principal components that share spatial symmetries (e.g. the same number of radial and polar nodes) have similar variances and fall next to each other in the sequence of components. In the case of the isotropic environment in the image plane, there is no preferred direction to allow the system to choose principal component 2 over component 3, for example. However, the displacement and velocities of the polymer are measured to be anisotropic (i.e. there is transport in the y -direction, so an aligning of principal components to the image axes would also suggest that the DNA is responded conformationally to the applied potential. No such alignment is seen in the principal components calculated here.

DNA conformational changes due to the applied voltage are not readily apparent in the principal components themselves, but the variance associated with each principal component contains further information. In order to compare the spectra before and during the applied voltage, the two data sets must be expressed in the same basis. To clarify: the goal is to compare the fraction of the variance associated with each principal component. This requires expressing the data collected while the flashing voltage was applied in the basis calculated from images collected *before any voltage was applied*. The two spectra of variances (each normalized by the total variance) can then be compared. The log of the stiffness of the first 16 modes is plotted versus

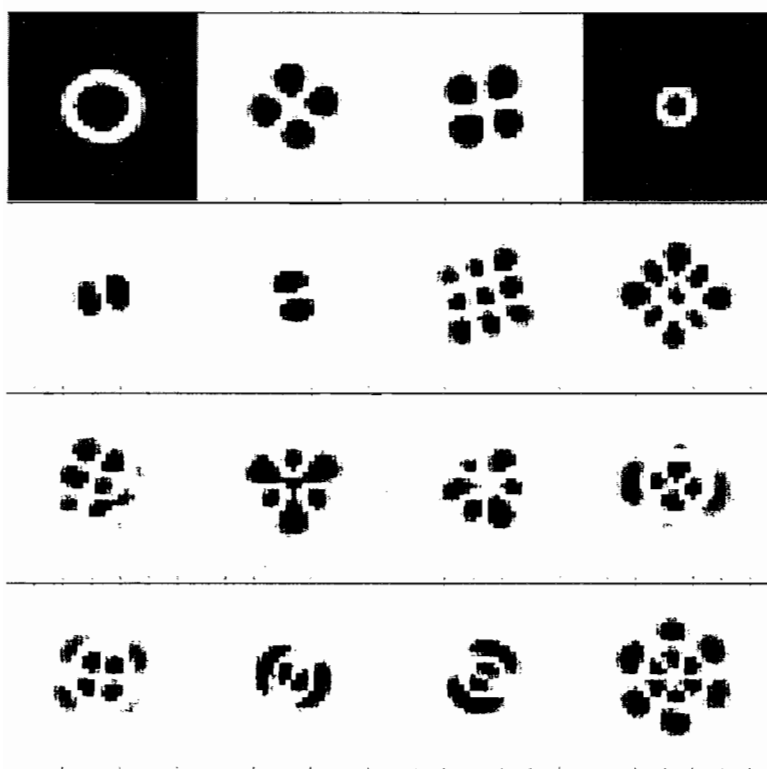


FIGURE 6.13: False color images of the first 16 principal components from images of λ DNA subjected to a flashing voltage. These images are almost identical to those calculated from images of DNA before any potential was applied (see Fig. 6.9). Each image is about $5 \mu m$ across.

mode number in Fig. 6.14. The stiffness k_i is defined in Eq. 6.6 and is proportional to the inverse of the fraction of the variance associated with the i^{th} principal component. The spectra of stiffnesses are calculated for DNA images both with and without an applied flashing voltage, but principal components used are calculated from data collected before any voltage was applied. The spectra plotted in Fig. 6.14 are very similar and the minor differences are most often amongst principal components that share the same symmetry. In the isotropic case, modes sharing the same symmetry (i.e. same number of radial and polar nodes) should each have the same share of the variance. However, experimental noise and finite data sets mean it's unlikely that three modes sharing the same symmetry will share the exact same variance. The data from equilibrium data are ordered by their variance, which also sets the order of the flashing voltage data points. Reordering of the components that share the same symmetry would make the two spectra nearly identical without obscuring any information.

Data of the squared amplitudes of the first four components are plotted *vs.* time for two temporal periods of the applied potential in Fig. 6.15. Especially compared to the y velocity signal seen in Fig. 6.6, the principal component amplitudes show no periodic signal. A periodic signal of any kind would indicate that the conformations explored by the DNA molecules changed with time and thus, with the application of the flashing potential. Although there are considerable fluctuations in each of the plotted quantities, the lack of periodic structure strongly indicates that no conformational changes are taking place that are accessible with this technique.

Summary of Results of Polymer Experiments

High quality images of individual λ DNA molecules in a microchannel above an interdigitated electrode array have been analyzed using trajectory analysis and principal components analysis. The resulting data show clear motion of the DNA

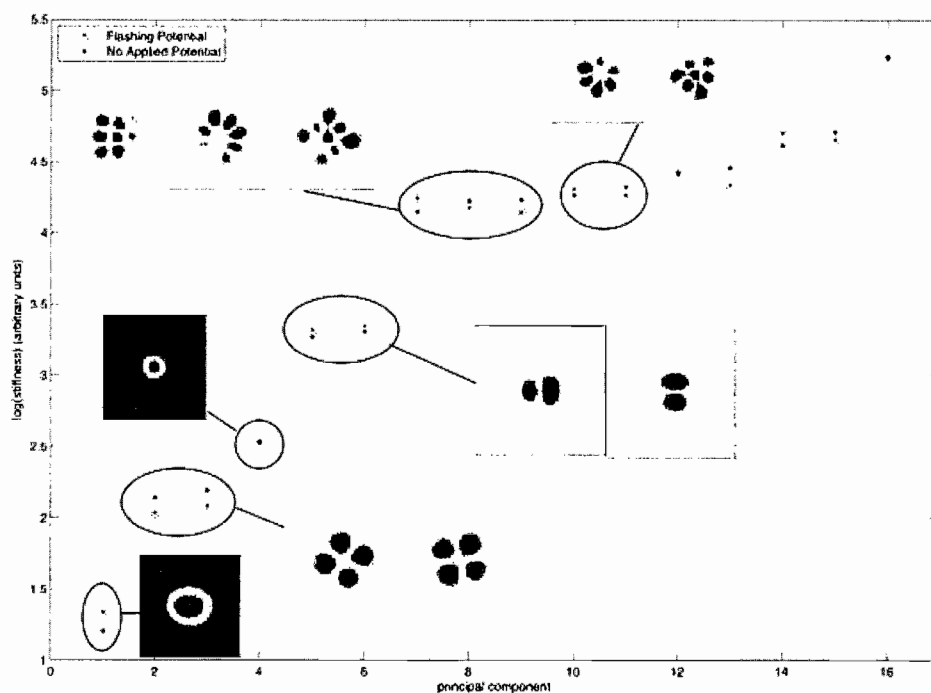


FIGURE 6.14: Spectra of the stiffness of the first 16 principal components as a function of principal component number. Both plotted data sets are derived from expressing images in the same basis: principal components calculated from images collected before any voltage was applied. The first 11 principal components are shown to illustrate that modes with the same symmetries are largely interchangeable in these spectra.

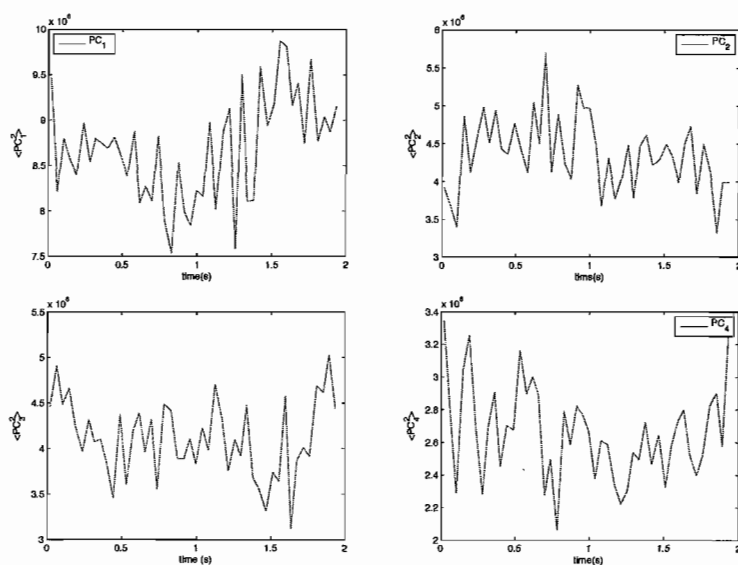


FIGURE 6.15: Square of principal component amplitudes 1-4 of λ DNA *vs.* time modulo two cycles of the flashing potential. The amplitudes are averaged over about 17 temporal cycles of the potential and each plotted point corresponds to ≈ 120 data points. There is no clear signal in response to the applied potential, especially compared to the y -velocity from the same data, which is plotted in the same format in Fig. 6.6.

molecules in response to the flashing applied voltage. However, displacements of $2 \mu m$ in response to potential switching contradict the polymer ratchet model described in Chapter III, which only allows displacements less than the spatial period of the underlying interdigitated electrode array, in this case $L = 500nm$. Despite the large displacements, further analysis using principal components methods shows no conformational changes in response to the applied voltage. This is consistent with the motion of DNA being caused by electroosmosis at the electrode array surface and leading to bulk flow in the microchannel. If other phenomena such as electrophoresis or thermophoresis affected polymer conformations, they were not measurable using principal components analysis.

CHAPTER VII

DIFFUSION AND NOVEL GEOMETRIES IN DETERMINISTIC LATERAL DISPLACEMENT DEVICES

Introduction

Thermal forces play an important role in the motion of micron-scale objects in aqueous solution, making the efficient sorting of colloidal particles based on size a challenging problem in technological applications. Deterministic Lateral Displacement (DLD) is a recently-developed method for separating micron-scale particles in solution using an array of obstacles in a microfluidic channel [30, 60, 29]. The basic DLD mechanism (illustrated in Fig. 7.1) uses a periodic array of obstacles to systematically displace particles larger than a critical size in one direction, while allowing smaller particles to move without any net lateral displacement. In experiments, the obstacles are cylindrical posts with a radius of a few microns and spacing about five to ten times the post size. The periodicity of the array shown (along with low Reynolds number and boundary conditions creating constant net flow through the microchannel) constrain fluid flows to have the qualitative form indicated. When a particle is smaller than the critical radius, r_c (here the width of the fluid flow ‘lane’ nearest an obstacle), its transport through the array follows the flow lines and so it experiences no net lateral displacement. Particles larger than r_c interact with the obstacle and are deflected into the adjacent lane. In limit of high flow speeds where diffusion can be ignored (see Sec. 7.4.3), this process happens systematically and deterministically, allowing for arbitrary spatial separation of particles after interacting with many rows of obstacles.

This method of sorting particles has a few clear benefits:

- Sorted particles can be collected in microfluidic outlet channels, allowing all particles to remain in their original aqueous environment and be used in subsequent processes.
- The critical radius for sorting is many times smaller than the separation between obstacles. This means that particles near the critical radius are unlikely to clog the array.

Initial analysis of this system would conclude that the critical radius of the device is just given by the gap between posts w_g divided by the periodicity of the device N , the number of rows before repeat.

$$r_c = \frac{w_g}{N} \quad (7.1)$$

This however, neglects the role that diffusion plays in determining the lateral displacement of particles as they move through the array. This chapter focuses on a model developed to address diffusion in DLD sorting. The model also allowed for exploration of previously ignored array geometries and led to the discovery of a novel sorting mode.

Published work on DLD has demonstrated some success at predicting the critical radius for sorting as a function of experimental parameters, including array dimensions and flow speeds. The most comprehensive attempt at these predictions is found in [61], where corrections due to diffusion and basic hydrodynamics are offered to Eq. 7.1. However, their analysis, which addresses data from all existing experimental literature [30, 60, 29, 62], is limited to the particular type of array geometry shown in Fig. 7.1 where an integer N characterizes periodicity of the obstacles. In fact, all published descriptions of DLD sorting mechanisms have used this restrictive geometry where the lateral spacing of obstacles p is an integer multiple of the shift of obstacles between rows, s . A more general array geometry allows for

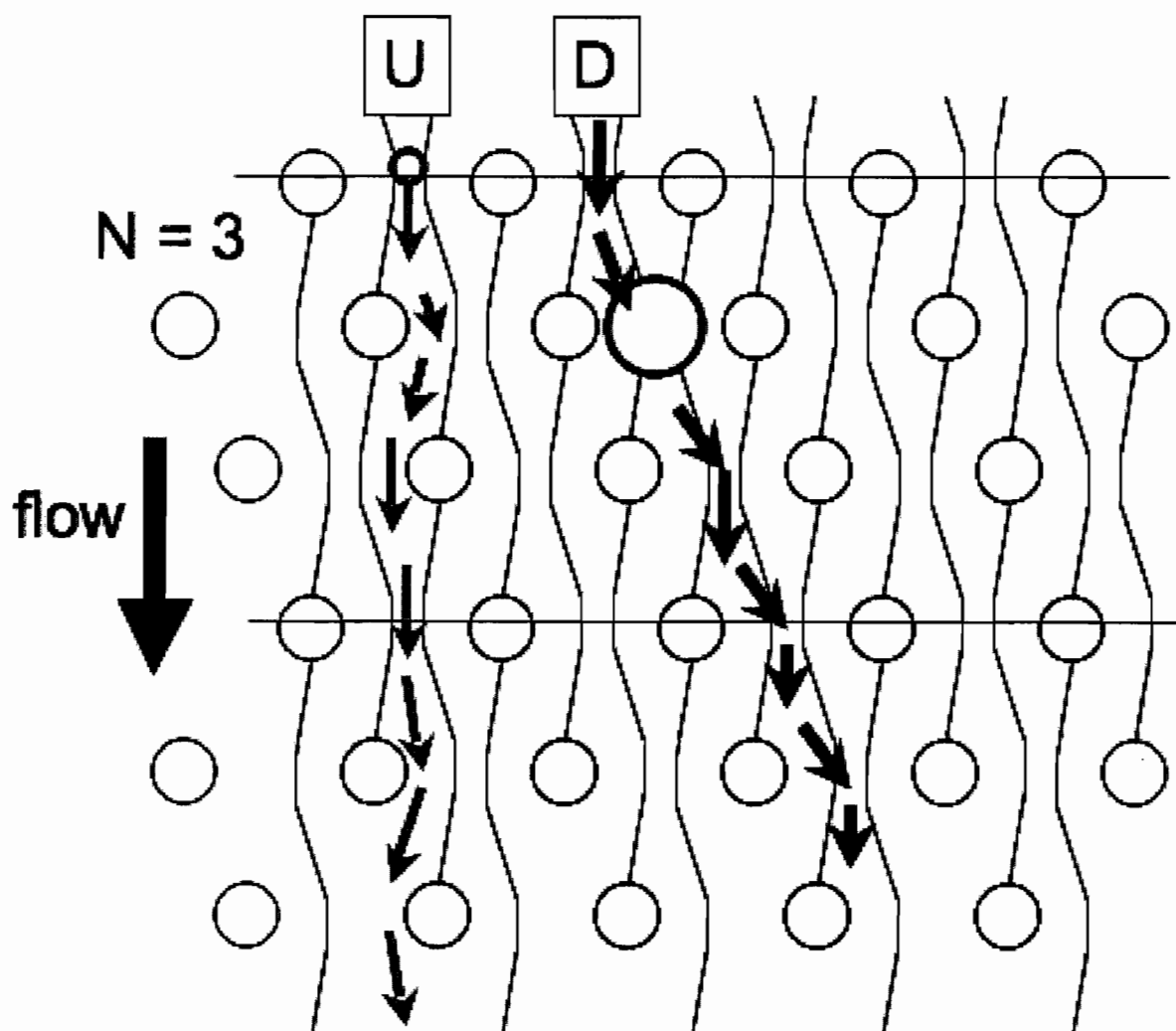


FIGURE 7.1: The basic DLD sorting mechanism in an array where the obstacle separation is $3 \times$ the shift between rows ($N=3$). Particles smaller than r_c (see Eq. 7.1) follow streamlines through the array of obstacles giving the path labeled 'U'. Particles larger than r_c are deflected at each row of posts, leading to the path marked 'D'.

obstacle spacings that are not related to s by simple integers. Previous work also focuses on array geometries with obstacle sizes comparable to obstacle separations p . In this regime, complex hydrodynamics largely determine the motion of particles through the array. This has been effective at sorting micron-sized particles [30, 60], coiled DNA [30] and red and white blood cells [29]. The lack of general array geometries and the rarity of diffusion in DLD analysis led to the model described below in Sec. 7.2. It reduces DLD sorting to its fundamental components in a limit where obstacles are small compared to their separation. This simplified model predicts novel sorting modes in DLD arrays and also shows a critical radius r_c that is robust against flow velocity changes. This model, which involves treating the obstacles as point-like posts, is also relevant to efforts to increase device throughput by reducing the hydrodynamic resistance of DLD devices through reduction in obstacle size.

Model and Implementation

The obstacles used in DLD devices are treated as an array of zero-radius posts arranged as indicated in Fig. 7.2. The lateral sorting behavior is of primary interest, so the array is taken to be infinitely deep and the flow is two-dimensional. One central simplifying assumption of the model is that the fluid flow is uniform throughout the array ($v(x, y) = v_0$). Particles move with the fluid unless they are displaced through interactions with obstacles. Point-like obstacles with a stick boundary condition may affect fluid flow in a region around them, but the stick boundary condition can be altered experimentally through the use of electroosmotically-driven (as opposed to pressure-driven) flow. The particles interact only with obstacles, and do so with a hard repulsion between the particle surface and the obstacle. This repulsion excludes the center of each particle from a circular neighborhood (with radius equal to that of the particle) around each obstacle. Another key assumption is that particles do not interact with each other and do not affect the fluid flow. Their motion also

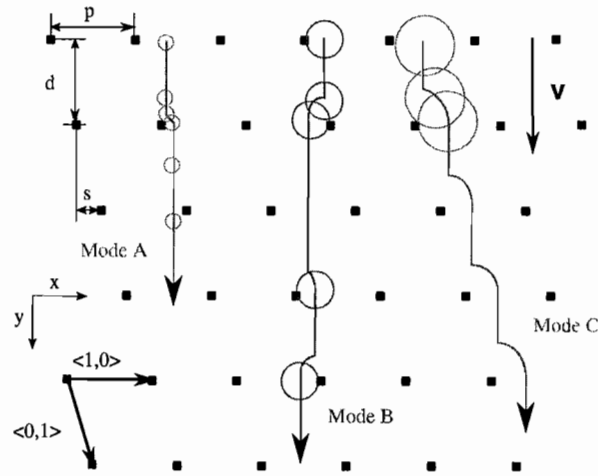


FIGURE 7.2: This sketch depicts the geometry used in the DLD model described in detail in Sec. 7.2. The array of point-sized posts is defined by p , the separation between posts, d , the distance between rows, and s , the lateral shift from one row to the next. Here $s = 0.3d = 0.3p$, corresponding to the results in Section 7.3. The point-like posts exclude the finite-sized particles with radius r from a circular region of the same radius around the post. The particle's motion through the array in the absence of diffusion includes movement along the straight flowlines (parallel to \mathbf{v}) and hard interactions with the obstacles. The paths are indicated schematically by arrows showing the three modes of transport through the array. These modes are defined by two critical radii, r_{c1} and r_{c2} described in the text. In mode A, ($r \leq r_{c1}$), there is no systematic net displacement in the x -direction. In mode B, ($r_{c1} < r \leq r_{c2}$) the particle moves in a zigzag pattern but is systematically displaced (to the left for this array). In mode C, ($r > r_{c2}$), at each row of posts, particles are displaced by the row shift s .

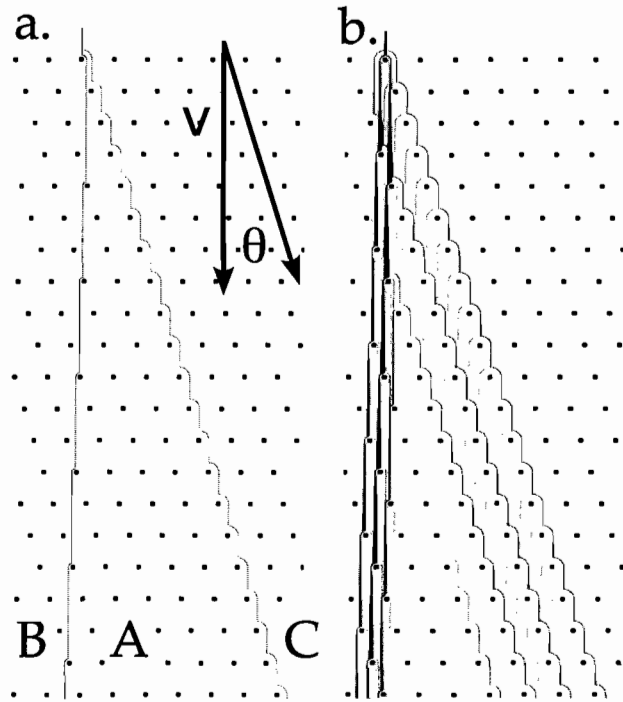


FIGURE 7.3: a. Composite image of spatial distributions without diffusion for particles with radii $r < r_{c1}$ (Mode A), $r_{c1} < r \leq r_{c2}$ (Mode B) and $r > r_{c2}$ (Mode C). Spatial distributions are characterized by a sorting angle θ , which is defined from the flow direction \vec{v} to the center of mass of each distribution. b. The same particle radii moving through the array with flow speed of $100 \mu\text{m/s}$ and including the effect of diffusion. Broadening of all distributions due to diffusion can be seen and particles in Mode C are sorted less efficiently. Initial spatial distributions are the same for all particle radii.

includes diffusion characterized by diffusion coefficient D and implemented through the distribution $\rho(x)$.

$$D(r) = \frac{k_B T}{6\pi\eta r} \quad (7.2)$$

with η the viscosity of the fluid.

The assumptions above allow the dynamics of the particles to be expressed in a continuous distribution ρ . The constant motion in the y -direction given by the velocity v further reduces the dependence on y , so that $\rho(x, t)$ captures the motion of a distribution of particles in x as it moves through the array. The collection of $\rho(x, t)$ for a given initial condition also corresponds to a continuous stream of particles moving through the array with a constant velocity and steady initial lateral distribution. The continuous distribution lends itself to easy inclusion of diffusion in the dynamics of particles, as described below. This scheme allows all the relevant dynamics of an ensemble of many particles to be captured in a continuous, lateral distribution $\rho(x)$ that moves through the array with velocity v . By following the evolution of $\rho(x)$ as the distribution interacts with posts and responds to thermal forces, this model identifies the basic modes of transport in an array of obstacles and the effect of diffusion on this transport. The calculations included here use an experimentally relevant post separation of 10 μm and with particle radii ranging from roughly 0.5 μm to 4 μm . The particles of interest are always suspended in aqueous solutions and flow speeds are typically less than a few mm/s , insuring that the Reynolds number is low and inertial effects can be ignored [28].

Schematically, the calculations proceed as follows: First, an initial distribution $\rho(x, y = 0, t = 0)$ enters the obstacle array at the ‘top’, moving in the y -direction with velocity v . For the data plotted below, a square distribution with width p is used for $\rho(x, y = 0, t = 0)$. However, an initial distribution that is much narrower is used in the images in Fig. 7.3 for clarity. The square distribution with width p accounts for all initial positions for particles entering the array, since the array is

periodic in the x -direction with period p . The resolution of the calculations is set by the number of pixels per spatial period; here 10^3 pixels are used for each period p . The calculation proceeds by starting with a distribution $\rho(x, y_0, t_0)$ and calculating $\rho(x, y_0 + \Delta y, t_0 + \Delta t)$ based on the previous distribution's interactions with the posts and according to the diffusion equation. The time step is taken as $\Delta t = \Delta y/v$, so the continuous distribution is evaluated discretely for each row of pixels. The method for calculating each new distribution is:

1. For a particle with radius r , the center of mass is excluded from an area with radius r around the point-sized obstacles. As the distribution encounters an obstacle, the distribution is set to zero in the excluded area and the distribution is increased at the edge of the excluded area such that the total number of particles is constant. This is shown in Fig. 7.3.
2. The new lateral distribution is then evolved in accordance with the diffusion equation:

$$\frac{\partial \rho}{\partial t} = D \frac{\partial^2 \rho}{\partial x^2} \quad (7.3)$$

as described below.

The second step is computationally simplified through the use of the Fourier cosine transform. First, the distribution in x , $R(k, y, t)$, is Fourier cosine transformed (denoted $F_{cos}[\]$ and described in Eq. 7.4). This is always done on an interval bounded by an impenetrable surface, either between two posts or across the entire calculation area (which is bounded by hard walls). Each Fourier coefficient is then multiplied by the Gaussian diffusion distribution with the corresponding k value (where k is the momentum conjugate to the spatial coordinate x). The new distribution is given by the inverse Fourier cosine transform. Because each of the Fourier cosine components has a derivative of zero at the boundary, the concentration gradient is always zero at the obstacles and at the edges of the array. This, along with proper normalization, insures

that no particles are allowed to diffuse into the obstacles or beyond the boundaries of the array. Only lateral diffusion is considered, because a steady-state flow is most relevant to DLD experiments. Broadening along the flow direction due to diffusion will not affect the lateral distribution of a steady stream of particles.

$$R(k, y_0, t_0) = F_{\cos}[\rho(x, y_0, t_0)]$$

where, for fixed y and t ,

$$F_{\cos}[g(x)] = \sum_n c_n \cos(k_n x)$$

denotes the Fourier cosine transform in x of a function $g(x, y, t)$. For a discretized finite interval L with pixel size Δx , $k_n = \frac{n\pi}{L}$ ranges from $\frac{\pi}{L}$ to $\frac{\pi}{\Delta x}$. So

$$\rho(x, y_0 + v\Delta t, t_0 + \Delta t) = F_{\cos}^{-1}[R(k, y_0 + v\Delta t, t_0 + \Delta t)]$$

and using Eq. 7.3, we have

$$\rho(x, y_0 + v\Delta t, t_0 + \Delta t) = F_{\cos}^{-1}\left[\sum_n c_n \cos(k_n x) e^{-Dk_n^2 \Delta t}\right] \quad (7.4)$$

Calculations were also performed without including thermal forces in order to show the sorting modes more clearly. These calculations are labeled $D = 0$ in plots, and show the limiting case of very high flow speed or low temperature. The calculations were done using Matlab software on personal computers and the University of Oregon's Academic Cluster.

Results

Transport of Particles Through the Array

The model described above was applied to a range of particle sizes and for various flow speeds. The 'zig-zag' mode (no net displacement) and the 'bumped'

mode (systematic displacement equal to the shift between rows) which have been previously described in DLD literature were confirmed. In addition, a novel sorting mode (labeled mode B in Fig. 7.3) was also observed in the calculated particle distributions. This mode has not been previously described in the literature for reasons discussed in Sec. 7.4.

The three modes of transport through the array can be easily seen in Fig. 7.3a. which the distributions are calculated without diffusion. The sorting directions for the three modes can be expressed in terms of the lattice vectors defined in Fig. 7.2:

- Mode A: Along the direction of flow. In this case \mathbf{v} is parallel to $\langle -3, 10 \rangle$.
- Mode B: Net displacement along the lattice vector $\langle -1, m \rangle$, where m is the integer quotient p/s .
- Mode C: $\ell_C = \langle 0, 1 \rangle$.

The sorting angles, θ_A , θ_B and θ_C are all defined between the lattice vectors mentioned above and the flow direction \mathbf{v} . For the arrays shown here, $\ell_B = \langle -1, 3 \rangle$, even though the flow \mathbf{v} is along $\langle -3, 10 \rangle$, as seen in Fig. 7.3. This difference between flow direction and the lattice vector $\langle 1, m \rangle$, then defines the angle θ_B . In the simulations, sorting the angle for a distribution is defined at a specific time as the angle between the flow direction \mathbf{v} and the center of mass of the distribution $\rho(x)$ at that time.

Particles move through the array in one of these three modes, depending on how their radius relates to two critical radii, r_{c1} and r_{c2} . For mode A, $r \leq r_{c1} = p$ modulo s ¹, particles may occasionally interact with the posts as seen in Fig. 7.3, but no net lateral displacement results. In Mode B ($r_{c1} < r \leq r_{c2} = s$), particles interact with posts more frequently than mode A but less frequently than Mode C. The direction of the displacement can vary with array parameters as described in Sec.

¹ a modulo $b := a - b \text{ floor}(a/b)$

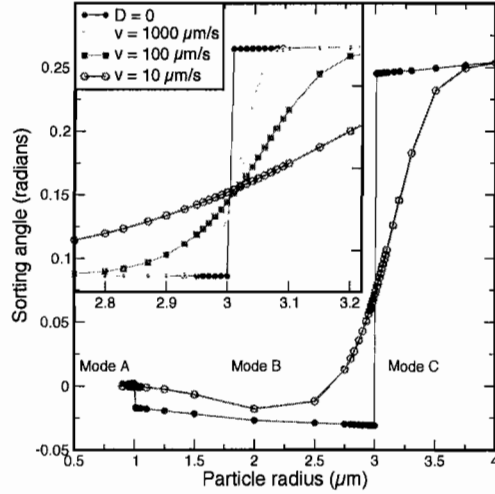


FIGURE 7.4: Sorting angles versus particle radius without diffusion (filled circles) and with diffusion at a flow velocity of $10\mu\text{m/s}$. The negative sorting angles for $r_{c1} < r < r_{c2}$ indicate the presence of mode B for the array used here; as in the text and other figures, $r_{c1} = 1\mu\text{m}$ and $r_{c2} = 3\mu\text{m}$. Inset shows the same quantity around $r = r_{c2} = 3\mu\text{m}$ for a range of flow velocities (same y-axis range). The sharp transition between sorting modes is blurred by diffusion.

7.4.2. Remaining particles ($r > r_{c2}$) fall into Mode C, where particles are displaced by s upon each interaction with a row of obstacles.

The Role of Diffusion in Particle Sorting

Lateral diffusion of the particles affects their direction of transport through the array. By plotting the sorting angle versus particle radius for a range of flow speeds, the effect of diffusion can be clearly seen (Fig. 7.4). These sorting angles are calculated after the distribution has passed through 10 rows of posts.

The data with slower flow speeds, where particles have more time to diffuse laterally at each step of the simulation, the effect of thermal motion on sorting is clearly seen: In the rows of posts, where the distribution is bounded in x to a region $\approx p - 2r$, the lateral diffusion of particles shifts the center of mass of the distribution $\rho(x)$ towards the midpoint between posts. This causes particles with $r < r_{c2}$ to be ‘bumped’ more frequently upon their interaction with the next row, and so their

sorting angle increases. In the the regions between rows, where the distribution is only bounded by the distant edges of the array, diffusion allows the particles to move laterally out of the path that would normally be ‘bumped’ to the by a post, decreasing their sorting angle. The smoothing of the angle *vs.* radius curves for slower flow speeds in Fig. 7.4 is due to the combined effect of these two phenomena.

Discussion

Novel sorting mode

One explanation for why mode B has not been mentioned in the literature of DLD sorting is that analysis of DLD devices has thus far been made with a fixed flow direction and with p an integer multiple of s . If this is the case,

$$r_{c1} = p \bmod s = 0 \tag{7.5}$$

and mode B vanishes. In devices characterized by post separations that are integer multiples of the shift between rows, all particles with $r \leq r_{c2}$ travel along the direction of flow. As seen in the simulation data shown in Fig. 7.4 and 7.3, the sorting angle of mode B is small compared to that of mode C. However, under the conditions outlined in Sec. 7.4.3, particles in mode B could realistically be spatially resolved from particles in modes A and C. This could lead to a useful secondary separation of particles in a single device. Assessment of the experimental detectability of this novel mode is discussed in Sec. 7.4.3.

Relationship between DLD and kinetically locked-in transport

While mode B is notably absent from DLD literature, it is implicitly present in the body of theoretical work studying transport through periodic potential landscapes. One system studied in that work consists of simulating the trajectories of objects

moving through a periodic, two-dimensional potential while being subjected to a steady external applied force. Typically, the direction of the applied force is varied for a fixed potential geometry and the transport direction is calculated [63, 64, 65, 66, 67]. Although no DLD experiments thus far have varied the flow direction for a fixed array, changing the spacing in a DLD array can be equivalent to varying the flow direction. For example, flow directions around $\langle -1, 3 \rangle$, the angles θ_B and θ_C vary as the flow directions change, but the relative angle between them ($\theta_C - \theta_B$) remains a constant defined by the array. The angle between modes B and C is then insensitive to flow direction for \mathbf{v} near (in this case) $\langle -1, 3 \rangle$. This is an example of a plateau in a so-called ‘devil’s staircase’: transport through a 2-D periodic potential is independent of flow direction near angles defined by lattice vectors with small integer-numbered lattice vectors, in this case $\langle -1, 3 \rangle$ and $\langle 0, 1 \rangle$ [63]. Many numerical simulations of trajectories of particles through two-dimensional periodic potentials have been done to study these and other phenomena, including sorting of particles [63, 64, 65, 67], but this body of work is rarely discussed in DLD literature. The transport theory work offers another perspective on the absence of mode B in previous descriptions of DLD arrays: the angle between modes B and C is constant and when B is chosen along A, transport in modes B and A are indistinguishable. It’s worth noting that mode B can be angled towards mode C, for example when flow is along $\langle -3, 8 \rangle$. The absence of Mode B in previous analyses of DLD experiments stems from the use of tilted square arrays with flows chosen along simple lattice vectors (e.g. $\langle 1, n \rangle$ as opposed to $\langle 2, m \rangle$) or more general arrays that are still limited to post separations p that are integer multiples of the shift s . In either case, modes A and B both go along the direction of flow.

There is also a technical difference between the transport theory modeling methods and the implementation used here (described in Sec. 7.2). Instead of adding thermal noise to deterministic equations of motion of particles (as is done in [64, 65, 66]), the simplifications used here allow all the dynamics of an ensemble to be expressed with

a continuous one-dimensional distribution that evolves in time. This enables easy incorporation of diffusion into modeling the transport of particles in DLD arrays. Also, the wide range of potential landscapes used in periodic potential landscape research seems to lack the particular form corresponding to hard spheres and point-sized obstacles. This interaction is also the same as that of point-sized particles moving in a uniform force field and interacting with finite-sized, circular obstacles.

Diffusion and Detectability

The results in Fig. 7.4 show clearly that diffusion affects sorting angle in this model, but the data do not show different critical radii for different flow speeds. The sigmoidal shape is smoothed by diffusion, but not shifted substantially. This is in contrast to experimental data from the first DLD publication [30], where the critical radius decreases significantly for smaller flow velocity. This effect may be due to finite size of the obstacles in experimental devices. The total fluid flux through any cross-section of the array parallel to the x -axis must be constant because aqueous solutions are essentially incompressible. This means that streamlines of the fluid flow are closer together between the posts than in the space between rows. As discussed in Sec. 7.3.2, diffusion within the rows tends to make particles more likely to follow the ‘bumped’ path, even in the case of a uniform flow field. The constrictions between finite-sized posts used in experiments narrow the streamlines there, amplifying the effect of lateral diffusion in the region where the particle interacts with the post. The limit explored in this model where obstacles are small compared to their separation, sorting is robust against changes in flow velocity.

Diffusion not only affects the sorting angle of particles moving through the array, it also broadens the lateral distributions of particles, which must be spatially separated to accomplish sorting. It is instructive to compare the diffusive spreading of the distribution to the shift between rows s in the time needed for a particle moving at

speed v to cover the distance between rows p . For high flow speeds,

$$v \gg \frac{2Dp}{(r - r_{c2})^2} \quad (7.6)$$

diffusion does not appreciably affect sorting and there are sharp transitions between sorting modes, as can be seen in the $D = 0$ case in Fig. 7.4. The velocity calculated above in Eq. 7.6 diverges as the particle radius approaches r_{c2} because the sorting angle is very sensitive to particle radius near r_{c2} . The sorting angle is also the most sensitive to diffusion near $r = r_{c2}$: Fig. 7.4 shows sorting angles of particles with r just greater than r_{c2} decrease by about half even at relatively high flow velocities ($1mm/s$). The particles closest in size to the critical radius are defined by the spatial resolution of this work (1 pixel = .01 microns). Particles with radii this close to the critical radius will still be sensitive to diffusion at flow velocities below $v \approx 10mm/s$. However, particles with radii greater or less than r_C still maintain a substantial fraction of their $D = 0$ sorting angle even at lower speeds.

In order for mode B to be experimentally detectable, the distributions of modes A and B must be spatially separated. The data shown in Fig. 7.5 show four qualitative regimes that could be observed in an experiment to detect the presence particle transport in mode B.

1. At very high flow speeds, (Fig. 7.5.a) the three modes are completely separated because each distribution is very narrow. In this regime, and spatial separation can be achieved simply by running the particles through a longer array.
2. At high intermediate flow speeds, (Fig. 7.5.b), the distributions have widened due to diffusion, but modes A and B are clearly distinguishable, despite some overlap.
3. At low intermediate flow speeds. (Fig. 7.5.c), modes A and B overlap enough to prevent resolution of two separate distributions. This regime is imminently relevant to DLD device design because it would be experimentally observed

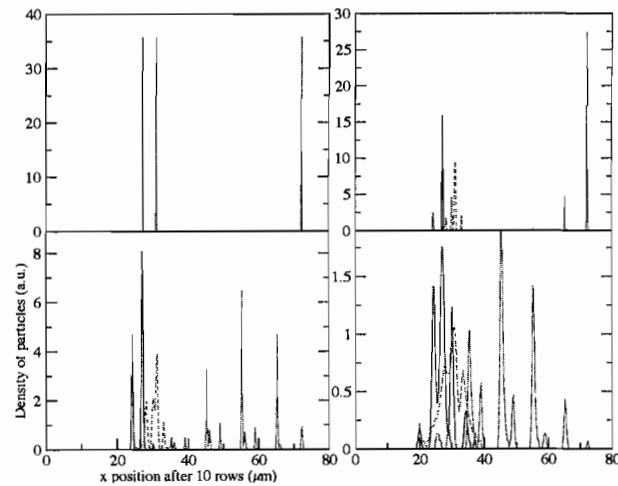


FIGURE 7.5: Spatial distributions of particles and mode detectability. Particle densities after ten rows of the array for three radii, $0.9 \mu m$, $2 \mu m$ and $3.08 \mu m$. a. No diffusion. b. $v = 1000 \mu m/s$ c. $v = 100 \mu m/s$ d. $v = 10 \mu m/s$. b. shows a case where mode B could be detected experimentally. For lower speeds (Fig. c) modes A and B are not resolvable but the combined distribution is broader than mode A alone. For even lower speeds (d) the distributions of particles in modes A and B are each wider than the separation between them and the two modes are completely unresolvable. The total number of particles is the same in each case and the initial distribution is a square distribution with width equal to the post separation $p = 10 \mu m$.

as an unexplained broadening of the distribution associated with the ‘zig-zag’ path.

4. At low flow speeds, distributions from modes A and B are completely intermingled and may even be indistinguishable from mode C.

Possibilities for Experimental Realization

In order to experimentally attain the simplifications set out by this model in Sec. 7.2, microfluidic channels would have to be fabricated with very small obstacles. DLD arrays made obstacles that are much smaller than their separation are also of interest to researches trying to increase fluid flow through DLD devices. For a given post separation, smaller posts reduce the hydrodynamic resistance of the DLD device and allow higher throughput for a given pressure difference across the device. In addition to diffusion-induced broadening of the spatial distributions, size dispersion of particles can also affect the measured distributions. Most DLD experiments are done using commercially available polystyrene beads, which typically have a size dispersion of less than $\pm 10\%$. This means that in order to differentiate between modes A and B in an experiment based on Fig. 7.5 where particles were 0.9 and $2 \mu m$, commercial particles must be purchased with radii 10% further apart. That is, in this case, particles should be chosen with size distributions centered on $0.8 \mu m$ and $2.2 \mu m$ to avoid contamination of one distribution in another. If lingering hydrodynamic effects of finite posts or limitations on flow velocity in an experimental setup prevent mode B from being completely resolved, it may still be present as an asymmetric broadening of the distribution of particles not in the ‘bumped’ mode, as in Fig. 7.5.

Conclusions

A simple model of DLD separation has identified a novel sorting mode for particles traveling in solution through periodic arrays of obstacles. The model also reproduces

key features of DLD arrays: particles are sorted based on size and the transitions between modes are smoother when flow velocities are reduced. The model and results should be useful to DLD researchers because the critical radius is robust against changes in flow velocity and the hydrodynamic drag of an array made from very small posts will be smaller than conventional designs.

CHAPTER VIII

CONCLUSIONS AND OUTLOOK

Conclusions

Brownian ratchets provide a method for transporting micron scale (and smaller) objects in solution without the use of long-range, macroscopic potential gradients. In the case of the flashing ratchet, this ‘force-free’ transport relies on keeping the thermal system out of equilibrium, utilizing the spatial asymmetry of a potential with micron scale periodicity. Experimental realizations of Brownian ratchet systems have seldom included the analysis of individual trajectories, and in the case of interdigitated electrode array devices, trajectory information reveals complex and varied dynamics in a relatively simple system.

The experiments discussed in Chapter V show that charged particles in solution are moved when flashing voltages are applied across interdigitated electrode arrays. However, there are a few observations that strongly suggest that the motion does not correspond to Brownian ratchet transport: A primary result from the particle experiments is that particle displacement in response to switching the potential on was too large to correspond to the movement of particles to the minimum of a periodic potential created by the electrode array. A secondary effect of applying voltages across electrode arrays in silicon dioxide microfluidic channels offers a more suitable explanation for the observed particle trajectories: fluid flow generated by electroosmosis. This effect has been reported in other electrode array geometries by microfluidics researchers [43, 44, 45, 47, 48], but not in the case of equally-sized, asymmetrically-spaced interdigitated electrodes.

In the case of polymers (Chapter VI), trajectory analysis was combined with principal components analysis (PCA) of images of individual λ DNA molecules. PCA of individual molecule images has been demonstrated here to be effective in measuring conformational changes of single DNA molecules. However, when applied to DNA subjected to a flashing ratchet potential, no signature conformational changes were measured, despite the clear motion of DNA in response to potential switching. From this, the conclusion drawn here is that electroosmotically-driven bulk flow transported the DNA without measurably affecting its conformations.

Deterministic Lateral Displacement (DLD) is a recently developed sorting mechanism that shows promise for separating objects in solution based on size. As discussed in Chapter VII, diffusion of particles in DLD sorting arrays has been incorporated into a model of the separation process in the limit of point-like obstacles. Results obtained from computer modeling predict novel sorting modes in unconventional DLD arrays with row shifts that are not integer multiples of obstacle separations. Also, the critical size for sorting in this model is more robust against velocity changes than existing experimental arrays.

Outlook

Although the work here indicates that interdigitated electrode arrays are not well-suited for generating asymmetric, periodic potentials for objects in solution, the arrays do exhibit transport due to electroosmotic flow. This capability has been exploited by others for pumping of fluids using AC voltages applied across similar electrode arrays [43, 44, 45, 47, 48] which may provide an avenue for future research and applications. In order to study Brownian ratchet transport, scanning line optical traps are currently being explored to generate the necessary asymmetric, periodic potential [19, 16]. Very recent experiments involving positional feedback in the flashing ratchet system have confirmed the continued utility of optical traps in Brownian ratchet research [68].

The high quality images of individual DNA molecules has allowed for PCA to be successfully applied to λ DNA subjected to the electroosmotically-driven flows of interdigitated electrode arrays. Although there is currently only one published paper on PCA and polymer images [59], PCA could readily provide insight into the conformations and dynamics of confined polymers, which are typically limited to describing how various quantities scale with polymer length [55, 69, 54, 70, 53]. Application of PCA to these systems could help quantify the changes in conformation over time and the differences between conformations of DNA under different confinement conditions.

With regards to DLD separation, the predicted novel sorting modes may be experimentally observed under the conditions discussed in Chapter VII. This may require novel fabrication techniques in order to realize the limit of small post size and incorporating semiconductor nanowires into microfluidic channels is a topic of ongoing research that ¹ [71]. In the future, sorting in experimental devices could be compared directly to simulation data in order assess the role of finite post size in determining critical radii and verifying the resolvability of new sorting modes. Devices with several sorting modes and critical radii that are robust against flow velocity changes would provide a useful extension of DLD device research.

¹Currently a Ph.D. project in Jonas Tegenfeldt's group at Lund University

APPENDIX A

IMAGE ANALYSIS AND OBJECT TRACKING

Introduction

Epi-fluorescence microscopy allows fluorescent, submicron objects to be visualized in the optical spectrum. This capability is very useful for qualitative observations, but the investigation of transport in a ratchet system requires quantitative information about the trajectories of individual objects. The objects of interest must be located, other objects in the frame must be ignored, and then the objects' locations in each frame must be linked together to form trajectories of individual objects. In the experiments described in the main text, the images of submicron beads or λ DNA were recorded with CCD cameras, with 0-100 objects present in each frame. The number of objects in a given frame may fluctuate due to particles entering and leaving the field of view, becoming photobleached or leaving the focal plane. Since all of these small objects in solution are diffusing and may also be actively transported, the task of turning particle locations into accurate trajectories is an important one. Fortunately, much of the heavy lifting on this topic has already been done and software tools for this task are publicly available. The David Grier group (currently at NYU) wrote software in the IDL programming language that is capable of robust and flexible particle tracking and documented the process in [72]. The description of particle tracking below follows their algorithm and was implemented using their original IDL software or the version ported to Matlab by Daniel Blair and Eric Dufresne.

Locating Objects in Images

Particle tracking is the first step to extracting particle trajectories or polymer conformations from images. Twelve bit grayscale images are collected by the CCD camera and stored to a hard disk and image analysis is done after the experiments are complete (typically 10-20 data sets of 1000-3000 images for each experiment). The steps of the tracking algorithm are as follows:

- Images are spatially bandpass filtered. The highpass filter eliminates constant and slowly-varying image background noise, potentially due to inhomogeneous illumination or misalignment of a planar sample to the focal plane. The lowpass filter reduces high spatial frequency noise, typically additive camera noise that is uncorrelated between pixels. The lowpass filter averages over adjacent pixels to reduce the pixel noise in each frame. The filtered image is smoother than the original frame and has no background variation.
- Local maxima pixels are found within a region of interest size set by the user to be a bit larger than the object size. These maxima are taken as the first approximation of particle locations.
- The object locations are then further refined by calculating the centroid of the region of interest centered on the approximate object locations. This centroid is the reported object location. In DNA experiments, this centroid was calculated directly from the original image (as opposed to the filtered image) in order to maintain the high spatial frequency information for principal components analysis.

Creating Trajectories from Positions

To track objects from image i to $i + 1$, a object location is searched for in frame $i + 1$ within a neighborhood around where a object was found in frame i . For data where particle separation is larger than the particles' displacement between frames, this method is sufficient. In problematic regions of an image sequence where particles are separated by distances comparable to their displacements between frames, more complex treatment is needed. The method described in [72] attempts all possible particle displacement combinations in the problematic area and the combination that produces the lowest total displacement is used.

APPENDIX B

DNA SOLUTION

Introduction

λ DNA belongs to the λ phage, a virus that infects bacteria [2]. It has 48kbp long and is 16 μm before exposure to intercalating dyes and 22 μm after full incubation to give 1 dye molecule for every 4 base pairs [73]. λ -DNA was chosen because it is easy to acquire in relatively pure form and long enough to cover several periods of the interdigitated electrode array in solution (see VI). The degassing steps are to prevent bubble formation in the microfluidic channels, and the mercaptoethanol prevents photobleaching.

Making the DNA Solution

1. 50 $\mu g/mL$ λ -DNA (48kbp) solution is thawed slowly from $-20^{\circ}C$ to $0^{\circ}C$ in an ice bath
2. DNA solution is diluted 1:10 in .5x TBE and 16% ToTo-1 stock solution (Molecular Probes)
3. Incubated at $50^{\circ}C$, wrapped in foil to avoid light exposure for 30 minutes
4. Solution was stored in a refrigerator in a box to avoid unnecessary light exposure.
5. Solution and diluting buffer mentioned below were degassed by sonication and simultaneous vacuum pumping for at least 20 minutes.

6. DNA solution was then diluted 1:10 to form a solution of $.5\mu\text{g}/\text{mL}$ λ -DNA in $.5\text{x}$ TBE and 3% mercaptoethanol by volume.
7. Solutions with lower concentrations of DNA (e.g. $.125\ \mu\text{g}/\text{mL}$ λ -DNA) in $.5\text{x}$ TBE and 3% mercaptoethanol by volume were used at times during the experiments.

APPENDIX C

FABRICATION OF INTERDIGITATED ELECTRODE DEVICES

Device Fabrication: Polymer Experiments

The version of the interdigitated electrode array devices used in polymer experiments described in Chapter VI were fabricated as User Projects at the Molecular Foundry at LBNL in Berkeley, CA with the help of Gerard Schmid, Bruce Hartenek, and Stefano Cabrini. Additional fabrication was done at Lund University in Lund, Sweden with the help of Ivan Maximov, Mariusz Graczyk, Jason Beech and Jonas Tegenfeldt. An earlier version was fabricated entirely at Lund University and all polymer experiments were performed in the lab of Dr. Jonas Tegenfeldt at Lund University.

Electrode array fabrication

Electron-beam lithography and optical lithography techniques were used to pattern the electrode arrays and metal contacts using the following protocol:

EBL

1. 4% PMMA was spun at 4000 rpm on 4" Si wafers with 210 nm of oxide
2. EBL exposure of electrode arrays with $CD = 50nm$ and period $L = 500nm$
3. 50Å Cr and 150Å Au were evaporated and liftoff done in dichloromethane.

Optical Lithography I: Metal Features

1. HMDS adhesion promoter was spun at 2000rpm on the wafers after liftoff of the EBL features.
2. MA-P 1215 positive photoresist was spun on at 3000rpm, followed by 2 minute bake on a 100°C hotplate.
3. The photoresist was exposed in a contact mask aligner for 3.5sec.
4. 50Å Cr and 150Å Au were evaporated and liftoff done in acetone.

Optical Lithography II: Microchannel and Fluidics

1. SU-8 2005 was diluted 1:1 in cyclopentanone and was spun at 3000rpm on the wafer after liftoff of the optically-patterned metal features. Post-application bake was done for 2 minutes in a 65°C oven and 2 minutes on a 100°C hotplate.
2. Exposure for 8 seconds, development in SU-8 developer for 60s, resulting in a patterned film approximately 26 μ m thick.
3. Rinsing with IPA was followed by N_2 drying and immediate sealing of the microchamber (as described below)

Microchamber fabrication

The microchambers were constructed by sealing a fitted glass coverslip directly to the patterned SU-8 immediately after development. The delay between development and sealing was minimized to avoid contamination of the surface with particles and to maintain the stickiness of the SU-8 surface.

1. Number 1 coverslips were cut to fit the outer border of the SU-8 pattern without encroaching on the electrical contact area.

2. Coverslips were sonicated in warm acetone and then isopropanol, followed by isopropanol rinse.
3. The chip with patterned SU-8 was placed on a microscope slide on a hotplate warming from room temperature to 100° C.
4. The clean coverslip was put in place on the SU-8 and pressure was applied using metal tweezers. Deformation of the coverslip where pressure was applied led to contact between the SU-8 and the coverslip.
5. By applying careful pressure at several locations on the device, a complete seal was obtained with about 50-75 % success.

Experimental Procedure

- Aligned microfluidic access holes on chip to the gaskets on the capillary fittings in the chuck. The chip was then held in place by applying vacuum.
- Electrodes were clipped in place in contact with the chip and electrical continuity was verified by measuring the resistance between clips attached to the same rail electrode.
- Capillary tubing attached to the chip was fitted to a Hamilton syringe (volume 250 μL) in a syringe pump and the DNA solution was pumped into the chip at rates of 1-5 $\mu\text{L}/\text{min}$.
- When wetting of the fluidic access channels was observed by eye, the chuck was placed in the microscope and the objective was brought into focus on the sample.
- Image collection was done with a range of exposures and applied voltages for up to 12 hours.

Device Fabrication: Particle Experiments

The interdigitated electrode array devices used in particles experiments described in Chapter V were fabricated as User Projects at the Molecular Foundry at LBNL in Berkeley, CA with the help of Gerard Schmid, Bruce Hartenek, and Stefano Cabrini. Very early devices were obtained from the Cura-Gen corporation, a biotech company with early interest in sorting DNA using Brownian ratchet devices [23].

Electrode array fabrication

All metal patterning of electrode arrays for particle experiments was done using UV lithography techniques.

Patterning Metal Features

1. HMDS adhesion promoter was spun at 2000rpm on the wafers after liftoff of the EBL features.
2. MA-P 1215 positive photoresist was spun on at 3000rpm, followed by 2 minute bake on a 100°C hotplate.
3. The photoresist was exposed in a contact mask aligner for 3.5sec.
4. 50Å Cr and 150Å Au were evaporated and liftoff done in acetone.

Patterning Microchannel

1. SU-8 2002 was spun at 3000rpm on the wafer after liftoff of the optically-patterned metal features. Post-application bake was done for 2 minutes in a 65°C oven and 2 minutes on a 100°C hotplate, resulting in a film of approximately 1.6 μm thickness.
2. Exposure for 8 seconds

Microchamber fabrication

Devices manufactured on 4-inch wafers were cleaved into chips with single devices. Cleaving procedure includes a small ($\sim 1\text{mm}$) score mark perpendicular to the wafer flat at the desired position of the cleavage. The surface of the wafer opposite this score mark is then placed on a razor blade mounted vertically in a chuck. Careful pressure with the thumbs on both sides of the score mark then cleaves the wafer along a vertical crystal plane near the score mark and perpendicular to the flat of the wafer. Subsequent cleaving is done perpendicular to these cleaved surfaces.

Number 1 coverslips are scored and broken by hand to a size of approximately 5 x 25 mm- narrow enough to allow the patterned SU-8 to extend beyond the width of the coverslip and long enough to allow for easy gripping with tweezers on a part of the coverslip that is not used for sealing. Cut coverslips are then cleaned by sonication in 50°C acetone and IPA for 10 minutes each, rinsing with the previous solvent after each step and maintaining liquid coverage of the surface at all times. After the final IPA rinse, coverslips are blown dry with nitrogen and set aside in a dry Eppendorf tube.

The device chips are cleaned in IPA at 50°C for 10 minutes with some agitation by hand. Chips are then placed in fresh IPA for a few minutes before being rinsed with IPA and dried with nitrogen. The use of acetone or sonication in cleaning devices can rapidly degrade the SU-8 film and lead to delamination of the photoresist or a rough SU-8 surface. The clean chips are placed directly onto a clean glass slide on a 60-80°C hotplate warming from room temperature to a 110°C setpoint. Coverslips are aligned to cover the microchannel and firm pressure is applied with tweezers to the coverslip over the SU-8 patterned areas, sealing the coverslip to the photoresist. Interference fringes provide visual indication of submicron variations in thickness of any remaining air gap. A successfully sealed device has no interference fringes across both of the SU-8/coverslip interfaces. After a good seal is achieved, the hotplate is turned off and allowed to return to room temperature slowly with the sealed devices

still on it. Quick removal of the devices can result in spontaneous unsealing of the coverslips. After the hotplate reaches room temperature, the devices are checked that the seal has been maintained. If not, the devices are heated again and pressed with tweezers to reseal the microchamber.

Success rates for well-cleaned devices are around 90% for this method; unsuccessful sealing is usually the result of inhomogeneity of the resist film from the initial spincoating procedure (e.g. bubbles or particles in the SU-8) or debris from the cleaving process deposited on the surface. By insuring that clean chips and coverslips are exposed to air for less than 30 seconds, many successful chambers were sealed in a room without specialized air filtration or laminar flow.

Sealing Details

Leaks to air are quickly apparent because the microchannel is so shallow; the loss of a small volume of water to evaporation leads to a large movement of the air-water interface in the microchannel. In cases where the seal was poor, air bubbles were usually visible by the time the device was placed in the microscope.

In nearly all microchannels sealed as described above, the vacuum grease - bead solution interface could be seen slowly encroaching into the microchannel, often from both ends. Motion of less than about 1 mm occurred over a few hours, with vacuum grease often occupying 10% or more of the microchannel's length by the end of a three-hour experiment. Because water is an incompressible fluid, motion of the vacuum grease-water interface can only be due to an increase in height of the chamber, water leaving the chamber, or a combination of the two.

APPENDIX D

FLUORESCENCE MICROSCOPY METHODS

Polymer and particle experiments both utilized epifluorescence microscopy to image fluorescent objects in solution. A diagram of the epifluorescence filtering scheme is shown in Fig. D.1.A.

Particle Experiments

Particle experiments discussed in Chapter V utilized a Leica DM LFS upright epifluorescence microscope with a 10x N.A 0.3 objective and Q-Imaging Retiga Exi CCD camera. Excitation light was from a 100W Hg lamp and the filter cube whose transmission characteristics are shown in Fig. D.1

Polymer Experiments

Polymer experiments also used epifluorescence as described above, but with a Nikon Eclipse TE2000U inverted microscope, a Nikon CFI Apo TIRF 100x, N.A. 1.49 Oil objective and an Andor iXon electron-multiplying, cooled CCD camera.

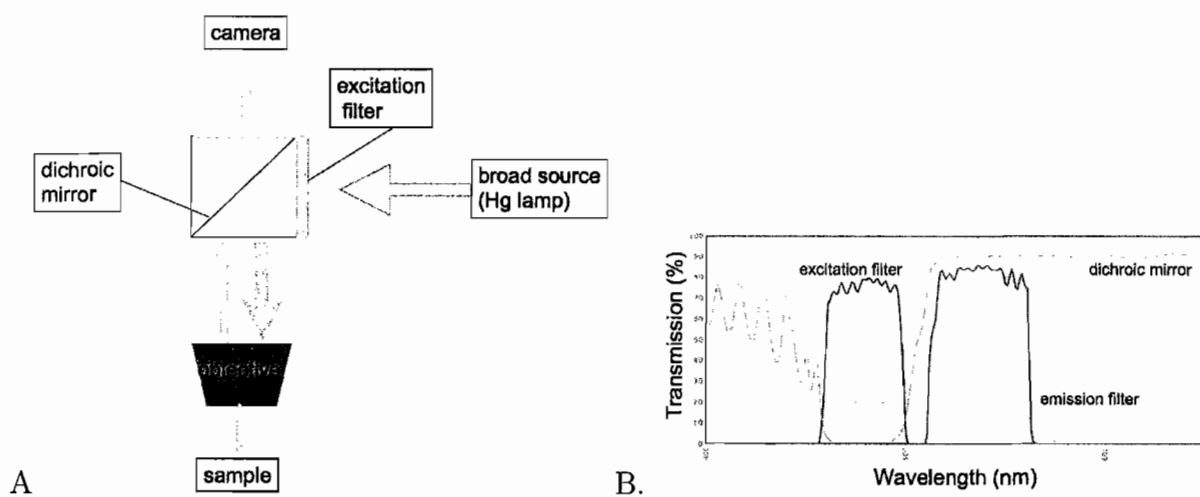


FIGURE D.1: A. Sketch of epifluorescence layout. The broad excitation light source is filtered to the spectrum indicated by the excitation filter transmission curve in B. This same band is reflected by the dichroic mirror and then excites the fluorescent sample. Emission light is transmitted by the dichroic mirror and then is filtered before being detected at the camera. B. Transmission characteristics of the epifluorescence filter used in particle experiments.

BIBLIOGRAPHY

- [1] *dna structure diagram* (*en.wikipedia.org*) (2008).
- [2] P. C. Nelson, *Biological Physics: Energy, Information, Life* (W.H. Freeman and Co., New York, 2004).
- [3] F. Julicher, A. Ajdari, and J. Prost, “Modeling molecular motors,” *Rev. Mod. Phys.* **69**(4), 1269–1281 (1997).
- [4] M. O. Magnasco, “Forced thermal ratchets,” *Phys. Rev. Lett.* **71**(10), 1477–1481 (1993).
- [5] R. D. Astumian and M. Bier, “Fluctuation driven ratchets - Molecular Motors,” *Phys. Rev. Lett.* **72**(11), 1766–1769 (1994).
- [6] R. D. Astumian, “Thermodynamics and kinetics of a Brownian motor,” *Science* **276**(5314), 917–922 (1997).
- [7] P. Reimann and P. Hanggi, “Introduction to the physics of Brownian motors,” *Appl. Phys. A-materials Science and Processing* **75**, 169–178 (2002).
- [8] P. Reimann, “Brownian motors: noisy transport far from equilibrium,” *Phys. Reports-review Section Phys. Lett.* **361**, 57–265 (2002).
- [9] M. Downton, M. J. Zuckermann, E. M. Craig, M. Plischke, and H. Linke, “Single-polymer Brownian Motor: a simulation study,” *Phys. Rev. E* **73**(011909) (2006).
- [10] J. Ingen-Housz, “Remarks on the use of the microscope,” (1784).
- [11] R. Brown, “Brief Account of Microscopical Observations,” *Edinburgh new Philosophical Journal* (1828).
- [12] A. Einstein, “Ueber die von der molekularkinetischen Theorie der Waerme geforderte Bewegung von in ruhenden Fluessigkeiten suspendierten Teilchen,” *Annalen der Physik* (1905).
- [13] R. P. Feynman, R. B. Leighton, and M. Sands, *The Feynman Lectures on Physics*, Vol. 1 (Addison-Wesley, 1966).

- [14] P. Curie, *J. Phys. (Paris)* (1894).
- [15] P. Hanggi, F. Marchesoni, and F. Nori, “Brownian Motors,” *Annalen der Physik* **14** (2005).
- [16] T. Harada and K. Yoshikawa, “Fluctuation-response relation in a rocking ratchet,” *Phys. Rev. E* **69** (2004).
- [17] J. Mai, I. M. Sokolov, and A. Blumen, “Directed particle diffusion under “burnt bridges” conditions,” *Phys. Rev. E* **64**01(1), 011 102 (2001).
- [18] J. Rousselet, L. Salome, A. Ajdari, and J. Prost, “Directional motion of brownian particles induced by a periodic asymmetric potential,” *Nature* **370**, 446–448 (1994).
- [19] L. P. Faucheux, L. S. Bourdieu, P. D. Kaplan, and A. J. Libchaber, “Optical thermal ratchet,” *Phys. Rev. Lett.* **74**, 1504–1507 (1995).
- [20] S. H. Lee, K. Ladavac, M. Polin, and D. G. Grier, “Observation of flux reversal in a symmetric optical thermal ratchet,” *Phys. Rev. Lett.* **94** (2005).
- [21] L. Gorre-Talini, J. Spatz, and P. Silberzan, “Dielectrophoretic ratchets,” *Chaos* **8**(3) (1998).
- [22] A. van Oudenaarden and S. G. Boxer, “Brownian Ratchets: Molecular Separations in Lipid Bilayers Supported on Patterned Arrays,” *Science* **285** (1999).
- [23] J. S. Bader, R. W. Hammond, S. A. Henck, M. W. Deem, G. A. McDermott, J. M. Bustillo, J. W. Simpson, G. T. Mulhern, and J. M. Rothberg, “DNA transport by a micromachined Brownian ratchet device,” *Proc. National Acad. Sciences United States Am.* **96**, 13 165–13 169 (1999).
- [24] J. S. Bader, M. W. Deem, R. W. Hammond, S. A. Henck, J. W. Simpson, and J. M. Rothberg, “A Brownian-ratchet DNA pump with applications to single-nucleotide polymorphism genotyping,” *Appl. Phys. A-materials Science and Processing* **75**, 275–278 (2002).
- [25] R. W. Hammond, J. S. Bader, S. A. Henck, M. W. Deem, G. A. McDermott, J. M. Bustillo, and J. M. Rothberg, “Differential transport of DNA by a rectified Brownian motion device,” *Electrophoresis* **21**, 74–80 (2000).
- [26] D. Dan, A. M. Jayannavar, and G. I. Menon, “A biologically inspired ratchet model of two coupled Brownian motors,” *Physica A-statistical Mechanics Its Applications* **318**, 40–47 (2003).

- [27] E. M. Craig, M. J. Zuckermann, and H. Linke, “Mechanical coupling in flashing ratchets,” *Phys. Rev. E* **73**(5), 051 106 (2006).
- [28] H. Bruus, *Theoretical Microfluidics*, 2nd ed. (unpublished lecture notes, 2005).
- [29] J. A. Davis, D. W. Inglis, K. J. Morton, D. A. Lawrence, L. R. Huang, S. Y. Chou, J. C. Sturm, and R. H. Austin, “Deterministic hydrodynamics: Taking blood apart,” *Proc. National Acad. Sciences United States Am.* **103**(40), 14 779–14 784 (2006).
- [30] L. R. Huang, E. C. Cox, R. H. Austin, and J. C. Sturm, “Continuous particle separation through deterministic lateral displacement,” *Science* **304**(5673), 987–990 (2004).
- [31] L. Landau and E. Lifshitz, *Statistical Physics* (Butterworth-Heinemann, 1980).
- [32] W. Sutherland, “A Dynamical Theory of Diffusion for Non-Electrolytes and the Molecular Mass of Albumin,” *Philosophical Magazine and Journal of Science* (1905).
- [33] Y. M. Wang, H. Flyvbjerg, E. C. Cox, and R. H. Austin, *Lecture Notes in Physics: Controlled Nanoscale Motion*, Vol. 711/2007 (Springer Berlin/Heidelberg, 2007).
- [34] M. Doi and S. F. Edwards, “The theory of polymer dynamics,” (1987).
- [35] *en.wikipedia.org:S.P.L.Sørensen* (website, 2008).
- [36] M. Daune, *Biophysique moléculaire/ Molecular biophysics : structures in motion* (Oxford University Press, Oxford ; New York, 1999).
- [37] I. Gradshteyn and I. Ryznik, *Table of Integrals, Series, and Products* (Academic Press).
- [38] D. Stigter, “Interactions of highly charged colloidal cylinders with applications to double-stranded DNA,” *Biopolymers* **16**(7), 1435–1448 (1977).
- [39] P. Dechadilok and W. M. Deen, “Hindrances factors for diffusion and convection in pores,” *Industrial and Engineering Chemical Research* **45**(21), 6953–6959 (2006).
- [40] A. Ramos, H. Morgan, N. G. Green, and A. Castellanos, “Ac electrokinetics: a review of forces in microelectrode structures,” *J. Phys. D-applied Phys.* **31**, 2338–2353 (1998).
- [41] S. H. Behrens and D. G. Grier, “The charge of glass and silica surfaces,” *J. Chem. Phys.* **115**(14), 6716–6721 (2001).

- [42] A. Ajdari, "Pumping liquids using asymmetric electrode arrays," *Phys. Rev. E* **61**(1), R45–R48 (2000).
- [43] A. Ajdari, "Electrokinetic 'ratchet' pumps for microfluidics," *Applied Physics A-Materials Science and Processing* **75**(2), 271–274 (2002).
- [44] A. B. D. Brown, C. G. Smith, and A. R. Rennie, "Pumping of water with ac electric fields applied to asymmetric pairs of microelectrodes," *Phys. Rev. E* **63**(1), 016 305 (2000).
- [45] M. M. Gregersen, L. H. Olesen, A. Brask, M. F. Hansen, and H. Bruus, "Flow reversal at low voltage and low frequency in a microfabricated ac electrokinetic pump," *Phys. Rev. E* **76**(056305) (2007).
- [46] L. H. Olesen, H. Bruus, and A. Ajdari, "ac electrokinetic micropumps: The effect of geometrical confinement, Faradaic current injection, and nonlinear surface capacitance," *Phys. Rev. E* **73**(5), 056 313 (2006).
- [47] A. Ramos, A. Gonzalez, A. Castellanos, N. G. Green, and H. Morgan, "Pumping of liquids with ac voltages applied to asymmetric pairs of microelectrodes," *Phys. Rev. E* **67**(5), 056 302 (2003).
- [48] V. Studer, A. Pepin, Y. Chen, and A. Ajdari, "Fabrication of microfluidic devices for AC electrokinetic fluid pumping," *Microelectronic Engineering* **61-2**, 915–920 (2002).
- [49] A. A. L. Olesen, Henrik Bruus, "AC electrokinetic micropumps: the effect of geometrical confinement, Faradaic current injection, and nonlinear surface capacitance," *Phys. Rev. E* (2005).
- [50] S. Duhr and D. Braun, "Why molecules move along a temperature gradient," *Proc. National Acad. Sciences United States Am.* **103**(52), 19 678–19 682 (2006).
- [51] H. S. Rye, S. Yue, D. E. Wemmer, M. A. Quesada, R. P. Haugland, R. A. Mathies, and A. N. Glazer, "Stable fluorescent complexes of double-stranded DNA with bis-intercalating asymmetric cyanine dyes: properties and applications." *Nucleic Acids Res* **20**(11), 2803–2812 (1992).
- [52] P.-G. de Gennes, *Scaling Concepts in Polymer Physics* (Cornell University Press, 1979).
- [53] J. O. Tegenfeldt, C. Prinz, H. Cao, S. Chou, W. W. Reisner, R. Riehn, Y. M. Wang, E. C. Cox, J. C. Sturm, P. Silberzan, and R. H. Austin, "The dynamics of genomic-length DNA molecules in 100-nm channels," *Proc. National Acad. Sciences United States Am.* **101**(30), 10 979–10 983 (2004).

- [54] W. Reisner, J. P. Beech, N. B. Larsen, H. Flyvbjerg, A. Kristensen, and J. O. Tegenfeldt, “Nanoconfinement-enhanced conformational response of single DNA molecules to changes in ionic environment,” *Phys. Rev. Lett.* **99**(5), 058 302 (2007).
- [55] A. Balducci, P. Mao, J. Y. Han, and P. S. Doyle, “Double-stranded DNA diffusion in slitlike nanochannels,” *Macromolecules* **39**(18), 6273–6281 (2006).
- [56] A. Cohen and W. Moerner, “Internal Mechanical Response of a Polymer in Solution,” *Phys. Rev. Lett.* **98**(116001) (2007).
- [57] H. Yamakawa, *Modern theory of polymer solutions* (Harper and Row, New York, 1971).
- [58] B. Flury, *Common principal components and related multivariate models* (Wiley, New York, 1988).
- [59] A. E. Cohen and W. E. Moerner, “Principal-components analysis of shape fluctuations of single DNA molecules,” *Proc. National Acad. Sciences United States Am.* **104**(31), 12 622–12 627 (2007).
- [60] D. W. Inglis, J. A. Davis, R. H. Austin, and J. C. Sturm, “Critical particle size for fractionation by deterministic lateral displacement,” *Lab on a Chip* **6**(5), 655–658 (2006).
- [61] M. Heller and H. Bruus, “A theoretical analysis of the resolution due to diffusion and size-dispersion of particles in deterministic lateral displacement devices,” arXiv:0711.0347v1 [physics.flu-dyn] (2007).
- [62] J. P. Beech and J. O. Tegenfeldt, “Tuneable separation in elastomeric microfluidics devices,” *Lab on a Chip* (2008).
- [63] C. Reichhardt and F. Nori, “Phase locking, devil’s staircases, Farey trees, and Arnold tongues in driven vortex lattices with periodic pinning,” *Phys. Rev. Lett.* **82**(2), 414–417 (1999).
- [64] A. Lacasta, M. Khoury, J. Sancho, and K. Lindenberg, “Sorting of Mesoscopic Particles Driven Through Periodic Potential Landscapes,” *Mod. Phys. Lett. B* **20**(23), 1427–1442 (2006).
- [65] K. Ladavac, K. Kasza, and D. G. Grier, “Sorting mesoscopic objects with periodic potential landscapes: Optical fractionation,” *Phys. Rev. E* **70**(1), 010 901 (2004).
- [66] M. Pelton, K. Ladavac, and D. G. Grier, “Transport and fractionation in periodic potential-energy landscapes,” *Phys. Rev. E* **70**(3), 031 108 (2004).

- [67] Y. Roichman, V. Wong, and D. G. Grier, “Colloidal transport through optical tweezer arrays,” *Physical Review E* **75**(1), 011407 (2007).
- [68] E. M. Craig, N. J. Kuwada, B. J. Lopez, and H. Linke, “Feedback control in flashing ratchets,” *Annalen der Physik* **17**(2-3), 115–129 (2008).
- [69] W. Reisner, K. J. Morton, R. Riehn, Y. M. Wang, Z. N. Yu, M. Rosen, J. C. Sturm, S. Y. Chou, E. Frey, and R. H. Austin, “Statics and dynamics of single DNA molecules confined in nanochannels,” *Phys. Rev. Lett.* **94**(19), 196101 (2005).
- [70] J. O. Tegenfeldt, H. Cao, W. W. Reisner, C. Prinz, R. H. Austin, S. Y. Chou, E. C. Cox, and J. C. Sturm, “Stretching DNA in nanochannels,” *Biophys. J.* **86**(1), 596A–596A (2004).
- [71] T. Martensson, M. Borgstrom, W. Seifert, B. J. Ohlsson, and L. Samuelson, “Fabrication of individually seeded nanowire arrays by vapour-liquid-solid growth,” *Nanotechnology* **14**(12), 1255–1258 (2003).
- [72] J. C. Crocker and D. G. Grier, “Methods of Digital Video Microscopy for Colloidal Studies,” *J. Colloid Interface Sci.* **179**(298) (1996). URL <http://physics.nyu.edu/grierlab/methods/methods.html>.
- [73] T. T. Perkins, D. E. Smith, R. G. Larson, and S. Chu, “Stretching of a single tethered polymer in a uniform-flow,” *Science* **268**(5207), 83–87 (1995).